AN ABSTRACT OF THE THESIS OF

Abdullah M.S. Almasoumi for the degree of Doctor of Philosophy in Nuclear Engineering presented on December 6, 1989

Title: Monte Carlo Model of a Capture Gamma Ray Analyzer for a Seafloor Core Sample

Abstract approved: Redacted for Privacy
Stephen E. Dykas

Of great benefit, but not limited to seafloor mineral exploration, is a technique that fairly rapidly determines the composition of a drilled vibracore (in a time comparable to the time involved in obtaining the core). The rapid assessment is desired to predict whether a given region warrants further exploration by coring.

A proposed monitoring system, based on neutron capture gamma ray analysis, consists of a container tank filled with water and tubular extensions that house a Cf-252 neutron source and a detector positioned within the tank. The core sample is passed through the system in stop and count steps. The net count rates, due to "signature" capture gamma rays from neutron capture in elements in the core sample, are proportional to the amount of the element responsible for emitting the capture gamma ray.

The proposed system was modeled and simulated by the Monte Carlo method to predict the relationship between the response of the

detector and the elemental concentrations within the sample. Accurate and detailed treatment of neutron transport and gamma ray production and attenuation within the system were employed not only to predict the relationship of the photopeak responses with respect to elemental concentrations, but also to permit investigation of the design parameters and structural material changes in the system.

The developed Monte Carlo code utilizes a variety of variance reduction techniques, such as implicit absorption with Russian Roulette and deterministic production of the gamma rays of interest, along with a form of correlated sampling to predict simultaneously the responses over a range of interest of the elemental concentrations. The predicted results were compared with predictions obtained from a well established general purpose Monte Carlo code (MCNP).

Monte Carlo Model of a Capture Gamma Ray Analyzer for a Seafloor Core Sample

by

Abdullah M.S. Almasoumi

A THESIS

Submitted to

Oregon State University

in partial fulfilment of
the requirements for the
degree of

Doctor of Philosophy

Completed December 6, 1989

Commencement June 1990

APPROVED:

Redacted for Privacy

Associate Professor of Nuclear Engineering in charge of major

Redacted for Privacy

Head of Department of Nuclear Engineering

Redacted for Privacy

Dean of Graduate School

Date thesis is presented December 6, 1989

Typed by Abdullah M.S. Almasoumi for Abdullah M.S. Almasoumi

IN THE NAME OF ALLAH, THE MOST BENEFICENT, THE MOST MERCIFUL

ACKNOWLEDGEMENTS

For his guidance and support in the preparation of this thesis, I would like to express my deepest appreciation to my advisor Dr. Stephen E. Binney. Special thanks are extended to the members of my Advisory Committee: Drs. Simon S. Johnson, Andrew C. Klein, John C. Ringle, and James R. Welty.

I would like to express my heartfelt appreciation to my mother, sisters, relatives, and friends for their prayers, support, and encouragement.

From the deepest of my heart I thank my daughter for the endless support, sacrifices, and understanding throughout my studies.

To whom I owe all what I am, Muhammad Sultan, Zarifah, and Reham I dedicate this work.

TABLE OF CONTENTS

TABLE OF CONTENTS (Continued)

LIST OF FIGURES

LIST OF FIGURES (Continued)

LIST OF FIGURES (Continued)

LIST OF TABLES

Monte Carlo Model of a Capture Gamma Ray Analyzer for a Seafloor Core Sample

1. INTRODUCTION

1.1 Neutron Capture Prompt Gamma Ray Analysis

Neutron capture prompt gamma ray analysis (NCPGA) is a nuclear technique that can be used to perform quantitative analysis of elemental concentrations in a host matrix. This technique is based on the principle that neutron captures result in the formation of compound excited nuclei which de-excite promptly (in less than 10^{-12} s) by the emission of one or more gamma rays with energies (typically 2 to 11 MeV) and yields that are characteristic of the excited nuclei and the energy of the original captured neutron that initiated the reaction.

In general, NCPGA is only sensitive to the major elemental constituents of a sample and offers a complementary technique for the conventional delayed gamma ray neutron activation analysis (NAA) which is best suited for trace element analysis. It has been shown that NCPGA has greater inherent sensitivity than conventional NAA for most elements, provided that equal neutron fluxes can be achieved for activation (Isenhour, 1966). A comparison of the theoretical sensitivity limits for the analysis of 63 elements by NCPGA and NAA shows that, calculating with an equal neutron flux, the NCPGA would be superior for 61 of these elements (Henkelmann, 1978).

The major difference between the two techniques is the fact

that in conventional NAA, the analysis depends on the radioactive product of the neutron bombardment, if formed in reasonable amounts with an inherent phenomenon of growth and decay. NCPGA, however, is independent of the product's nuclear characteristics.

The term "prompt" gamma ray analysis is to be understood as the observation of the characteristic electromagnetic radiation resulting directly from the neutron radiative capture. This radiation is prompt in the sense that the nuclear decay time is in the order of 10^{-12} s and thus strongly contrasts with the time delay of seconds, or longer, characteristic of gamma radiation following β^- decay. In fact the term "prompt gamma analysis" is not strictly accurate since the prompt gamma rays include also those from inelastic neutron scattering, which is a threshold reaction determined by the level of the first excited state of the target nucleus and hence is of interest when fast neutrons are used.

Foremost among the advantages of NCPGA over conventional NAA is the fact that NCPGA eliminates errors of timing encountered during corrections for decay during counting. The prompt gamma rays are emitted before the product has any chance to migrate out of the sample and the possibility of loss of any volatile species as a result of Szilard-Chalmers processes is avoided. Also, the sample to be analyzed needs little or no preparation, and it produces negligible residual activity. The drawback of NCPGA not being suitable to take advantage of decay to identify species and observe contaminants, or avoid interference is not considered serious.

This work pertains to computationally modeling, by the Monte

Carlo method, a proposed monitoring system based on the NCPGA principle for the purpose of quantitatively analyzing the elemental concentrations of elements of interest (Mg, Cl, Ti, Cr, Mn, and Fe) found in vibracores taken from seafloor sediment core samples. All of the abovementioned elements have major capture gamma rays of energies above 3 MeV. In contrast, the gamma rays produced by neutron activation, neutron inelastic scattering, and natural radioactivity have energies mainly below 3 MeV.

The non-destructive, fairly rapid sampling of all or most of a process stream (bulk sampling), thus giving more representative results, the minimal interference from natural radioactivity, and the feasibility of portable small intense neutron sources all make the NCPGA a prime technique for in-situ mineral exploration to identify and quantify the elements present in a field sample.

Although of no economical interest, chlorine is included in the list above since in marine applications, the high gamma ray background from the $Cl(n,\gamma)$ reaction is the major interference. The area under the full energy peaks of the characteristic capture gamma rays (fingerprints) from these elements are non-linear functions of the elemental concentrations in the core sample, because of the competition for neutrons among the various constituents of the sample, especially if strong neutron absorbers are present. Hence the relationship between the photopeak response and the elemental concentrations needs to be estimated by Monte Carlo technique.

The Monte Carlo model is useful in the calibration of such a monitoring system without the need for constructing calibration

standards representative of the various elemental concentrations of the sample. This calibration is helpful to investigate and predict the variation of detector response with elemental concentrations. A single calibration standard composed of known elemental concentrations within a matrix of composition similar to that expected in the field is needed to normalize the responses estimated by the Monte Carlo model. In addition, the model is thought to be useful for sensitivity analysis investigations of the design parameters, such as the sample to source and detector distances and relative locations or the concentration of a given element. This is feasible because of the detailed treatment of neutron transport in the system and detailed treatment of capture gamma ray transmission.

1.2 Literature Review

The majority of the literature on the use of the NCPGA in mineral exploration and on-line analysis represents extensive experimental determination and assessment of the use of this nuclear technique. Numerous sources are given in the reference listing (Charbucinski *et al.*, 1986; Clayton, 1983; Failey *et al.*, 1979; Glascock, 1982; Lukander and Uusitalo, 1979; Moxham *et al.*, 1976; Nargolwalla *et al.*, 1973; Senftle *et al.*, 1974; Tanner *et al.*, 1972; Thomas *et al.*, 1983; Uusitalo *et al.*, 1982; Wormald and Clayton, 1983). In this work it is relevant to emphasize the theoretical modeling and to compare the results of such modeling with experimental work if possible.

The research in general is concerned with a borehole geometry.

Brief descriptions of previous work, relevant to the potential benefits of computer simulation, are summarized below. The flux distribution in the medium of interest as an integral part of a model, represented by steady-state diffusion theory, has been applied to obtain the neutron flux distribution from a point source in cylindrical coaxial geometry (representative of borehole geometry)(Nargolwalla *et al.*, 1973). The resulting neutron spatial distribution was used to compute neutron capture reaction rates to assess the unscattered gamma-ray flux reaching a point detector by integrating over the medium volume.

A sonde-in-borehole configuration was modeled by Doster (1979) to predict the photopeak detector response (Fe: 7.64 MeV peak) from a thin axial zone of iron concentration. The four-group neutron flux distribution was determined by the two-dimensional multigroup diffusion theory code PDQ-5. Numerical integration over the medium volume was performed to calculate the prompt gamma production rate resulting from the neutron capture reaction rates. The obtained results were in good agreement with the experimental results .

Sohrabpour and Bull (1979) developed a Monte Carlo model to predict the photopeak detector response from a capture gamma ray experiment in an infinite homogeneous medium with a Cf-252 neutron source and a Ge(Li) detector. Neutron cross sections were based on six(one thermal)-group cross sections. The predicted responses for copper and tungsten were shown to be non-linear. The model was tested experimentally, and the results showed that the model predictions exceeded the experimental values by 30-40%.

The discrete ordinate (1-dimensional) neutron transport code ANISN was used to determine the neutron flux distribution in a multi-layered medium in a spherical geometry of coal with a neutron source in the center (Reynolds, 1977; Elias and Gozani, 1980). Analysis of the bulk density, sample uniformity, system size and hydrogen content on the prompt gamma ray flux in the experimental system was assessed.

A multigroup Monte Carlo method to determine the ash content of coal was reported by Wormald *et al.* (1979).

Clark *et al.* (1982) reported a Monte Carlo model for borehole geometry with thorough treatment of neutron transport within the shielding components. Pointwise ENDF/B-V cross section data were used after being fitted with analytical functions to reduce the data storage requirements.

Sanders (1983) applied the multi-group Monte Carlo method to the problem of geologic formation analysis in oil exploration by modeling neutron interactions to demonstrate the ability of the Monte Carlo method to simulate complex geometry problems and to analyze neutron and gamma ray transport in the field of applied earth sciences.

The use of the Monte Carlo technique to optimize the geometrical configuration of an on-line capture gamma ray analyzer has been reported by Lukander and Uusitalo (1978).

Thomas *et al.* (1983) reported on a towed seabed spectrometer for mineral exploration, based on both natural and neutron induced gamma rays. Monte Carlo calculations were used to simulate the

experimental probe and to estimate the effective sampling depth by simulating the depth of penetration of neutrons into the seabed and the subsequent attenuation of capture gamma rays returning to the detector. The results were represented as sectional contours of contributions to the detector. Monte Carlo calculations were also used to simulate an artificial seabed of sand containing varying concentrations of copper and manganese to investigate the non-linear relationship between count rate and elemental concentration for trace elements with significantly large neutron absorption cross sections.

Monte Carlo modeling to describe the design and calculation of capture gamma-ray analysis systems has been demonstrated for coal and compared with experiments (Schmidt and Rose, 1984). The general Monte Carlo program SAM-CE (Monte Carlo System for Radiation Transport and Criticality calculations in complex configurations, developed at the Electric Power Research Institute) has been modified to have the capability of predicting strong discrete gamma ray lines and used with ENDF/B-V cross sections (including gamma ray production data) to calculate a complete gamma ray spectrum. It seems that the model uses the detector response function to predict the instrument response.

Rainbow (1985) used the general purpose Monte Carlo code MORSE and nuclear data derived from ENDF/B-IV to model a conveyor belt iron ore analyzer which detects thermal neutron capture gamma rays from Fe-56. A multi-group energy treatment was used with processed multigroup cross sections for the analyzer materials averaged over

the slowing-down neutron spectrum from a uniformly distributed Cf-252 fission source in an infinite polyethylene moderator. A user supplied patch to model the Cf-252 source as a point fission source with a Maxwellian spectrum was used. The author concluded that such simulation would be possible provided that the efficiency of the calculations was improved. Some form of correlated sampling is recommended to improve the efficiency of simulating a number of similar systems. Due to the smearing effects of multigroup energy treatment, only simple gamma ray spectra could be treated. Otherwise a continuous energy treatment, such as is incorporated in the MCNP code (a general purpose Monte Carlo code developed at Los Alamos National Laboratory), has to be used.

The trend of research to understand the influence of perturbing factors on neutron transport, such as construction materials, sample constituents and physical state, and hence to make allowance in equipment design and data interpretation, is leaning heavily on neutron transport studies by Monte Carlo techniques.

2. REVIEW OF APPLICABLE NEUTRON AND GAMMA RAY PHYSICS

In this chapter, a general review of the interaction of neutrons with matter and the governing equations that describe the mechanics of such interactions are discussed along with the origin, attenuation, and penetration of associated capture gamma rays within a medium. The significance of the interactions and effects on this work is emphasized.

2.1 Neutrons

Throughout this discussion, neutrons are pictured as very small spheres and their wave characteristics are ignored except in the case of thermal neutrons with energies at thermal equilibrium with the atoms in the surrounding medium. The deBroglie wavelength associated with such a neutron (0.0253 eV energy at room temperature), is 18 nm and is comparable to the lattice parameters. This is of significance in considering thermal neutron cross sections (Section 2.1.4). Furthermore, any relativistic effects are ignored since even a neutron with an energy as high as 5 MeV would have a speed of only ~1% of the speed of light. Beta decay of a free neutron (half-life of 11.7 minutes) is not considered when compared with the time scale of the events of interest. Neutron polarization (up or down ½ spin) is not considered, since this is only of significance in determining the azimuthal angle of neutron scattering reactions.

A very important feature of neutron transport is that, being

neutral, the electromagnetic fields of the atoms that comprise the medium where the neutron is being transported play no role in the interactions. Therefore, the path that neutrons transcribe between collisions is a straight line.

2.1.1 Neutron Sources and Associated Neutron Spectra

Excluding the bulkier nuclear reactors and accelerators, practically portable neutron sources can be categorized into:

A. Radioisotopic decay sources

Many heavy radioisotopes decay by spontaneous fission and in the process emit neutrons. Among these is Cf-252. The artificially produced Cf-252 is considered a highly practical neutron source for research and engineering measurements. It has a half-life of 2.65 years and decays 97% by alpha emission and 3% by spontaneous fission with the emission of an average of 3.5 neutrons per fission. On a unit mass basis, 2.3×10^6 neutron/s are produced per μg of Cf-252. The energy spectrum of the neutrons is reported (Boldeman *et al.*, 1979) to be accurately represented by:

$$\chi(E) = \frac{2}{\pi^{1/2}} T^{-3/2} E^{1/2} e^{-E/T} \qquad (2.1.1\text{-}1)$$

$$\text{with} \quad T = 1.424 \text{ MeV}$$

The mean energy of this spectrum is 2.136 MeV which is appreciably lower than that of the isotopic sources discussed below. Furthermore, the specific yield of neutrons is higher and the associated gamma ray yield is lower than the isotopic sources. The

Cf-252 source is considered to be more appropriate for neutron capture reactions, which are characterized by large thermal neutron absorption cross sections for many elements.

B. Isotopic sources

Neutrons can be produced by (α,n) and (γ,n) reactions. One such compact source that is commercially available is a mixture of Be-9 and an α-emitting radioisotope, such as Po-210, Pu-239, Ra-226, or Am-241, that through the reaction $^{9}Be(\alpha,n)^{12}C$ produces neutrons having a spectrum of energies from 0 to about 11 MeV with an average neutron energy of about 4.5 MeV.

The (γ,n) reaction on a Be-9 has a threshold energy of 1.665 MeV; radioisotopes with both practical half-lives and gamma radiation with an energy above 1.665 MeV are rare. One such candidate (Sb-124) has a relatively short half-life of about 60 days. The average energy of the neutrons produced by the antimony-beryllium $^{9}Be(\gamma,n)^{8}Be$ source is about 0.0223 MeV (Knoll, 1979). All isotopic neutron sources give yields from about 2×10^{6} to 1×10^{7} neutron/s per curie of initiating radioisotope.

C. 14-MeV compact d-t neutron generators

These generators make use of either the $^{3}H(d,n)^{4}He$ or $^{2}H(d,n)^{3}He$ reactions. In the former case, neutrons are produced with an energy of 14 MeV and high yields can be obtained. The latter reaction has a lower yield with lower neutron energies. The high energy neutrons are suitable for methods based on inelastic

scattering, and the generator has the advantage that it can be turned off when it is not in use, thus reducing unnecessary exposures and irradiations. By pulsing the neutron generator, it is possible to separate the gamma ray spectrum produced by neutron inelastic scattering from those excited in neutron capture reactions. In addition to being expensive, the neutron flux is not reliably steady and the lifetime of the generator tube is limited.

2.1.2 Neutron Interactions

Upon collision of a neutron with a nucleus, one of the following interactions may take place depending on the neutron energy and the nucleus involved:

A. Absorption

In the absorption reaction, the neutron totally disappears and is replaced by one or more secondary radiations. The absorption reaction leads to the formation of a compound nucleus in an excited state that might persist anywhere from 10^{-14} s to years depending on the nucleus and the state in question. The excited compound nucleus may decay, with a finite probability, by one of the following modes:

1. Charged particle emission: (e.g., (n,α), (n,p), etc.). The compound nucleus becomes de-excited by emitting a charged particle (proton, deuteron, α-particle, or occasionally an electron). From the viewpoint of neutron population, the process results in the loss of a neutron and hence is equivalent to a neutron capture.

2. Neutron capture: (n,γ). The compound nucleus de-excites almost instantaneously by emitting a γ-ray. Often the nucleus is still not stable after the γ-ray emission, and a β-decay follows. This reaction is the prime origin of the characteristic capture gamma rays discussed in Section 2.2.1. The effect on the neutron population is a loss of the captured neutron.

3. Neutron producing reaction: ((n,xn), where x is an integer ≥ 2). The compound nucleus de-excites by emitting two or more neutrons. The neutron population is considered to be increased, and thus this reaction is similar to a fission event from a neutron economy standpoint.

4. Fission: The compound nucleus de-excites by a nuclear fission, splitting into two large fragments (and one light fragment in the rare ternary fission reaction) along with the instantaneous emission of generally from one to three free neutrons, of which a small fraction of about 0.65% are delayed neutrons. This mode effectively increases the neutron population.

B. Scattering

In scattering reactions, a neutron re-emerges after getting close enough to the nucleus to experience the nuclear force. The time involved in the formation of the compound nucleus and the de-excitation is very short. This reaction is classified further into:

1. Elastic scattering: A neutron is emitted and the nucleus returns to its initial ground state. The emitted neutron need not be the same one that originally interacted with the nucleus. The lifetime of the excited compound nucleus is so short ($\sim 10^{-12}$ s) that for practical purposes, the collision process may be analyzed as a "billiard-ball" collision. This type of elastic scattering is called resonance scattering and is very rare. A more common form is potential scattering, in which the impinging neutron does behave exactly like one billiard ball striking another (the nucleus). As judged by the time involved ($\sim 10^{-22}$ s), the neutron interacts with the nucleus as a whole without forming a compound nucleus. Thus, whether the elastic scattering is anomalous resonance scattering or the common potential scattering, the billiard ball model that pictures the original neutron as striking the nucleus (causing it to recoil) and moving off in a direction different from its original flight path is adequate to analyze the process. Elastic scattering is an extremely important process since it is the chief mechanism in neutron thermalization by which the high energy neutrons lose their kinetic energy.

2. Inelastic scattering: $(n,n'\gamma)$. A neutron is emitted from the compound nucleus, but the nucleus still remains in an excited state, usually the first excited state, which decays promptly, generally with the emission of only one gamma ray. The time involved in the process ($\sim 10^{-12}$ s) is effectively

instantaneous. Theoretical models usually account for the large amount of energy lost by the neutron in the scattering process to be responsible for the nucleus remaining in an excited state.

2.1.3 Nuclear Cross Sections

Before any mathematical representations of neutron interactions can be formulated, the concept of nuclear cross sections has to be presented.

To obtain a quantitative measure of the events (absorption, scattering, etc.) that may take place when a neutron interacts with a nucleus, it is in order to define quantities which specify the probability that a neutron, having a given kinetic energy and moving through a medium containing a given material, will interact in a certain manner. It must be understood that these quantities are probabilities and one cannot predict exactly which event will occur in a particular case. However, given that only absorption and scattering are the two possible events among the statistical ensemble, and, say $p_{absorption} = 0.3$ and $p_{scattering} = 0.7$, then one can predict that 30% of the events will be absorptions and 70% of the events will be scatterings.

Physicists have introduced the concept of a nuclear cross section by specifying the probability of an interaction, picturing the nucleus as presenting an "unshadowed" cross sectional area to a neutron traveling through a medium. Adopting this concept of cross section literally would require that the nucleus adjust its "size"

in accord with the energy of a neutron about to hit it, since it is known by measurements that the probability of interaction depends on the kinetic energy of the neutron. The cross section is then not to be taken as a literal, but only a convenient, way of expressing the probability of an interaction to take place. Thus, the microscopic cross section for the interaction by a specific process between a nucleus and a passing neutron can be defined in terms of the probability that an interaction of type s will take place when a neutron having kinetic energy E moves a distance dx in a medium containing N_j atoms of isotope j per cm^3, namely $N_j \sigma_{s,j}(E)\, dx$. In this definition, it is understood that, since the probability of interaction depends on the relative kinetic energy between the neutron and the target nucleus, an average over the thermal motions of the nuclei has been performed. Thus, one should think of the $\sigma_{s,j}(E)$ as depending implicitly on the temperature of the isotope j and consider E as the kinetic energy of the neutron relative to the laboratory system. This temperature dependence of $\sigma_{s,j}(E)$ is important when the neutron energy is in the thermal energy range ($0 < E \leq 1$ eV) where the speed of the neutron is comparable to the thermal motion of the nuclei comprising the medium; this effect is further investigated in Section 2.1.4. Another situation, when the energy of the neutron corresponds to a "resonance energy" of the nucleus it strikes, causing the "Doppler broadening", is also referred to in Section 2.1.4.

The product $N_j \sigma_{s,j}(E)$ is labeled the macroscopic cross section, which may be used to define the probability of occurrence

less ambiguously as: the macroscopic cross section is the probability per unit path length in a material that a neutron of energy E will undergo an interaction of type s with material j.

With the above in mind, it is customary to speak of cross sections for all possible nuclear processes (scattering, absorption, etc.).

2.1.4 Characteristics of Nuclear Cross Sections

The neutron energy range of interest in this work extends to the highest neutron energy emitted by the Cf-252 source. It is can be shown that the probability that a neutron emitted from Cf-252 has an energy greater than 5 MeV is less than 0.05 (Profio, 1979). Therefore, the upper limit can be safely assumed to be, say, 10 MeV, and the energy behavior of neutron cross sections in this range of interest for the nuclei comprising the monitoring system is addressed next.

A. Behavior of neutron absorption cross sections

General behavior for the neutron absorption cross section of all elements tend to vary as $E^{-\frac{1}{2}}$ (one over v behavior) at low (< 2 eV) energies. For most light nuclei the 1/v behavior persists up to higher energies. However, for intermediate and heavy nuclei, the curve of $\sigma(E)$ versus E exhibits very high and very sharp peaks (resonances) begining in the energy range just above thermal. These peaks are due to the existence of metastable energy levels in the excited nucleus. Physically, the formation of the compound nucleus

is strongly favored when the total excitation energy of the nucleus corresponds to that of the metastable level. The total available excitation energy being the kinetic energy of the neutron about to strike the nucleus in addition to the potential energy released (binding energy) when that neutron enters the potential field of the nuclear force. Most of the resonance peaks are due to neutron absorptions although the asymmetric dipping just beyond each resonance is a scattering effect explained by quantum mechanics. The resonance widths are very narrow and, because the target nuclei are in motion, are dependent on the relative motion of the target nuclei. These resonances are said to be Doppler-broadened with increasing target nuclei temperature.

Care must be practiced when nuclear cross section data are obtained. For instance, capture cross section data for a free Na-23 nucleus at 0 ^{o}K and 300 ^{o}K obtained from the Evaluated Nuclear Data File (ENDF/B-V) are shown in Figure 2.1.4-1; comparison of the two curves clearly shows the Doppler broadening effect of the resonances, indicated by the decrease in the peak magnitude of the cross section value at the resonance energy. It is feasible to account for the Doppler-broadening theoretically using the Breit-Wigner formula for the isolated resonances, when it is deemed that this adjustment is significant. At neutron energies above a few hundred eV, the resonance peaks become lower and broader. Due to the lack of precise measurements of $\sigma_{s,j}(E)$ in this energy range and the closeness of the nuclear levels, the curve takes on a smooth "unresolved resonances" appearance.

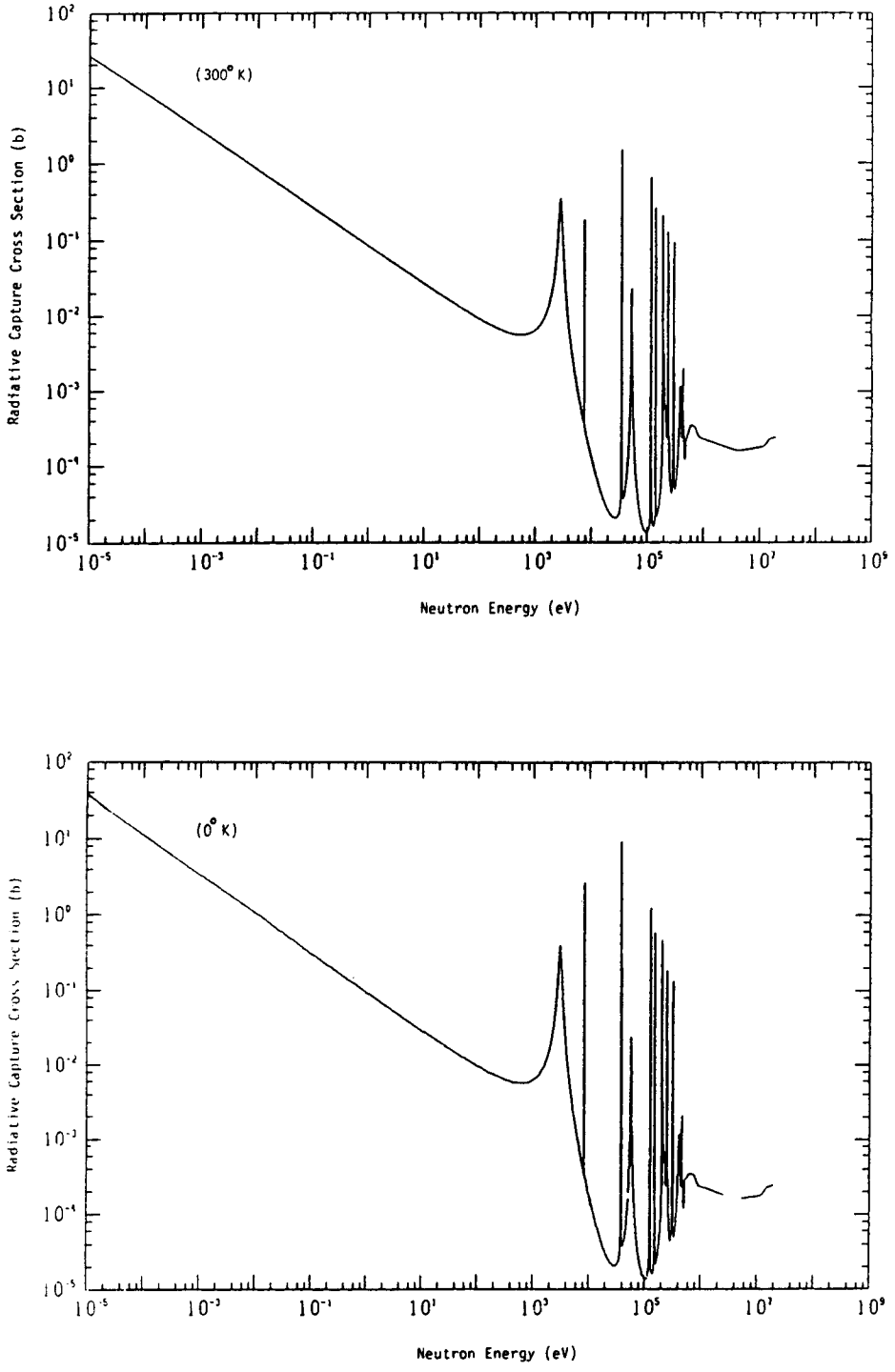

Figure 2.1.4-1 Na-23 Radiative capture cross section as a function of incident neutron energy given at 300^0 K (top) and at 0^0 K (bottom) (ENDF/B-V data).

Absorption cross sections are not affected by the absorber atom nucleus being in a bound state in a molecule or in a crystal lattice or by being free. Therefore, the cross sections can be taken to be the same for bound atom nuclei as for free atom nuclei (Bell and Glasstone, 1982).

B. Behavior of neutron scattering cross sections

Scattering cross sections for low energy neutrons interacting with most elements are elastic, roughly constant as a function of energy, and small in magnitude. Important exceptions to this rule occur when the atomic nucleus with which the neutron is interacting is bound chemically in molecules (not free) to other atomic nuclei or in part of a crystalline structure; under these conditions, low energy neutrons (with wavelength in the order of the lattice parameters) will Bragg scatter and tend to interact with several nuclei at once. The nucleus in a bound state cannot recoil freely in a collision. Instead there is an interaction between the scattering atomic nucleus and its neighbors in the molecule or solid.

The kinematics of two-body interactions considers the reduced mass of the neutron-nucleus system; in heavy nuclei the reduced mass is practically equal to the neutron mass and the ratio of the scattering cross section for the bound atom to the free atom is essentially unity. Nevertheless, for light nuclei (e.g., H), the reduced mass effect is pronounced. Furthermore, the scattering is

often inelastic, some of the incident kinetic energy of the neutron being retained by the molecule in the form of excited vibrational or rotational motions of its constituent atoms. It is a formidable effort to apply free hydrogen scattering data in the case of bound hydrogen in molecules even after theoretically accounting for some of the aforementioned effects (e.g., the Nelkin model). Furthermore, the effect of the target nucleus motion as a function of temperature that affects the interaction at low neutron energies cannot be ignored as shown in Figures 2.1.4-2. Thus, in general, the scattering cross sections depend on the physical and chemical forms and temperature of the scattering material.

Figure 2.1.4-3 schematically shows the origin of the delayed gamma radiation resulting from the activation of heretofore stable elements with neutrons, thereby rendering them radioactive, which in turn decay by emitting nuclear radiation specific to each element. This process is utilized in the conventional NAA, whereas the NCPGA utilizes the radiation emitted at the time of neutron activation rather than that emitted from the de-excitation of the newly-formed daughter nucleus. Furthermore, Figure 2.1.4-3 schematically shows the functional dependence of the capture, elastic, and inelastic cross sections on the neutron kinetic energy exhibiting resonance behavior at those energies at which the center-of-mass energy E_{cm} plus the neutron binding energy match an energy level of the compound nucleus.

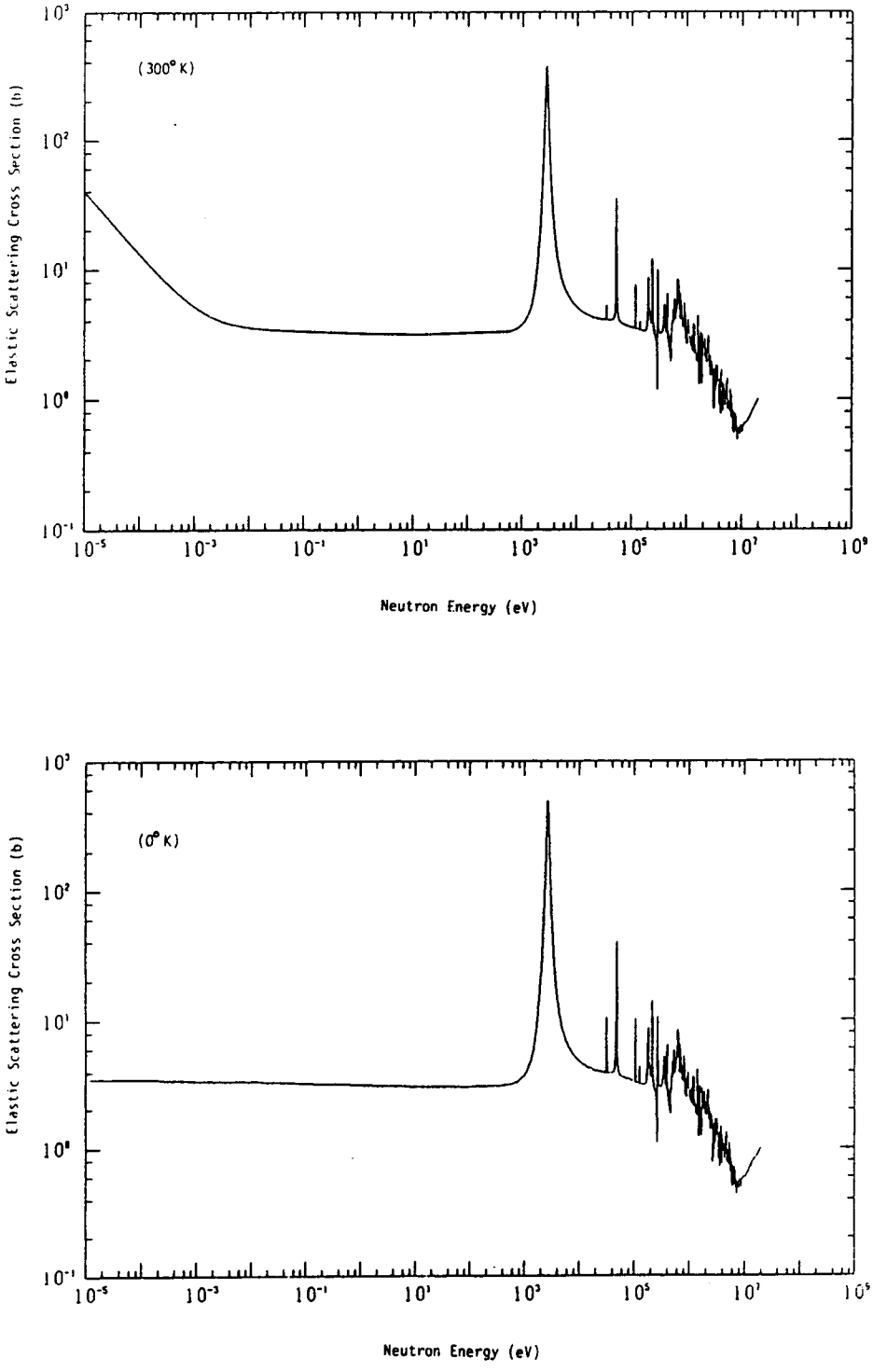

Figure 2.1.4-2 Na-23 Elastic scattering cross section as a function of incident neutron energy, given at 300^0 K (top) and at 0^0 K (bottom) (ENDF/B-V data).

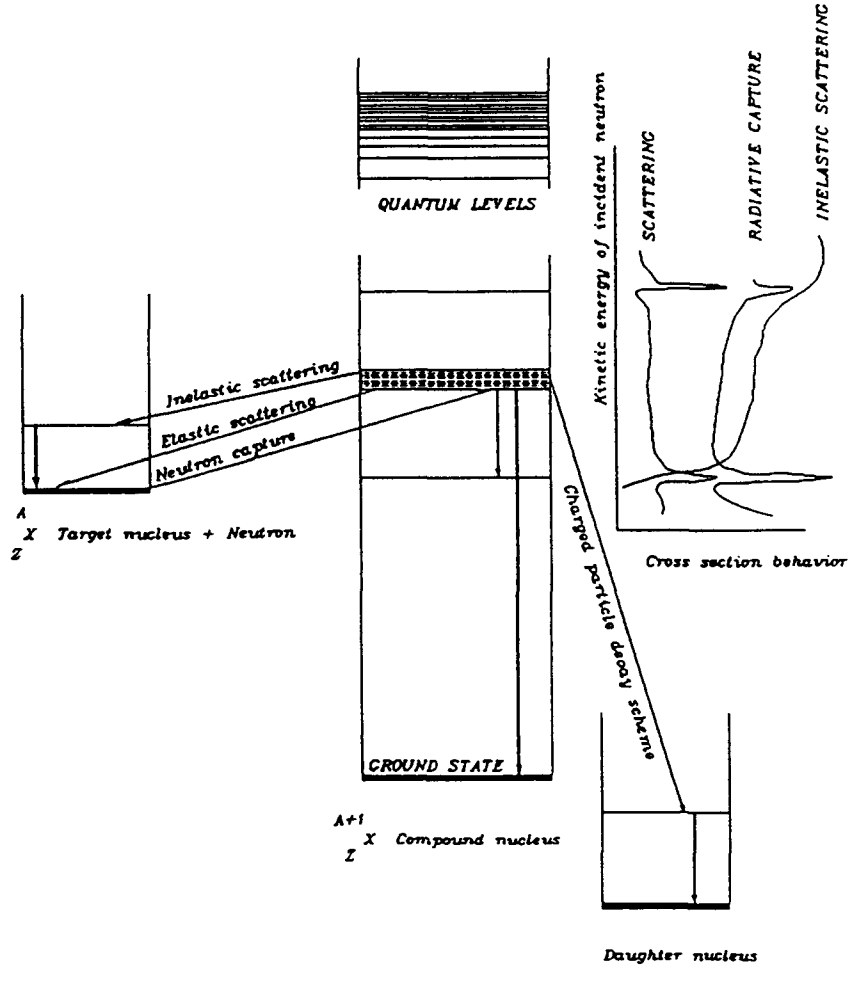

Figure 2.1.4-3 Schematic representaion of the origin of the prompt capture gamma rays.

2.1.5 Mathematical Representation of Neutron Interactions

Quantitative mechanics of the neutron absorption reaction are not needed in this work since a neutron undergoing absorption is considered lost. The path length that a neutron traverses between collisions is discussed in Appendix A. Radiative capture is discussed qualitatively in Section 2.2, since it is the origin of the prompt gamma rays of interest.

Neutron scattering representations and models are investigated and the models used in this work are outlined. Neutron scattering reactions may be categorized according to the interacting neutron energy into:

A. Thermal Scattering

At thermal neutron energies, where the interacting neutron kinetic energy is comparable to the thermal agitations of the target scattering nuclei, the latter can no longer be regarded as being at rest. Therefore, it is possible that the neutron gains energy, by upscattering, as well as loses energy in collisions. In addition, molecular and crystal binding and wave interference effects have to be accounted for. As mentioned before, since the cross section is averaged over the target nuclei velocity distribution, one expects the cross section behavior to be temperature dependent. By using data at the appropriate temperature, no special considerations are necessary for radiative capture. On the other hand, the neutron scattering model has to be modified significantly to account for the

possibility that the colliding neutron may gain or lose energy in the collision. Chemical binding, thermal vibrational and rotational modes of molecules of the target nucleus, and crystalline effects may be incorporated into the adopted model, depending on the sophistication of the model.

The $S(\alpha,\beta)$ scattering law is the most rigorous treatment and is derived from quantum mechanical theory of neutron scattering from a system of bound nuclei. The α and β (dimensionless momentum and energy exchange) parameters uniquely determine the kinetic energy and scattering angle of the emerging neutron in the laboratory system. This model requires the storage of only two-dimensional arrays (Bischoff *et al.*, 1972).

The monatomic gas model, in which the moderating atoms (nuclei) are modeled as being a monatomic gas in which there is no chemical binding among molecules, is considered to be a good approximation (Carter and Cashwell, 1975). The energy distribution among the atoms is the Maxwell-Boltzmann distribution, which accounts for the thermal motion, and results in upscatterings and yields a good approximation to the thermal neutron energy distribution. It is considered to be a good approximation when chemical binding effects may be ignored or adequately described by various approximations. The inherent assumption in this model is that the neutrons are transported in a monatomic gas of the moderating nuclei; the gas is assumed to have a Maxwellian velocity distribution:

$$p(V)\ dV = \left(\frac{A}{2\pi kT}\right)^{3/2} V^2\ e^{-\frac{AV^2}{2kT}}\ dV\ d\theta\ d\phi \qquad (2.1.5\text{-}1)$$

The scattering is assumed to be elastic (no inelastic energy loss as vibrational, rotational, etc.) and further assumed to be isotropic in the center-of-mass system, since the thermal target motion tends to make the scattering more nearly isotropic.

The energy available for an interaction is the sum of the kinetic energy of the neutron and the nucleus with respect to their center-of-mass. This reduced mass ($\tilde{m}$) energy is given by:

$$E_{cm} = \frac{1}{2} \tilde{m} v_r^2 \qquad (2.1.5\text{-}2)$$

where $\tilde{m} = mM/(m+M)$, m and M are the mass of the neutron and the nucleus, respectively, and v_r is the relative speed of approach. The relative velocity obtained by the cosine law is given by:

$$v_r = \sqrt{v_n^2 + V^2 - 2v_n V \cos\psi} \qquad (2.1.5\text{-}3)$$

where ψ is the angle between the velocity vectors of the neutron v_n and the nucleus V. The total interaction rate for all nuclei is therefore:

$$\Phi \; N \; \bar{\sigma}(E,T) = \int_V n \; v_r \; \sigma(E_{cm}) N(V) \; dV \qquad (2.1.5\text{-}4)$$

since $\Phi = nv_n$ where v_n is the speed of the neutron and Φ is the neutron flux. The effective scattering cross section in the laboratory system for a neutron is:

$$\sigma_s^{eff}(E,T) = \frac{1}{N v_n} \iint v_r \; \sigma(v_r) \; N \; p(V) \; dV \; d\Omega \qquad (2.1.5\text{-}5)$$

If it is assumed that the scattering cross section of the nucleus is independent of this relative velocity, i.e.,

$$\sigma(E_{cm}) = \sigma_s^0 = \text{constant}$$

with β defined as:

$$\beta = \sqrt{\frac{A}{2kT}} \qquad (2.1.5\text{-}6)$$

and a new variable x defined as :

$$x = \beta V = \sqrt{\frac{AV^2}{2kT}} \qquad (2.1.5\text{-}7)$$

then Equation (2.1.5-1) in terms of the transformed dimensionless variable x can be rewritten as:

$$p(x)\, dx = \frac{4}{\sqrt{\pi}} x^2 e^{-x^2} dx \qquad (2.1.5\text{-}8)$$

and Equation (2.1.5-5) can be written as:

$$\sigma_s^{eff}(E,T) = \frac{1}{v_n} \int_0^{\infty} \frac{\sigma_s^0 \beta^3 V^2 e^{-\beta^2 V^2}}{\pi^{3/2}} \int_0^{2\pi} d\phi \int_{-1}^{1} \sqrt{v_n^2+V^2-2v_n V\mu}\; d\mu dV \qquad (2.1.5\text{-}9)$$

The integral over the cosine variable yields:

$$\int_{-1}^{1} \sqrt{v_n^2+V^2-2v_n V\mu}\, d\mu = \frac{1}{-3v_n V}\left[(v_n^2+V^2-2v_n V)^{3/2} - (v_n^2+V^2+2v_n V)^{3/2} \right] \qquad (2.1.5\text{-}10)$$

and Equation (2.1.5-9) becomes:

$$\sigma_s^{eff}(E,T) = \frac{2\sigma_s^0}{3\pi^{1/2} v_n^2} \int_0^{\infty} \left[(v_n+V)^3 - |v_n-V|^3 \right] \beta^3 V e^{-\beta^2 V^2}\, dV \qquad (2.1.5\text{-}11)$$

Implementation of this method to sample thermal scattering reactions is discussed in Section 5.4.2.1.

B. Non-thermal scattering

When the incident neutron energy is in excess of a value of the order of 2 eV, the thermal motion of the scattering nuclei may be neglected and the nucleus can be assumed to be at rest in the lab system. Furthermore, the nuclei (or atoms) may be treated as being free because the binding energy in a molecule is not significant in comparison with the energy involved in the neutron-nucleus interaction. The scattering (slowing down) process may be described by elastic or inelastic scattering.

Classical "billiard ball" elastic scattering model:

This is a two-body final constellation elastic scattering model of a neutron from a free nucleus and is considered to be a satisfactory approximation of the elastic scattering when the kinetic energy of the incident neutron is greater than about ten times the equilibrium kinetic energy of the target nuclei (Carter and Cashwell, 1975). Details for derivation of this model can be found in virtually every book in the field of nuclear engineering. It should be understood that this representation is derived with the target nucleus at rest, which is not a serious limitation when the neutron speed is considerably greater than the thermal agitation velocities of the target nuclei (a good assumption for neutron energies greater than about 2 eV). The neutron energy E', in the

laboratory system, after being scattered from a stationary nucleus of mass A (units of neutron mass) through a polar angle ψ (relative to the incident neutron direction Ω), in the center-of-mass system, is related to the initial incident neutron energy E by the equation:

$$\frac{E'}{E} = \frac{A^2 + 2A\cos\psi + 1}{(A + 1)^2} \qquad (2.1.5\text{-}12)$$

where A = M/m, M and m are the mass of the scattering nucleus and the neutron, respectively. The corresponding polar scattering angle θ in the laboratory system can be obtained as:

$$\cos\theta = \frac{A\cos\psi + 1}{\sqrt{A^2 + 2A\cos\psi + 1}} \qquad (2.1.5\text{-}13)$$

In the special case of collisions with hydrogen (A~1) and for an isotropic distribution of ψ, the scattered neutron energy is uniformly distributed in the interval (0 to E) and the scattering angle θ in the laboratory system is given by:

$$\cos\theta_H = \sqrt{\frac{1 + \cos\psi}{2}} \qquad (2.1.5\text{-}14)$$

The angular distribution of elastically scattered neutrons, when viewed in the center-of-mass system, can be assumed to be isotropic at low incident neutron energies for all elements. This approximation deteriorates with increasing neutron energy or increasing target nucleus mass. Above about 0.1 MeV, elastic scattering is anisotropic for most nuclei with the exception of hydrogen, where it can be assumed to be isotropic for energies of the incident neutron up to about 15 MeV. The scattering in the

azimuthal angle ϕ to the incident neutron direction is always uniform unless the scattered neutrons are polarized (possessing uniform up or down ½ spin). Thus, the angular distribution for elastically scattered neutrons is given by:

$$p(\psi,\theta)\ d\psi\ d\theta = \frac{1}{4\pi}\ \sin\psi\ d\psi\ d\theta \qquad (2.1.5\text{-}15)$$

In the case when the angular distribution of the scattering angle is not isotropic, the anisotropic scattering law (supplied in file 4 in ENDF/B-V)(Kinsey, 1979) is represented for a specific reaction type as discrete values at a series of incident neutron energies.

Discrete level and evaporation inelastic scattering models:

Treatment of the inelastic scattering reactions is handled through the use of the discrete level energy loss model that assumes the scattering to be isotropic in the center-of-mass system. This model uses values of the inelastic excitation level energies along with a probability for each one. If the neutron energy is below a certain excitation energy, that level cannot be excited. Therefore this reaction is a threshold reaction and cannot take place unless the kinetic energy of the colliding neutron exceeds this energy threshold.

The excited nucleus may be elevated to one of a number of possible levels; the levels are fairly widely spaced and have well known thresholds and probabilities of excitation at a given incident neutron energy. For such discrete levels, the incident

neutron energy degradation can be represented by (Schaeffer, 1973):

$$\frac{E'}{E} = \frac{1}{(A+1)^2}\left[1+A^2\left(1-\frac{\epsilon}{E}\right)+2A\cos\psi\left(1-\frac{\epsilon}{E}\right)^{1/2}\right] \quad (2.1.5\text{-}16)$$

where E' = the neutron energy after being scattered

E = the incident neutron energy that will result in the excitation of a discrete level

ϵ = the excitation energy required to excite the discrete level in question

ψ = the scattering angle in the center-of-mass system, and

A = the scattering nucleus mass ratio (units of neutron mass)

The corresponding laboratory polar scattering angle θ is given in this case by

$$\cos\theta = \frac{1 + A\cos\psi\left(1-\frac{\epsilon}{E}\right)^{1/2}}{\sqrt{1 + A^2\left(1-\frac{\epsilon}{E}\right) + 2A\cos\psi\left(1-\frac{\epsilon}{E}\right)^{1/2}}} \quad (2.1.5\text{-}17)$$

For large A, an approximate relation for the energy after scatter is

$$E' = E - \epsilon \quad (2.1.5\text{-}18)$$

As the excitation energy increases, the levels become increasingly more closely spaced, until the individual levels are no longer resolvable at the "continuum threshold". The probability for the target nucleus to be excited to an infinitesimal energy band

within the continuum is well-known as a function of neutron energy. The probability distribution that a neutron will be emitted with an energy between E' and $E'+dE'$ when the incident neutron energy is E for inelastic scattering model, derived from the liquid-drop nuclear model, is given by (Lamarsh, 1972):

$$p(E') = \frac{E'}{T^2} e^{E'/T} \qquad (2.1.5\text{-}19)$$

with a nuclear temperature

$$T = 3.2 \sqrt{\frac{E}{A}} \qquad \text{(MeV)}$$

The angular distribution of inelastically scattered neutrons is typically isotropic in the center of mass system for neutron energies up to approximately 10 MeV.

2.2 Gamma Rays

2.2.1 Prompt Gamma Ray Source and Associated Gamma Ray Spectra

The radiative capture reaction is the prime source of capture prompt gamma rays. This reaction can take place at all incident neutron energies of interest here, although the probability is usually highest at thermal energies. Upon capture of a neutron into the nucleus, the nuclear binding energy of the neutron to the nucleus, which ranges from 2.2 MeV in hydrogen to 11 MeV in nitrogen (Garrett *et al.*, 1973) is usually divided among 1 to 5 photons. The spectra of most nuclides are fairly complex with discrete energies ranging up to the value of the neutron binding energy of the compound nucleus. The Porter-Thomas distribution implies that the

spectrum results from widely fluctuating transitions to a set of final nuclear states, and thus each nuclide will display a spectrum unique to the thermal neutron capture for that specific nuclide. The elemental spectra will be comprised of the weighted contributions for the several naturally occurring isotopes of that element. The shape (relative intensities) of the prompt gamma ray line spectrum is dependent upon the incident neutron energy (Senftle *et al.*, 1974).

Therefore, the spatial and energy distribution of the neutron field, caused by one or more of the variations in the type and abundance of major constituents, density changes, moisture content, presence of low-abundance strong neutron absorbers (neutron poisons), and temperature changes, affects gamma ray emission and absorption. Measurements of prompt gamma ray intensities reported by Lone *et al.*, (1981) are made at thermal energies, and serious errors can result from applying these data to epithermal captures. This is especially significant in media for which the fraction of epithermal capture is appreciable. Thus, radiative capture is an elementally and energetically specific reaction. In principle, the gamma rays following the neutron capture can be identified by energy and, provided there exists an appropriate calibration, the concentration of the associated element can be determined.

2.2.2 Quantitative Representation of Gamma Ray Attenuation

Analogous to the concept of macroscopic cross sections for neutron interactions, the probability that gamma ray event s takes

place per unit path length in the material is defined to be μ_s. The sum of probabilities for all possible events that might occur throughout the path of the gamma ray defines the probability per unit path length (the linear attenuation coefficient) that the gamma ray photon is removed from the beam :

$$\mu = \mu_{pe} + \mu_{cs} + \mu_{pp}$$

where the customary nomenclature for the three major gamma ray mechanisms of interactions are used.

The number of uncollided photons (I) passing through a distance x in a medium with a linear attenuation coefficient μ is then given in terms of the original unattenuated intensity I_0 before the transmission as:

$$I = I_0 \, e^{-\mu x} \qquad (2.2.2\text{-}1)$$

To overcome the drawback that the linear attenuation coefficient varies with the density of the absorber, even though the absorber material is the same, the mass attenuation coefficient is widely used and defined as (μ/ρ). Thus, for a given gamma ray energy, the mass attenuation coefficient does not change with the physical state of the absorber. For instance, (μ/ρ) for water does not depend on the absorber being in the liquid or vapor state.

The mass attenuation coefficient of a compound or mixture of elements can be calculated from:

$$\left(\frac{\mu}{\rho}\right)_{\text{compound}} = \sum_i w_i \left(\frac{\mu}{\rho}\right)_i \qquad (2.2.2\text{-}2)$$

where w_i is the weight fraction of element i in the compound or

mixture.

2.2.3 Interactions of Gamma Rays

Since in this work the detailed transport and tracking of gamma rays is not performed, only their penetration is of interest. A brief qualitative review of the major mechanisms of interactions of gamma rays in matter is discussed, enough to clarify the concept of the attenuation coefficient that is used to quantitatively describe the response of interest in a radiation detector, namely the photopeak.

Although a large number of possible interaction mechanisms are known for γ-rays in matter, types can be confined to three mechanisms that result in the partial or complete transfer of the γ-ray energy to an electron, thus resulting in abrupt changes in the gamma ray history, in that the photon either disappears entirely or is scattered through a large angle with a decrease in energy.

A. Photoelectric absorption

The incoming photon interacts with the atom of the material as a whole, in which case the photon completely disappears and an energetic photoelectron is ejected from one of the bound electron shells of the atom. This interaction cannot take place with a free electron.

B. Compton scattering

The incoming photon interacts with an atomic electron with the

result that the γ-ray is deflected with respect to its original direction and the electron is recoiled. All angles of scattering are possible.

C. Pair production

This is a threshold reaction, possible to take place when the energy of the incident γ-ray exceeds twice the rest mass energy of an electron (1.022 MeV). In the interaction, which must take place in the coulomb field of a nucleus, the photon disappears and is replaced by an electron-positron pair. The excess energy above the 1.022 MeV threshold is shared by the created e^-e^+ pair. The positron will subsequently annihilate after slowing down in the material and produce two annihilation photons of 0.511 MeV energy and opposing directions.

2.2.4 Gamma Ray Build-up

The intensity of the gamma radiation from a source may be considered to be composed of primary (uncollided) and scattered radiations. Buildup factors have been calculated or measured for various gamma ray energies and for various absorbers and sources (Cember, 1978) to account for the contribution due to scattered radiations. The use of this buildup factor is not applicable in this work since it is considered that only the unscattered capture gamma rays will contribute to the full energy peaks, and the scattered gamma ray contributions represent a background under the peaks that can be extracted.

3. REVIEW OF MONTE CARLO TECHNIQUES IN NEUTRON TRANSPORT

Monte Carlo is a statistical procedure wherein the expected characteristics of a neutron population in an assembly are estimated by drawing samples from a large number of histories of neutrons whose individual "lives" are simulated and tracked by a computer code.

3.1 General Characteristics

The probabilistic Monte Carlo method essentially consists of following individual histories of the neutron of interest from "birth" to "death" by randomly sampling parameters such as the possible angles, path lengths, and energies from the appropriate probability density functions of the pertinent interactions with matter. The yield or the number of scored events of interest divided by the total number of histories (for a large number of histories) is an estimate of the probability of occurrence of the phenomenon of interest. "Crude" or hit-or-miss Monte Carlo techniques use the above-mentioned procedure. If a sufficient number of particles are tracked, parameters of interest can be scored with acceptable statistical errors, as discussed in Section 3.1.2. It can be seen that a large number of histories is usually required to attain a reasonable accuracy. In fact, for events of interest that have a small probability of occurrence, this number may be so large that it precludes the use of this method, since much of the time would be spent, for example, tracking particles which

are moving in regions where there is a very low probability of their influencing the detector count rate (the parameter being sought). However, a Monte Carlo approach can deal with complex source distributions over space and energy, with asymmetric geometries through which the particles move, and with the direct usage of detailed nuclear data (not averaged over energy groups). A class of techniques referred to as variance reduction is useful to reduce the number of histories required to attain a given accuracy so that most of the computing time will be spent tracking particles which have a good chance of contributing to the detector counts.

3.1.1 Variance Reduction Methods

From the point of view of particle transport, these methods may be classified into:

A. Exact analytical replacement

Part of the problem under consideration is solved analytically or experimentally and used in the problem to replace the Monte Carlo simulation of that part. For instance, the mechanics of interactions and their approximations by Monte Carlo methods inside a detector's effective volume that result in a desired response may be bypassed and replaced by an experimentally determined energy-dependent detector efficiency with which to multiply the incident fraction of radiation to yield the desired response.

B. Restriction of the range of the sampled variables

The possible range of the values that a sampled variable can take is restricted to within a selected range expected to contribute to the desired result. To prevent biasing errors, the weight of the particle is changed accordingly. The effectiveness of this method is discussed in Appendix A. Generally, "common sense" knowledge of the phenomenon in question determines whether this method should be used. For instance, common sense suggests that the backscatter of radiation is limited to a thickness beyond which it is known from experimental evidence that a negligible contribution is made.

C. Mathematical method

This is a purely mathematical technique and usually has no direct physical basis. Among the examples of this method are specific cases of splitting, stratified sampling, Russian Roulette, and variable transform such as the exponential or linear transformation.

3.1.2 Statistical Fluctuations

Because of Monte Carlo's inherently statistical nature, the desired information has to be obtained from a statistical set of case histories.

The "expected" or "true mean" value $\langle \tau \rangle$ of a variable of interest τ can be estimated by Monte Carlo as the average $\bar{\tau}_N$ over N case histories of the statistical ensemble, that is:

$$\bar{\tau}_N = \frac{1}{N} \sum_{i=1}^{N} \tau_i \qquad (3.1.2\text{-}1)$$

This estimate, $\bar{\tau}_N$, is expected to approach $\langle\tau\rangle$ as the number of case histories N increases. To determine how close $\bar{\tau}_N$ is to $\langle\tau\rangle$ for a given value of N, the central limit theorem provides an estimate such that as N becomes very large, the probability that $|\bar{\tau}_N - \langle\tau\rangle|$ will be less than a small number ϵ is given by:

$$p(|\bar{\tau}_N - \langle\tau\rangle| < \epsilon) \approx \lim_{N\to\infty} \sqrt{\frac{2}{\pi}} \int_0^{\epsilon\sqrt{N}/\sigma} e^{-t^2/2}\, dt \qquad (3.1.2\text{-}2)$$

$$\text{where} \qquad \sigma^2 = \langle\tau^2\rangle - (\langle\tau\rangle)^2 \qquad (3.1.2\text{-}3)$$

and $\langle\tau^2\rangle$ is the expected value of:

$$\tau^2 = \lim_{N\to\infty} \frac{1}{N} \sum_{i=1}^{N} \tau_i^2 \qquad (3.1.2\text{-}4)$$

The probability that $|\bar{\tau}_N - \langle\tau\rangle|$ will be less than ϵ becomes unity for a fixed ϵ as $N\to\infty$, since $\int_0^\infty \exp(-t^2/2)\, dt = (\pi/2)^{1/2}$, provided that $\langle\tau\rangle$ and $\langle\tau^2\rangle$ exist.

Moreover, for a particular value of N, there is an ϵ such that $p(|\bar{\tau}_N - \langle\tau\rangle| < \epsilon)$ is, say, 0.99; if it is desired to reduce this value of ϵ in half, it is then necessary to process four times as many case histories so that $\epsilon\sqrt{N}$, and thus the value of the right hand side of Equation (3.1.2-2), remains constant. It is evident from Equation (3.1.2-3) that it is desired to have the variance of τ, namely σ^2, as small as possible if $\bar{\tau}_N$ is to be close to $\langle\tau\rangle$.

In practical applications, with a limited number of case histories, the variance of Equation (3.1.2-3) can only be

approximated by:

$$\sigma^2 = \frac{1}{(N-1)} \sum_{i=1}^{N} (\bar{\tau}_N - \tau_i)^2 \qquad (3.1.2\text{-}5)$$

The variance reduction methods mentioned in Section 3.1.1 are to be used to obtain a smaller σ.

3.2 Random Walks and Integral Equations

This section deals with transport of radiation and its simulation by transcription of the natural stochastic processes into a numerical Monte Carlo sampling procedures. The behavior of such simulation is a kind of random walk to integral equations.

3.2.1 Modular Outline

The modular steps needed to carry out a Monte Carlo simulation of radiation transport are:

A. Formulation of a description of the sources of radiation and their interpretation as probability density functions that can be sampled to specify initial values of the phase space coordinates in the simulation.

B. Formulation of the tracing of radiation path and the description of interactions between radiation and the medium, including sampling the distance traveled and pertinent probabilities to determine whether and what kind of radiation continues the process.

C. Repetition of module B, until either the radiation disappears or become insignificant.

D. During the iteration of module B, the events of interest are counted and recorded as results.

Steps A, B, and C, in effect, are rules for carrying out a random walk of a radiation particle that moves within a spatial-energy-direction phase space.

3.2.2 Descriptive Random Walk

To describe the random walk mathematically, one needs to:

1. Characterize the space on which the walk is defined.
2. Describe the probability density function (pdf) of the source, say $S(x)$.
3. Define the stochastic rule for moving from one point, say, x' to another, say, x (this will be a density function $T(x' \rightarrow x)$ for sampling a new point x when the previous point of the walk was x'). The probability density function T has to satisfy:

$$T(x' \rightarrow x) \geq 0$$

$$\int_x T(x' \rightarrow x)\, dx \leq 1$$

T is not normalized to permit the probability that the walk terminates at x' with probability $(1-\int T(x' \rightarrow x)\, dx)$.

4. Designate some variable of interest that is desired to be determined.

A general variable of interest would be the density of arrivals at x, namely $\Gamma(x)$. That is, summing over all steps of the random walk and averaging over all possible walks, the expected number of times that a point is sampled within a region $\mathfrak{R}$ is

$\int_R \Gamma(x)\, dx$.

The walk starts with an x, say x_0, sampled from S(x). Then if not absorbed, the neutron moves to x_1, sampled from $T(x_0 \rightarrow x_1)$. In general $T(x_{n-1} \rightarrow x_n)$ governs the n-th move. The arrival at x can occur either because it was sampled from S or because the neutron moved to x from an earlier point, say, x′. The total average density at x is the sum of these two:

$$\Gamma(x) = S(x) + \int T(x' \rightarrow x)\ \Gamma(x')\ dx' \qquad (3.2.2\text{-}1)$$

The integral term of the right-hand side of Equation (3.2.2-1) is the average density of arrival at x from the next earlier arrival, where $\Gamma(x')dx'$ is the chance that there was an arrival in dx′, and $T(x' \rightarrow x)$ is the probability that this arrival was followed by a move to x. One integrates over x′ to include all possible positions of the previous move. This equation describes the average behavior of the random walk.

$T(x' \rightarrow x)$ can be factored into:

$$T(x' \rightarrow x) \equiv (1-\Psi(x'))\ \Xi(x')\ \Upsilon(x', x) \qquad (3.2.2\text{-}2)$$

with $\Psi(x')$ ≡ capture probability at x′

$\Xi(x')$ is a normalization factor defined by

$$\Xi(x') = \frac{\int T(x', x)\, dx}{[1-\Psi(x')]} \qquad (3.2.2\text{-}3)$$

and $\Upsilon(x', x)$ is a normalized collision kernel given by

$$\Upsilon(x',x) = \frac{T(x',x)}{\int T(x'',x)\ dx''} \qquad (3.2.2\text{-}4)$$

The integral in Equation (3.2.2-1) can be solved using a Neumann expansion as:

$$\Gamma(x) = \sum_{n=0}^{\infty} \int dx_0 \int dx_1 .. \int dx_{n-1}\ S(x_0) T(x_0,x_1) .. T(x_{n-1},x)) \qquad (3.2.2\text{-}5)$$

and a functional $G = \int g(x)\Gamma(x)\ dx$ can be expressed as:

$$G = \sum_{n=0}^{\infty} \int dx_0 .. \int dx_n S(x_0)[1-\Psi(x_0)]\Upsilon(x_0,x_1)[1-\Psi(x_{n-1})]$$
$$\Upsilon(x_{n-1},x_n)\Psi(x_n)\omega(x_0..x_n) \qquad (3.2.2\text{-}6)$$

where

$$\omega(x_0..x_n) \equiv \frac{g(x_n)}{\Psi(x_n)}\ \Xi(x_0)..\Xi(x_{n-1})$$

These random walk sampling steps are used to evaluate the functional G as:

(1) sampling $S(x_0)$ for the initial coordinates x of a particle history.

(2) sampling $\Psi(x_{n-1})$ for termination at the n-th collision.

(3) sampling $T(x_{n-1},x_n)$ for the next collision point, given that the chain continues.

$\omega(x_0..x_n)$ is the "score" for such a history in the Monte Carlo calculation of G. Thus, G is the expectation value of the score, where the expectation implies averaging over all stochastic events that underline the random walk. Therefore, G can be estimated by

sampling a number of histories, computing ω for each history, and averaging these scores as:

$$G \cong \frac{1}{N} \sum_{i} \omega(x_0^i .. x_n^i) \qquad (3.2.2\text{-}7)$$

where $x^i_0,..,\ x^i_n$ are sampled from distributions given by $S(x_0)$, $T(x_{n-1},x_n)$, and n is determined by $\Psi(x_n)$.

In a sense, since the outcome is a series of points x_0, x_1, x_2..., the random walk can be regarded as a device for sampling the function Γ that is the solution of Equation (3.2.2-5). The correctness of the sampling is true asymptotically.

3.2.3 Boltzmann Transport Equation

Although particle transport by the Monte Carlo method can be performed without even referring to the transport equation, the following discussion is thought to give an insight into the simulation.

The time-independent integral transport equation for the neutron angular flux can be written (Bell and Glasstone, 1982) as:

$$\Phi(\mathbf{r},E,\hat{\Omega}) = \int_0^\infty e^{-\alpha(\mathbf{r},R,E,\hat{\Omega})}\ q(\mathbf{r},E,\hat{\Omega})\ dR \qquad (3.2.3\text{-}1)$$

where $\exp(-\alpha(\mathbf{r},R,E,\Omega))$ is the attenuation factor by which the flux is reduced in going through distance R to reach point $\mathbf{r}$, α is the optical thickness which is a measure of the effective absorption between points $\mathbf{r}$ and $\mathbf{r}'$ (separated by distance R), and $q(\mathbf{r},E,\Omega)$ is the total rate at which neutrons appear at $(\mathbf{r},E,\Omega)$ as a result of

both collisions and the independent (extraneous) source $S(\mathbf{r},E,\Omega)$, that is:

$$q(\mathbf{r},E,\hat{\Omega}) = \int\int \Sigma_s(\mathbf{r}',E'\rightarrow E,\hat{\Omega}'\rightarrow\hat{\Omega}) \Phi(\mathbf{r}',E',\hat{\Omega}')\,dE'd\hat{\Omega}' + S(\mathbf{r},E,\hat{\Omega}) \qquad (3.2.3\text{-}2)$$

where $\Sigma_s(\mathbf{r}',E'\rightarrow E,\Omega'\rightarrow\Omega)$ is the double differential scattering cross section at $\mathbf{r}'$ that characterizes scattering from an incident energy E' and direction Ω' to a final energy E in dE and direction Ω within the infinitesimal solid angle $d\Omega$. Therefore, the expected angular neutron collision density rate at which neutrons suffer collisions in $d\mathbf{r}$ about point $\mathbf{r}$, of neutrons of energies E between E and E+dE, moving in direction Ω in a differential solid angle $d\Omega$ is given by:

$$f(\mathbf{r},E,\hat{\Omega})\,d\mathbf{r}dEd\hat{\Omega} = \Sigma_t(\mathbf{r},E)\Phi(\mathbf{r},E,\hat{\Omega})\;\; d\mathbf{r}dEd\hat{\Omega} \qquad (3.2.3\text{-}3)$$

where $S(\mathbf{r},E,\Omega)\;d\mathbf{r}\;dE\;d\Omega$ is the rate of source neutrons appearing in $d\mathbf{r}$ about $\mathbf{r}$, dE about E, and $d\Omega$ about Ω. Substituting Equations (3.2.3-2) and (3.2.3-3) into Equation (3.2.3-1) yields the time-independent integral transport equation for the collision density rate as:

$$f(\mathbf{r},E,\hat{\Omega}) = \int_0^{\infty} d\mathbf{R}\;\Sigma_t(\mathbf{r},E)\;e^{-\alpha(\mathbf{r},\mathbf{R},E,\hat{\Omega})}\Big[\int dE'\int d\hat{\Omega}'\;\frac{\Sigma_s(\mathbf{r}',E'\rightarrow E,\hat{\Omega}'\rightarrow\hat{\Omega})}{\Sigma_t(\mathbf{r}',E')} f(\mathbf{r},E',\hat{\Omega}') + S(\mathbf{r},E,\hat{\Omega})\Big] \qquad (3.2.3\text{-}4)$$

This equation can be rewritten in a form similar to Equation (3.2.2-1) with:

x as $(\mathbf{r},E,\Omega)$, the particle phase space coordinates,

S(x) as the first-flight collision rate density due to the source,

T(x'→x) as the next-flight collision rate density at x due to collision at x', and

Γ(x) as the particle collision rate density.

The functional of Equation (3.2.2-6) is the detector photopeak response for capture gamma rays, given by:

$$G = \int d\mathbf{r} \int_0^\infty dE \int_{4\pi} d\hat{\Omega}\ P_{score}\ f(\mathbf{r},E,\hat{\Omega}) \qquad (3.2.3\text{-}5)$$

where P_{score}, discussed in Section 5.5, is the probability that an interaction within the capture gamma ray source region (the integration $\int d\mathbf{r}$ is carried out over the core sample volume) will score favorably under the detector full energy photopeak.

The steps of the random walk sampling are applied to obtain an estimate of G.

The sampling scheme can be interpreted physically as first sampling the initial particle coordinates $(\mathbf{r}_0,E_0,\Omega_0)$ by sampling the source $S(\mathbf{r},E,\Omega)$. Then the distance to the first collision R is determined by sampling:

$$\Sigma_t(\mathbf{r}_0,E_0)\ e^{-\alpha(\mathbf{r}_0,R,E_0,\hat{\Omega}_0)}$$

The sampled distance R along with the $(\mathbf{r}_0,\Omega_0)$ values are used to determine the location of this collision as:

$$r = r_0 + R\hat{\Omega}_0$$

One could sample from the capture probability:

$$\Psi(r_0, E) \equiv \frac{\Sigma_a(r_0, E)}{\Sigma_t(r_0, E)}$$

to see whether the particle is captured in the collision so that the history should be terminated. In practice, it is very inefficient to terminate histories when a capture event is sampled. Alternatively, the particle weight can be reduced or the score increased by the non-capture probability:

$$[1 - \Psi(x_1)] \equiv \frac{\Sigma_s(r_1, E_0)}{\Sigma_t(r_1, E_0)}$$

That is, all particles are forced to scatter at r_1. Next a new particle energy E_1 and flight direction Ω_1, are sampled from the scattering distributions. The energy is sampled from:

$$\frac{1}{4\pi\Sigma_s(r_1, E_0)} \int d\hat{\Omega}\ \Sigma_s(E_0 \rightarrow E_1, \hat{\Omega}_0 \rightarrow \hat{\Omega}_1)$$

while the flight direction Ω_1 is sampled from

$$\frac{\Sigma_s(E_0 \rightarrow E_1, \hat{\Omega}_0 \rightarrow \hat{\Omega}_1)}{\int d\hat{\Omega}\ \Sigma_s(E_0 \rightarrow E_1, \hat{\Omega}_0 \rightarrow \hat{\Omega}_1)}$$

This random walk procedure is applied to successive collision events until the particle history is terminated (see Section 5.6) because the particle's weight has been reduced below some cutoff value.

4. DESCRIPTION OF THE SEAFLOOR SEDIMENT CORE MONITORING SYSTEM

In this chapter, a detailed description is presented of the proposed and modeled monitoring system geometry and composition, with emphasis on construction materials, compatibility, and suitability in this work. This design is intended for a prototype for exploratory use.

4.1 General Configuration

The monitoring system is designed to analyze a cylindrical vibracore sample from the seafloor sediment by the NCPGA technique. The rapidity of this technique makes it feasible to pass an intact (full length) core through an assembly that contains the Cf-252 neutron source surrounded by water (moderator) to slow down the neutron energies to be more effective in inducing (n,γ) reactions within the core. The characteristic gamma rays, resulting from neutron capture interactions, are detected and recorded by a Ge detector and a multichannel analyzer spectrometer. The passing of the core through the monitoring system is done in pause and count steps. The gamma ray spectra are expected to be complex but contain distinguishable peaks. In this work, it is desired to simulate this monitoring system and to predict the functional dependence of the characteristic (photopeak) energy peaks on the elemental concentrations within the core sample.

Such a monitoring system, incorporated in a seagoing survey vessel and capable of analyzing seafloor sediments while the vessel

is underway, can be used to give guidance to the ultimate economic value of seafloor sediment deposits.

The basic geometrical configuration, shown in Figure 4.1-1, consists of a large cylindrical container (100 cm long and 100 cm in diameter) that houses the cylindrical vibracore sample of 7 cm diameter and of full intact length of the extracted vibracore, the Cf-252 source, and the detector assembly inside tubular constructions that protrude inside the container. The internal space is filled with a moderating material. A hydrogeneous moderator may not be optimum, since at distances further than a few centimeters from the source, neutron absorption by hydrogen becomes significant (Greenwood, 1978). A relatively pure thermal neutron flux may be obtained in moderator materials with a diffusion length greater than the slowing down length. Heavy water is a prime choice; however, since it is quite expensive, graphite or pure water may be an alternative.

The exterior dimensions of the container are mainly determined by the radiation dose limits to personnel during the routine handling operation, the most hazardous being during the transfer of the neutron source between its storage container and its operational location.

The sample tube extends along the entire length of the container and its axis could be located anywhere within the container. The only restriction is that it is co-linear with the major axis of the cylindrical container; this provision enables one to run the computer program with different relative locations

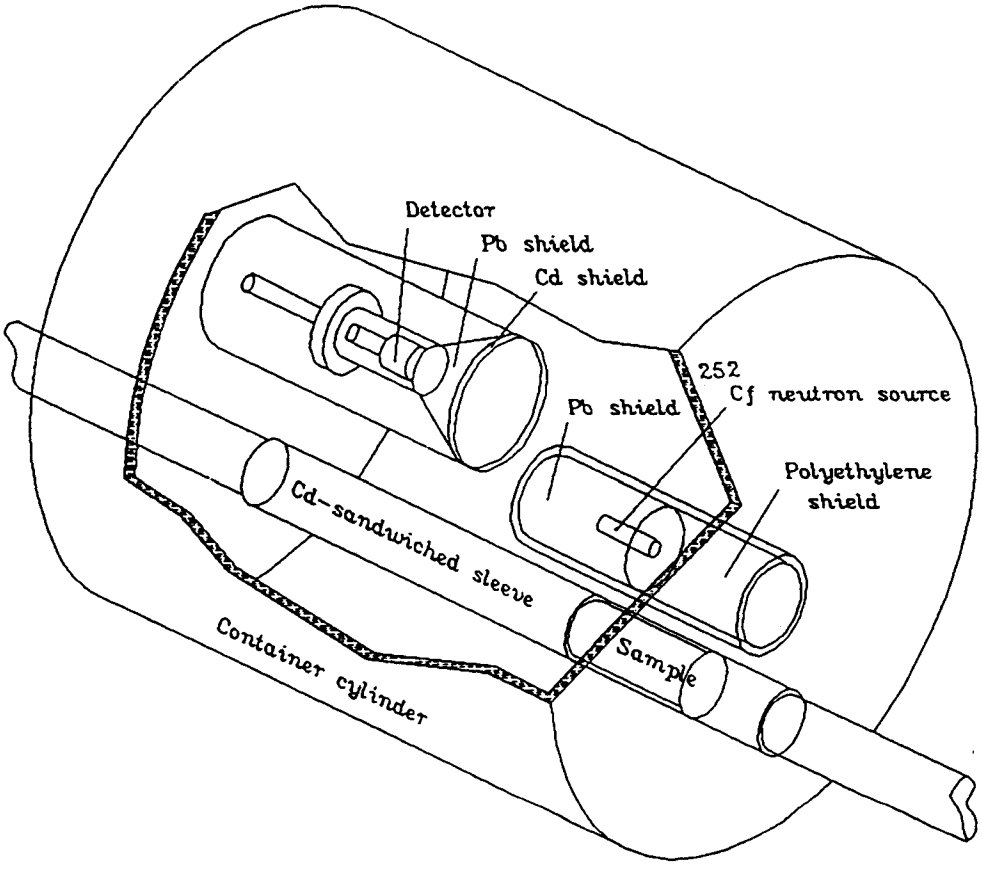

Figure 4.1-1 The proposed monitoring system showing internal configuration.

between the three tubes to examine the most effective positioning of the sample, source, and detector. The tube is accessible from the outside to accommodate a cylindrical core sample, which is usually encased in a lucite casing. The core sample is longer than the container cylinder and can be maneuvered manually or mechanically to be passed through the sample tube (it might be required, for good counting statistics to move the core sample in discrete intervals and pause to accumulate the required counts in between moves). The sample tube is lined on the inside with two sleeves in the form of an annular sandwich that is filled with a thin annular effective neutron absorber. The sleeves can be moved along the internal length of the sample relative to each other to form a variable length window that defines a cylindrical section of the core sample to be effectively exposed to the neutron flux. Thus, more information about the distribution of elements along the vibracore sample length can be gained by consecutively monitoring increments of the core. Marine mineral deposits generally occur as thin layers widely spaced in the seabed sediments, since they are often formed as a result of deposition processes.

The source tube (21 cm long and 6 cm diameter) extends partially inside the container cylinder; its inner end is closed and sealed to prevent water leakage into the internals. The tube is accessible from the outside of the container. The Cf-252 neutron source (encapsulated) is placed within a machined well along the axis of a cylindrical mass of lead shield. This shield helps reduce the background gamma radiations directly from the source. This

neutron source and its encapsulation contain details that are not significant in this work. The capsule is modeled to be represented by a stainless steel 316 solid capsule of 5 cm length and 0.5 cm radius with a spherical Cf-252 source, of 0.25 cm radius, at its centerline located at 1 cm from the end. Figure 4.1-2 shows an actual capsule along with the approximated model. The rest of the internal of the tube is occupied by a cylindrical bulk of shielding and moderating material (polyethylene).

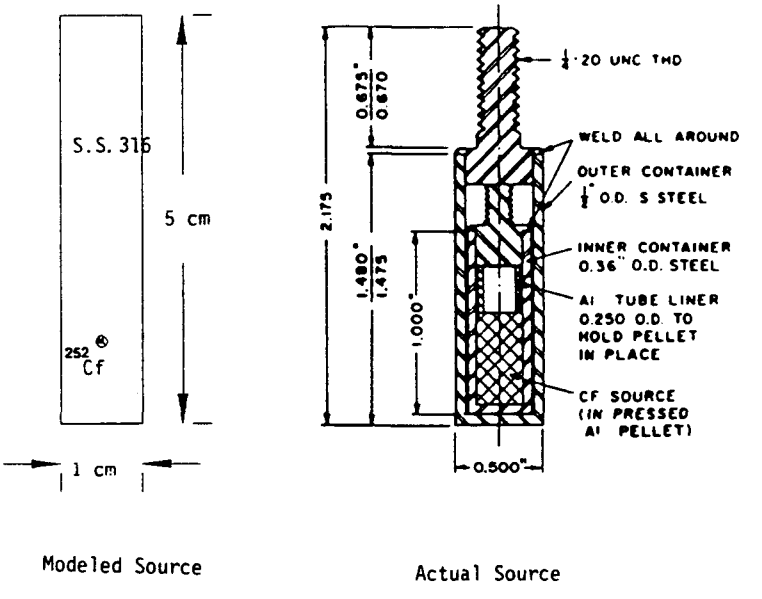

Figure 4.1-2 The industrial Cf-252 neutron source capsule and the adopted model.

The detector tube (74 cm long and of 14.5 cm diameter) extends partially along the inside of the container cylinder and is

positioned to be on the opposite end of the container from the source tube. Similar to the source tube, it is closed and sealed at the inner end and is accessible from outside the container. The innermost end of the tube contains a thin wafer of a neutron absorber (Cd, 0.3 cm thick) to reduce the intensity of gamma rays induced by neutron reactions in the detector housing. Since it is believed that the neutrons are well thermalized at this location, cadmium was used to accomplish this task. The radius of the wafer is the same as the inner radius of the tube. Next to the Cd wafer is a conical cylindrical shield of lead, intended to shield against the neutron capture gamma rays in the Cd wafer to prevent their contribution to the background and interference in the detector, and at the same time, to permit capture gamma rays coming from the core sample to arrive unshielded. The smaller radius of the conical cylindrical Pb shield is equal to the radius of the detector casing which is located next to it. The aluminum encased detector and its electronics are represented and modeled as shown in Figure 4.1-3. The detector extends inside the tube at the end of a copper cold finger. The annular space in between the conical cylindrical Pb shield, the detector and the inner surface of the detector tube is occupied by polyethylene to center the internals along the major axis of the tube.

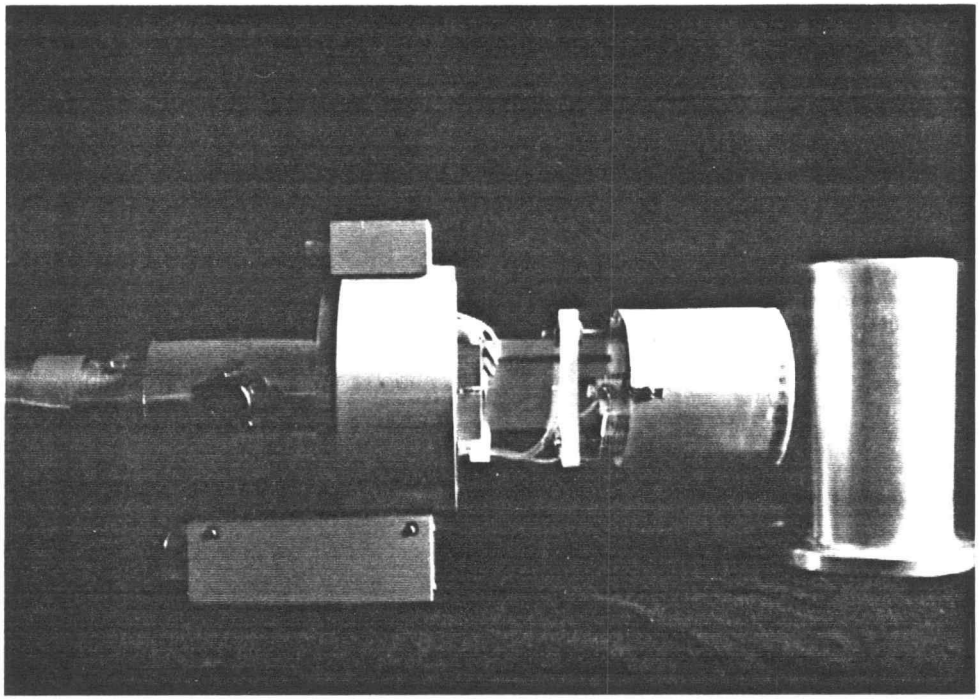

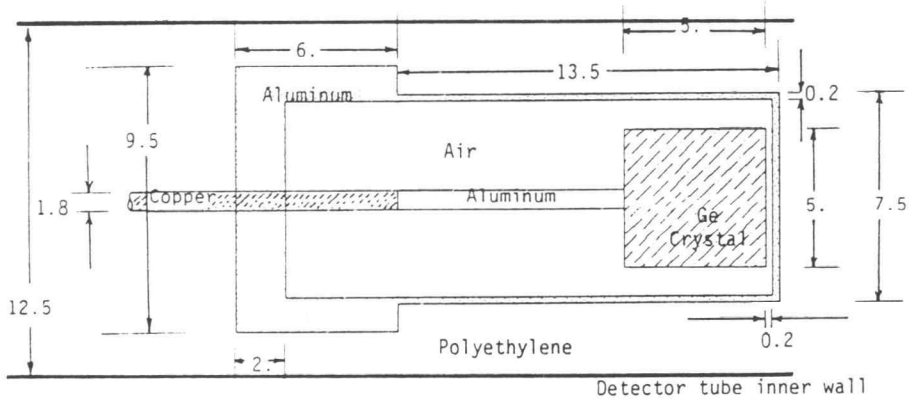

All dimensions are in cm

Figure 4.1-3 The detector proper and its approximation as modeled in this work.

4.2 Selection of Materials

Structural materials, i.e., the encapsulation, container, moderating, shielding materials, etc., are potential capture gamma ray sources which can cause a spectral interference that degrades the signal to background ratio. Thus, materials have to be chosen to minimize this interference, while considering nuclear properties, which affect the neutron economy, and mechanical fabrication constraints. For instance, there exists an excited state of oxygen at 6.14 MeV produced by inelastic scattering. The full, single, and double escape peaks due to inelastic scattering in oxygen almost coincide with three of the chromium capture peaks at 6.14, 5.62, and 5.12 MeV, respectively.

The criterion of "interference parameter" S_T, as applied by Senftle *et al.*, (1971) was used to select low-background materials. S_T is defined to be the sum of discrete energy sensitivity indices S_E over the energy range from 3 to 10 MeV as defined by Duffy *et al.*, (1970) and is proportional to the number of gamma rays per unit incident neutron flux per unit mass. Therefore, the interference, when defined as above for construction materials of any system, is a function of the total amount of the individual materials present in the system. Thus,

$$S_T = \sum_{3}^{10\ \mathrm{MeV}} S_E = \sum_{3}^{10\ \mathrm{MeV}} I_E \frac{\sigma}{A} \qquad (4.2\text{-}1)$$

where S_E = sensitivity index for energy E

I_E = the gamma photon yield (photons/100 n captured)

σ = the elemental thermal capture cross section (barns), and

A = the atomic weight of the element (g/mole)

Table 4.2-1 lists interference parameter values for some elements of interest in the proposed monitoring system.

Small S_T values in an element without prominent peaks indicates a minimal interference in the capture gamma ray spectrum. A sensitivity index of 0.01 and $I_E > 1$ is considered a useful rule of thumb limit (Duffy *et al.*, 1970) to assess the usefulness of analytical analysis below which the interference contribution may be overlooked.

Element	Interference parameter S_T	Sensitivity index $S_{E_{max}}$
C	0.028	0.019
Mg	0.291	0.106
Al	0.633	0.175
Mo	0.724	0.096
Ge	1.50	0.069
Na	2.62	0.596
Fe	4.66	2.31
Cr	5.76	1.44
Cu	5.96	1.72
Ni	9.02	3.25
Ti	16.54	6.87
Mn	23.4	2.91
Cl	78.3	14.8
Cd	837.3	75.0

Table 4.2-1 The interference parameter along with the maximum sensitivity index S_E in the range 3-10 MeV for some elements of interest.

The californium encapsulation can be custom fabricated to meet any constraints, although these constraints must be balanced with safety and service requirements. Iron and chromium have a large number of capture gamma rays with sensitivity indices above 0.01, whereas zirconium has only one gamma line with an $S_E > 0.01$. Therefore zirconium alloys offer low interference and at the same time have acceptable resistance to chemical and mechanical damage.

In the case that the detector material and the associated hardware are exposed to a significant neutron flux, the capture gamma rays resulting from the detector crystal and the hardware could be significant and one should endeavor to minimize such interference either by reducing the neutron flux in the proximity of the detector or through selective choice of the materials, or both. The detector cold-finger heat conductor to the liquid-nitrogen cryostat in a Ge detector is generally fabricated from copper for its high thermal conductivity; unfortunately copper has moderately high interference parameters due to a significant number of very prominent peaks. A trade-off between thermal and interference properties has to be considered, especially if copper is one of the elements whose response is of interest.

Calculations by Nichols (1968) indicated that polyethylene moderators give the best peak thermal neutron flux up to about 10 centimeters from a point Cf-252 source. The 4.95 MeV capture gamma ray from the $^{12}C(n,\gamma)^{13}C$ reaction may cause interference for some experiments. The 2.223 MeV capture gamma ray of hydrogen, when a hydrogenous moderator is used, is considered below the energy range

of interest and can usually be ignored, although these gamma rays can cause significant personnel exposure rates outside the moderator-shield assembly and thus should be considered from that point of view. In water, the aforementioned inelastic scattering from oxygen may cause undesired interference. Small amounts of zirconium hydride in the immediate vicinity of the source could lead to a significant increase in the thermal neutron flux, but excessive amounts of zirconium might also raise the capture gamma ray background below 6 MeV to undesirable levels.

The thermal neutron shield in the vicinity of the detector and its surroundings (e.g., electronic components and copper wires) could be ^{6}Li or cadmium. The latter has the disadvantage of excessive capture gamma rays, but can be shielded by appropriate geometry. For the former shield, one has to consider the $^{6}Li(n,\alpha)^{3}H$ exothermic reaction.

In general, the best materials to be used will be dictated, to a certain extent, by the elements one wishes to measure and the neutron flux in the proximity of the material in question during a given experiment.

4.3 Choice of the Detector

The energy spectrum of capture gamma rays generated by the sample consist of a series of isolated narrow lines whose energies are accurately known. The derivation of elemental concentrations is based on the absolute intensities of these peaks. In fact, the identity of a particular gamma ray in a spectrum is determined to

result from a specific capturing element when it can be shown that the intensity per unit mass of the capturing element is constant or that the ratio of intensities of two peaks is constant for several samples of the elements obtained from different sources.

In the capture gamma ray spectrum, certain gamma ray interactions in the detector form a background continuum under the isolated peaks (lines). The lines become closely spaced due to the number of contributing elements; the single and double escape peaks from high energy gamma rays further crowd the spectrum. For instance, the primary capture lines from Ti are 6.7597 MeV and 6.418 MeV, which are difficult to separate from interference peaks when there is a small Ti concentration present. The single escape peak of Fe (7.2789 MeV) interferes with the Ti 6.7597 MeV peak, and the double escape peak of the Cl 7.790 MeV capture peak further complicates the interference. Also, the double escape peak of the Cl 7.4138 MeV peak interferes with the Ti 6.418 MeV peak. Table 4.3-1 lists the prominent capture gamma ray energies from all the materials used in the monitoring system in order of increasing energy to illustrate the energy interference effects.

Because of this complex spectra of capture gamma rays, a detector with high energy resolution is essential, thereby necessitating the use of a solid-state detector. High resolution germanium detectors have the drawback of having relatively low efficiency for high energy gamma rays, such as encountered in neutron capture where the gamma rays released following the capture process have energies up to 10 MeV. In addition, these detectors

Branching Ratio (γ/100 capture)	Energy (MeV)	Responsible Element
82.0	2.1844	O
100.0	2.223	H
5.55	2.4149	Na
14.78	2.5176	Na
10.15	2.8627	Na
39.0	3.028	Ge
8.35	3.0981	Na
18.0	3.271	O
14.95	3.588	Na
32.10	3.6889	C
5.38	3.8785	Na
18.63	3.982	Na
14.94	4.4189	Ca
5.23	4.8824	Ti
67.64	4.9452	C
5.17	5.6167	Na
5.50	5.7152	Cl
9.02	5.9203	Fe
9.0	6.0184	Fe
20.0	6.1108	Cl
22.18	6.3954	Na
30.13	6.4183	Ti
38.89	6.4199	Ca
8.01	6.6195	Cl
5.04	6.7364	Pb
24.17	6.7597	Ti
10.79	6.837	Ni
5.33	7.2787	Fe
8.09	7.3062	Cu
94.06	7.3677	Pb
10.42	7.4138	Cl
28.51	7.6311	Fe
15.71	7.6366	Cu
24.13	7.6454	Fe
8.55	7.7901	Cl
8.19	7.8189	Ni
30.82	7.9145	Cu
16.98	8.5334	Ni
37.74	8.9988	Ni

Thermal neutron capture cross sections(barns):
H:0.332, C:3.37×10^{-3}, O:2.7×10^{-4}, Na:0.4,
Cl:33.2, Ca:0.43, Ti:6.1, Fe:2.55, Ni:4.43,
Cu:3.79, Ge:2.3, Mo:2.65, Cd:2450.,and Pb:0.17

Table 4.3-1 Major capture gamma rays from neutron captures in various elements of the monitoring system.

are expensive and unable to operate for a long period in an intense fast neutron flux. Stelson *et al.* (1972) showed that ~10^8 fast neutron/cm^2 will damage a coaxial Ge(Li) detector, which suffers a loss of resolution when used at high counting rates, with a progressive loss of resolution as a result of radiation damage. Reliable large radiation-hardened Ge detectors, such as the n-type hyperpure germanium detectors that are not damaged by recycling to room temperature and have relatively low sensitivities to neutron damage, are now available. Such a detector with a carefully designed shield that maximizes the attenuation of the fast neutrons with only a small impact on the neutron capture gamma rays from the sample is an excellent choice.

4.4 Core Sample

The geometry of the core is adopted to be a standard offshore drilled core, although a cored sample limits the potential of the nuclear technique. A larger (more representative) volume can be investigated in an in-situ borehole configuration. The composition of a typical core is simulated based on reported elemental analysis (Peterson and Binney, 1988) of Oregon continental shelf samples, along with some assumptions that are thought to be reasonable.

The core matrix is assumed to be SiO_2 and salt water (typical seawater with 35 ppt NaCl). The silicon dioxide density is taken to be that of shale (sandstone) rocks (2.65 g/cm^3). The salt water density is 1.02072 g/cm^3. The core is considered to be 90 $^w/_o$ SiO_2 and 10 $^w/_o$ salt water, which yields a bulk density of 2.488 g/cm^3.

The core sample is assumed to be neutronically homogeneous, i.e., any heterogeneity in the distribution of elements within the sample is within the range traveled by a neutron.

A typical composition of shale is given in Table 4.4-1.

Element	Weight percent
H	0.28
C	0.72
O	49.9
Na*	1.19
Mg*	1.6
Al*	8.79
Si	27.53
Ca*	1.52
Ti*	0.47
Mn*	0.07
Fe*	4.82

Table 4.4-1 Typical composition of shale

The relative abundance of Mg, Ti, Cr, Mn, Fe, Na, Al, and Ca in Oregon continental shelf sample is estimated in Table 4.4-2.

Element	Relative abundance ▪
Na	0.0053
Mg	0.1239
Al	0.0354
Ca	0.0531
Ti	0.1947
Cr	0.0425
Mn	0.0142
Fe	0.5310

(▪) indicates a normalized group

Table 4.4-2 Estimated relative abundance of selected elements in Oregon continental shelf samples.

The elements in Table 4.4-2 and their relative abundance are used to replace the elements that are marked by an asterisk in Table 4.4-1. The Na, Cl, H, and O in salt water are added to Table 4.4-1 and normalized to yield an estimated core sample composition as shown in Table 4.4-3.

Element	Weight percent
H	1.0825
C	0.6684
O	52.8541
Na	0.9503
Mg**	2.1292
Al	0.6083
Si	25.5591
Cl**	1.7903
Ca	0.9125
Ti**	3.3458
Cr**	0.7304
Mn**	0.2440
Fe**	9.1251

** These elements were changed sequentially to predict the photopeak responses as a function of elemental concentrations.

Table 4.4-3 Estimated elemental composition of the (reference) core sample.

The elements, marked with double asterisks in Table 4.4-3 are those whose prominent capture gamma rays are estimated at the detector. The energies and branching ratios (yields) are given in Table 4.4-4 based on thermal neutron captures (Lone *et al.*, 1981).

Element	Capture γ-ray Energy (keV)	Branching Ratio (γ/100 neutron captures)
Mg	585.20	25.55
	1808.90	29.97
	2828.10	42.51
	3916.70	48.62
Cl	5715.26	5.50
	6110.88	20.00
	6619.53	8.01
	7413.80	10.42
	7790.16	8.55
Ti	341.70	26.27
	1381.48	69.08
	6418.35	30.13
	6759.78	24.17
Cr	835.10	26.86
	7939.30	26.97
Mn	7057.81	11.06
	7243.79	12.13
Fe	352.18	11.70
	6018.48	9.00
	7631.13	28.51
	7645.45	24.13

Table 4.4-4 Selected capture γ-rays emitted from the elements of interest along with their branching ratios.

5. OVERVIEW OF THE NEUTRON TRANSPORT SIMULATION

In this chapter, the procedures of the Monte Carlo simulation are discussed, along with the nuclear reactions that have been modeled in various materials and the justifying arguments, where applicable, to include or exclude some features or reactions. The Monte Carlo simulation involves several distinctive phases, which are discussed below.

5.1 Sampling the Neutron Source Parameters

The neutron state, which is defined exclusively in this work via its position, direction, and energy, is required to be known at all times. For tracking convenience the cartesian coordinates (x,y,z) are chosen with a specified coordinate origin as shown in Figure 5.1. The direction parameters are specified through the polar angle θ and the azimuthal angle ϕ in spherical coordinates. The associated cartesian coordinates for the normalized direction cosines are given by:

$$\Omega_x = \sin\theta \cos\phi$$

$$\Omega_y = \sin\theta \sin\phi$$

$$\Omega_z = \cos\theta \qquad (5.1\text{-}1)$$

Finally, the energy variable is represented by an energy parameter E. Thus, the neutron state is defined by a seven dimensional vector $(x,y,z,\Omega_X,\Omega_Y,\Omega_Z,E)$. For tracking and scoring purposes the neutron also has some other parameters associated with it. They are the

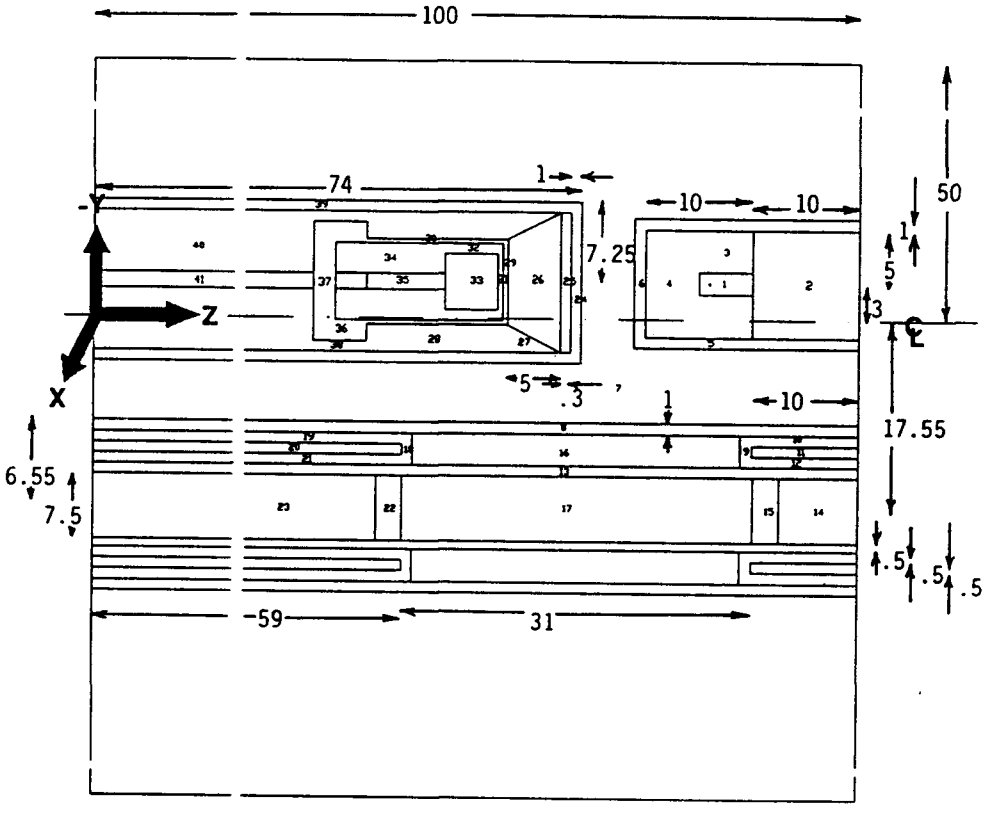

Dimensions in larger prints are in cm

Figure 5.1 Schematic diagram of the various cells (cell numbers in small prints) and the master cartesian coordinate origin. Cell 1 is the neutron source, cell 33 is the Ge detector, cell 17 is the effective core sample volume, cells 14,15,22, and 23 are sections of the core sample considered to assess the effectiveness of the Cd sleeves (cells 11 and 20)

absolute weight and a geometrical index which tells which geometrical region the neutron is in.

For a point source, the position parameters are initialized at

$$x_0 = x_{\text{point source}}$$
$$y_0 = y_{\text{point source}}$$
$$z_0 = z_{\text{point source}} \qquad (5.1\text{-}2)$$

The direction parameters are sampled from an isotropic distribution of polar and azimuthal angles in the laboratory system. The isotropic distribution of Equation (2.1.5-15) is repeated here for convenience:

$$p(\theta,\phi)\ d\theta\ d\phi = \frac{1}{4\pi} \sin\theta\ d\theta\ d\phi$$

and since θ and ϕ are uncorrelated, is sampled as

$$p'(\theta)d\theta = \frac{1}{2} \sin\theta\ d\theta$$
$$\theta = \cos^{-1}\ (2\xi - 1) \qquad (5.1\text{-}3)$$

When the random number $\xi\in(0,1)$, then $\theta\in(0,\pi)$.

$$\hat{p}(\phi)\ d\phi = \frac{1}{2\pi}\ d\phi$$
$$\phi = 2\pi\xi \qquad (5.1\text{-}4)$$

When $\xi\in(0,1)$, then $\phi\in(0,2\pi)$.

The energy parameter of the emitted neutron from Cf-252 source is governed by the probability density function (pdf) of Equation (2.1.1-1) that can be sampled through the use of three random numbers ξ_1, ξ_2, and ξ_3 on (0,1) (Carter and Cashwell, 1975) as

$$E = 1.424\ [-\ln\xi_1 - \ln\xi_2 \cos^2(\tfrac{\pi}{2}\xi_3)]\ \text{(MeV)} \qquad (5.1\text{-}5)$$

5.2 General 3-D Tracking

The neutron is followed through the cell geometry (in the case of a new history with a source neutron, the neutron is initially located within the source capsule). The tracking utilizes the essential feature that neutrons travel in a straight line between collisions.

In general, the parametric equations that describe a point (x_n,y_n,z_n) vector Ω in the direction $(\Omega_x, \Omega_y, \Omega_z)$ and starting from point (x_0,y_0,z_0) are given (see Appendix E) by:

$$\begin{aligned} x_n &= x_0 + D\ \Omega_x \\ y_n &= y_0 + D\ \Omega_y \\ z_n &= z_0 + D\ \Omega_z \end{aligned} \qquad (5.2\text{-}1)$$

where the distance traveled D is given by:

$$D = \sqrt{(x_n-x_0)^2 + (y_n-y_0)^2 + (z_n-z_0)^2} \qquad (5.2\text{-}2)$$

Tracking the neutron inside the cell consists of:

A. Evaluation of the microscopic cross sections, pertaining to the elements in the cell, at the neutron energy E. This is accomplished by interpolation from ENDF/B-V data.

B. Computation of the macroscopic cross sections, depending on the cell composition, and the total macroscopic cross section.

C. Computation of the distance to the cell boundary in the

direction of the neutron flight.

Repetitive geometrical patterns in the monitoring system permitted the system to be modeled by dividing it into a collection of 41 cells, as shown in Figure 5.1. All cells can be constructed from four basic geometries, namely solid circular cylinders, annular cylinders, circular right conical cylinders, and reversed conical cylinders inside the container cylinder with three internal tubular protrusions that contain the sample, the source, and the detector assemblies. The distance to the boundary for neutrons having an interaction within the geometry is determined as indicated below for the various geometries used.

5.2.1 Solid Circular Cylinder

First, the intersection points of the neutron direction of flight vector Ω with the infinite cylinder of radius R are determined by solving for the projection of the intersection in the x-y plane. The circular projection is described by the equation

$$(x - x_{CL})^2 + (y - y_{CL})^2 = R^2 \qquad (5.2.1\text{-}1)$$

Where (x_{CL},y_{CL}) are the coordinates of the projection of the geometry centerline on the x-y plane. The intersection points satisfy Equation (5.2.1-1), whose coordinates (x_n,y_n,z_n) are given by the parametric Equations (5.2-1) in terms of the coordinates of the neutron position inside the cylinder (x_o,y_o,z_o), the direction cosines of the neutron flight vector $(\Omega_x,\Omega_y,\Omega_z)$, and the distance d between the points (x_o,y_o,z_o) and (x_n,y_n,z_n). This is the distance

to the boundary.

Substituting Equations (5.2-1) into Equation (5.2.1-1) to eliminate x and y yields an expression that is quadratic in d and hence has two roots.

$$d^2(\Omega_x^2+\Omega_y^2)+2d[\Omega_x(x_0-x_{CL})+\Omega_y(y_0-y_{CL})]$$
$$+[x_0^2+y_0^2-2(x_0x_{CL}+y_0y_{CL})+x_{CL}^2+y_{CL}^2-R^2]=0 \qquad (5.2.1\text{-}2)$$

The discriminant to Equation (5.2.1-2), namely,

$$4[\Omega_x(x_0-x_{CL})+\Omega_y(y_0-y_{CL})]^2-4(\Omega_x^2+\Omega_y^2)$$
$$[x_0^2+y_0^2-2(x_0x_{CL}+y_0y_{CL})+x_{CL}^2+y_{CL}^2-R^2] \qquad (5.2.1\text{-}3)$$

determines the nature of the roots.

$$\text{If discriminant} \begin{cases} < 0; \text{ two imaginary roots exist (no intersection)} \\ = 0; \text{ two equal real roots exist} \\ > 0; \text{ two different real roots exist} \end{cases} \qquad (5.2.1\text{-}4)$$

Point (x_0,y_0,z_0) is within or on the boundaries of the geometry, although this is not a strictly true statement due to round-off errors in digital representations. As explained in Section 5.7, point (x_0,y_0,z_0) is always confined to be within the boundaries. Thus, Equation (5.2.1-2) always gives two real roots. The root in the desired direction Ω (denoted by d^*) is positive, and the other is negative, as shown in Figure 5.2.1.

To determine whether the direction vector penetrates the top,

bottom, or side wall of the finite cylinder before leaving the cylindrical surface, the z-coordinate of the intersection point:

$$z^* = z_0 + d^* \Omega_z \qquad (5.2.1\text{-}5)$$

is compared with the cylinder end z-coordinates. For $z^* > z_{top}$, the direction vector pierces the top of the cylinder and the desired distance to the boundary δ is:

$$\delta = \frac{(z_{top} - z_0)}{\Omega_z} \qquad (5.2.1\text{-}6)$$

If $z_{bottom} < z^* < z_{top}$, the direction of flight vector intersects the side wall and the desired distance to the boundary δ is given by:

$$\delta = d^* \qquad (5.2.1\text{-}7)$$

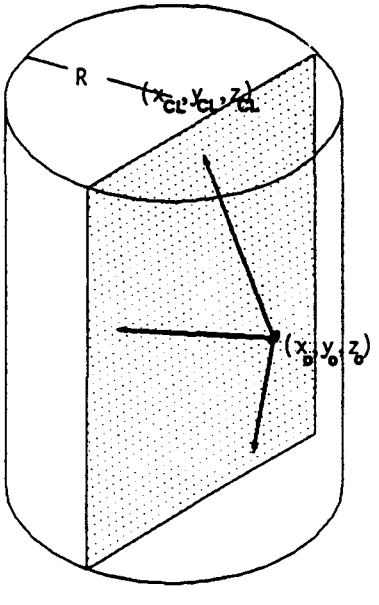

Figure 5.2.1 Tracking within a solid circular cylindrical geometry.

If $z^* < z_{bottom}$, the direction of flight vector pierces the bottom

of the cylinder and the desired distance is:

$$\delta = \frac{(z_{bottom} - z_0)}{\Omega_z} \qquad (5.2.1\text{-}8)$$

Knowing whether the direction vector penetrates the top, bottom, or side wall of the cylinder allows the neutron to enter the proper neighboring cell, should it escape its present cell.

5.2.2 Annular Cylinder

Again the procedure of Section 5.7 is practiced to ensure that the neutron is within the geometry. The desired distance to the boundary (see Figure 5.2.2) is determined by first evaluating

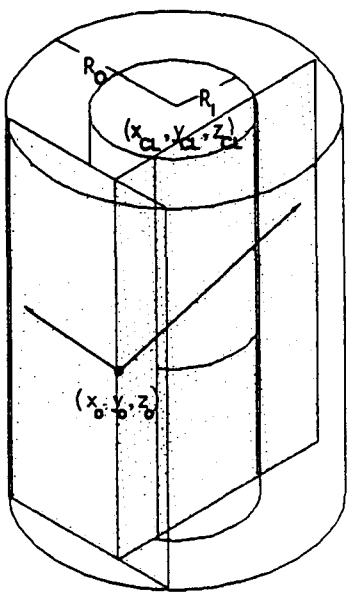

Figure 5.2.2 Tracking within an annular cylindrical geometry.

Equation (5.2.1-2) at the inner radius R_I; a negative or zero discriminant as given by Equation (5.2.1-3) indicates that the

flight direction does not intersect the inner surface or that it just barely intersects tangentially, respectively. In this case Equation (5.2.1-2) is re-evaluated at the outer radius R_0 and the geometry is effectively treated as the solid cylinder was treated in Section 5.2.1. On the other hand, when Equation (5.2.1-2) evaluated at the inner radius gives two real roots, (a positive root and a negative root possibility is excluded since the neutron is not within the inner circle), both roots being negative implies that the flight direction is directed away from the inner surface and the treatment for the solid cylinder at the outer radius can be used. Two positive roots indicate that the direction vector pierces through the inner surface and the desired root is the smaller of the two, say, d^*, which is then used in Equation (5.2.1-5) to determine the z-coordinate of the intersection point. The comparison with the z-coordinates of the cylinder ends as explained for the solid circular cylinder in Section 5.2.1 determines whether the direction vector penetrates the top, bottom, or the inner surface.

5.2.3 Right Circular Conical Cylinder

With the neutron position at (x_0,y_0,z_0) and its direction vector ensured to be within the geometry, the intersection of the vector Ω with the conical shape is determined by substituting the parametric equations given by Equation (5.2-1) into:

$$\sqrt{(x-\hat{x})^2 + (y-\hat{y})^2} - t(z-\hat{z}) = 0 \qquad (5.2.3\text{-}1)$$

where $(\hat{x},\hat{y},\hat{z})$ are the coordinates of the vertex of the cone with a

slope t (see Figure 5.2.3). An expression that is quadratic in d results:

$$d^2(\Omega_x^2+\Omega_y^2-t^2\Omega_z^2)+2d[\Omega_x(x_0-\hat{x})+\Omega_y(y_0-\hat{y})-t^2\Omega_z(z_0-\hat{z})]$$

$$+[x_0^2+y_0^2-2(x_0\hat{x}+y_0\hat{y})+\hat{x}^2+\hat{y}^2-t^2(z_0^2-2z_0\hat{z}+\hat{z}^2)]=0 \quad (5.2.3\text{-}2)$$

The two roots may be investigated through the discriminant similar to Equation (5.2.1-4), the discriminant being

$$4[\Omega_x(x_0-\hat{x})+\Omega_y(y_0-\hat{y})-t^2\Omega_z(z_0-\hat{z})]^2 - 4(\Omega_x^2+\Omega_y^2-t^2\Omega_z^2)$$

$$[x_0^2+y_0^2-2(x_0\hat{x}+y_0\hat{y})+\hat{x}^2+\hat{y}^2-t^2(z_0^2-2z_0\hat{z}+\hat{z}^2)] \quad (5.2.3\text{-}3)$$

Two real roots are expected because the point (x_0,y_0,z_0) is strictly within the geometry. If one denotes the smaller of the two roots as $d_{min}= \min(d_1,d_2)$ and the larger as $d_{max}= \max(d_1,d_2)$, Figure 5.2.3 shows that the two roots are either equal (both positive or both negative) or a positive root and a negative root.

Case I. Both roots are positive. This subcase includes the special case when both roots are equal. The root of smaller numerical value d_{min} is the desired root d^* and is used to evaluate the z-coordinate of the closest intersection point using Equation (5.2.1-5); this value of z^* is compared with the z-coordinate of the bottom end of the conical geometry (the end that is closer to the vertex). If $z_{min} \leq z_{bottom}$, then the vector Ω pierces through the the bottom

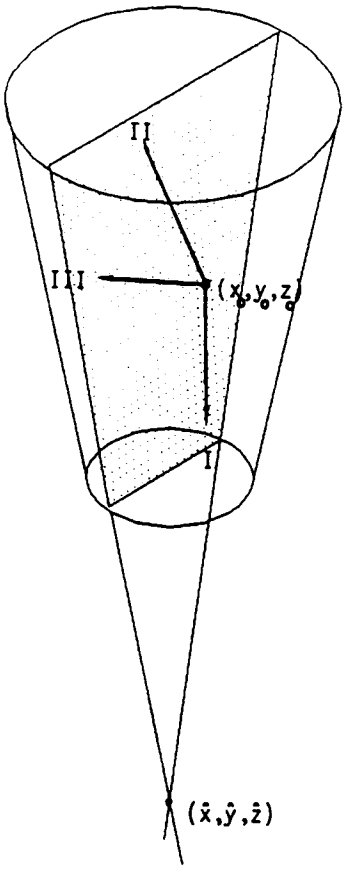

Figure 5.2.3 Tracking within a right circular solid conical geometry

surface and the desired distance δ is obtained from Equation (5.2.1-8). If $z_{min} > z_{bottom}$, then the vector Ω pierces through the side wall surface and the desired distance δ is determined as follows:

The x and y coordinates of the intersection point (x',y',z^*) which lies on the conical surface are determined from:

$$x' = \hat{x} + \sqrt{t^2(z_0-\hat{z})^2 - (y_0-\hat{y})^2}$$

$$y' = \hat{y} + \sqrt{t^2(z_0-\hat{z})^2 - (x_0-\hat{x})^2} \qquad (5.2.3\text{-}4)$$

The desired distance to the intersection is determined as:

$$\delta^* = \sqrt{(x'-x_0)^2 + (y'-y_0)^2 + (z'-z_{max})^2} \qquad (5.2.3\text{-}5)$$

Case II. Both roots are negative. This is conclusive that the vector Ω pierces through the top surface and the desired distance is obtained from Equation (5.2.1-6).

Case III. One positive and one negative root. The positive root is chosen as the desired root d^*, and the z coordinate of the intersection point is obtained from Equation (5.2.1-5); if $z_{bottom} < z^* < z_{top}$, then the vector Ω pierces through the side wall surface and the coordinates of the intersection point and the desired distance are obtained from Equations (5.2.3-4) and (5.2.3-5), respectively. If $z^* \leq z_{bottom}$, then the vector penetrates the bottom surface, and the desired distance is obtained from Equation (5.2.1-8). Otherwise, if $z^* \geq z_{top}$, then the vector Ω pierces through the top surface, and the desired distance is given by Equation (5.2.1-6).

5.2.4 Reversed Conical Cylinder

For a point (x_0,y_0,z_0) and a flight vector Ω located within a finite reversed conical cylinder of smaller radius R, height H, and geometrical center at (x_c,y_c,z_c), as shown in Figure 5.2.4, the distance to the closest boundary in the direction of flight is determined via a procedure analogous to the annular cylinder of Section 5.2.2. It is more convenient to examine first the possibility of intersection of the direction of the flight vector with the inner conical surface by solving Equation (5.2.3-2) for d.

The solution may either indicate no intersection, intersection in the negative (back track) direction of Ω (two negative roots), intersection in the direction of Ω (two positive roots), or intersection in both forward and backward directions of Ω (a positive and a negative root). Specific logical considerations require that the quadratic Equation (5.2.1-2) be re-evaluated at the outer cylindrical radius as follows:

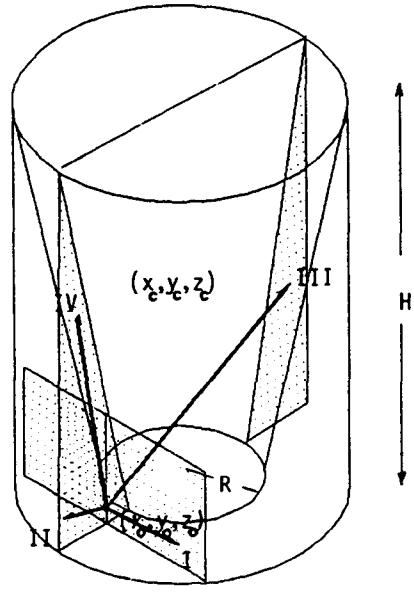

Figure 5.2.4 Tracking within a reversed conical cylindrical geometry.

Case I. If the discriminant of Equation (5.2.3-2) is negative, this is an indication of no intersection with the conical surface. Then the quadratic Equation (5.2.1-2) with R as the outer cylinder radius

is solved and should yield a positive and a negative root. The positive root is taken to be the desired root d^* and is used in Equation (5.2.1-5) to determine the z-coordinate of the point of intersection z*. A test is then made by comparing this z-coordinate with the z-coordinates at the top and bottom ends of the geometry in a procedure similar to the solid circular cylinder of Section 5.2.1. The direction of flight intersects the outer cylindrical surface if $z_{bottom} < z^* < z_{top}$ and the desired distance to the boundary δ is given by Equation (5.2.1-7). If the inequality is not satisfied, and $z^* < z_{bottom}$, the direction vector pierces the bottom surface of the geometry, and the desired distance to the boundary δ is computed by Equation (5.2.1-8). The possibility that $z^* > z_{top}$ is excluded logically for it violates the no intersection condition with the conical surface that led to the re-evaluation at the outer cylindrical surface. The parameters d_{min} and d_{max} are defined as the minimum and maximum, respectively, of the two real roots resulting from solving Equation (5.2.3-2).

Case II. If the larger of the two roots is negative, implying interaction in the negative direction of Ω, then the quadratic Equation (5.2.1-2) is solved at the outer cylinder surface, and subcase I is applicable.

Case III. If both roots are positive, the intersection is in the forward direction of Ω and the smaller of the two roots d_{min} is chosen to be the desired root d^* that determines the z-coordinate of the intersection point, using Equation (5.2.1-5). In a logic similar to the circular cylinder case of Section 5.2.1, if this

intersection point is located below the bottom end of the geometry, then the direction vector pierces through the bottom surface and the distance to the intersection is given by Equation (5.2.1-8). On the other hand, if the z-coordinate is greater than the z-coordinate of the bottom of the geometry, then the direction vector pierces through the inner conical surface and the desired distance is $\delta = d^*$. The intersection point z-coordinate is not possible to be greater than z_{top} when there are two positive roots, and therefore is excluded.

Case IV. For the subcase when one of the real roots is positive and the other is negative, the positive root d_{max} is chosen as the desired root d^*, and the z-coordinate of the point of intersection z^* is determined from Equation (5.2.1-5) and compared with the end coordinates as follows:

If $z_{bottom} < z^* < z_{top}$, then the direction vector pierces the inner conical surface and the desired distance to the intersection is $\delta = d^*$. If the inequality is not satisfied but $z^* > z_{top}$, then the quadratic equation of the outer cylindrical surface is solved, and subcase I is applicable. Otherwise if $z^* < z_{bottom}$, then the direction vector pierces the bottom surface, and the desired distance is given by Equation (5.2.1-8).

5.2.5 Container Cylindrical Tank

Given the neutron is located at a point (x_0,y_0,z_0) within the container tank, but not within any of the internally protruding tubes that contain the sample, source, or the detector. The neutron

is traveling in a path characterized by the vector $\Omega = \Omega_x \hat{i} + \Omega_y \hat{j} + \Omega_z \hat{k}$ where $(\Omega_x,\Omega_y,\Omega_z)$ are the normalized direction cosines. This path intersects an infinite cylinder of radius r whose major axis is located at (x_{CL},y_{CL}), if the point of closest approach (discussed in the next paragraph) (x_p,y_p) from the path of vector Ω to the point (x_{CL},y_{CL}) is within the radius of the cylinder, i.e., if

$$(x_p - x_{CL})^2 + (y_p - y_{CL})^2 \leq r^2$$

The distance of closest approach is derived by minimizing the distance from any point (x',y') along the vector Ω to the point (x_{CL},y_{CL}) in the x-y plane with respect to the parameter t as shown in Figure 5.2.5-1, where the parametric equations along the vector Ω are given by:

$$\begin{aligned} x &= x_0 + \Omega_x t \\ y &= y_0 + \Omega_y t \\ z &= z_0 + \Omega_z t \end{aligned} \qquad (5.2.5\text{-}1)$$

The distance between an arbitrary point (x',y') along Ω and the point (x_{CL},y_{CL}) is given by:

$$D = \sqrt{(x_0+\Omega_x t-x_{CL})^2 + (y_0+\Omega_y t-y_{CL})^2} \qquad (5.2.5\text{-}2)$$

To find the value of t, namely t_p, such that D is minimum (D_{min}) requires setting the derivative d(D)/dt equal to zero at the point of closest approach.

$$\Omega_x(x_0+\Omega_x t_p-x_{CL}) + \Omega_y(y_0+\Omega_y t_p-y_{CL}) = 0 \qquad (5.2.5\text{-}3)$$

If Equation (5.2.5-3) is solved for t_p, the result is

$$t_p = \frac{\Omega_x(x_{CL}-x_0) + \Omega_y(y_{CL}-y_0)}{(\Omega_x^2 + \Omega_y^2)} \qquad (5.2.5\text{-}4)$$

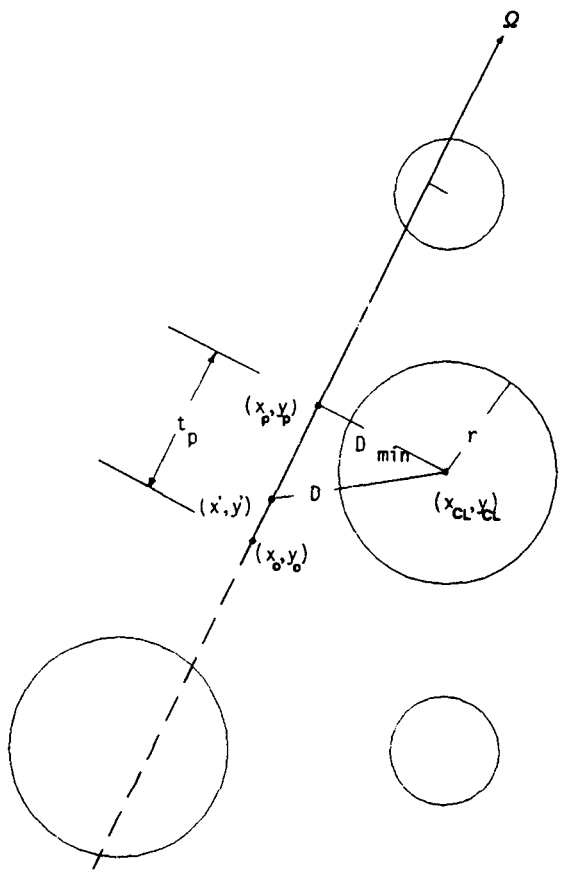

Figure 5.2.5-1 The distance of closest approach.

and the closest point (x_p,y_p) along the path Ω to the point (x_{CL},y_{CL}) in the x-y plane is given by:

$$x_p = x_0 + \Omega_x\, t_p$$
$$y_p = y_0 + \Omega_y\, t_p \qquad (5.2.5\text{-}5)$$

D_{min} is the normal distance from the path of the vector Ω to the point (x_{CL},y_{CL}). Values of t_p less than zero indicate that the infinite cylinder is located in the opposite direction of travel (back track) and can therefore be neglected with the conclusion that in the forward direction of the vector Ω, intersection with the infinite cylinder under consideration is not possible. Once it is concluded that the vector Ω possibly intercepts the infinite cylinder, that is, the minimum approach distance D_{min} is less than the radius r, the intersection points are determined by solving for the intersection with the equation of the circle, i.e., solving Equation (5.2.1-1) with R replaced with the appropriate radius, which should yield two positive roots, d_1 and d_2. It remains to be determined whether the direction vector penetrates the top, bottom, or side wall of the finite (tube) cylinder. Given that z_{top} and z_{bottom} are the z-coordinates of the top and bottom ends of the finite cylinder, and letting $d_{min} = \min(d_1,d_2)$ and $d_{max} = \max(d_1,d_2)$, then the z-coordinates of the intersection points are:

$$z_{min} = z_0 + \Omega_z\, d_{min}$$
$$z_{max} = z_0 + \Omega_z\, d_{max} \qquad (5.2.5\text{-}6)$$

It should be investigated to see if the point (x_0,y_0), where the neutron is located, is within the radius of the infinite tube under

consideration to conclude that the point is within the extension of the finite cylindrical tube. In this case, Equation (5.2.1-2) yields a positive and a negative root; the positive root is taken as d_{max}.

The z-coordinates of Equation (5.2.5-6) are compared with the end z-coordinates of the finite tube to determine the surface of intersection as follows:

I. If the point (x_o,y_o) is not within the extension of the tube, but the minimum approach distance is within the radius of the infinite cylinder, this leads to the following subcases:

   A. $z_{bottom} \leq z_{min} \leq z_{top}$. The vector pierces the side wall of the finite tube and the desired distance to the intersection is $\delta = d_{min}$.

   B. $z_{min} < z_{bottom} < z_{max}$. The vector pierces the bottom surface of the finite tube and the desired distance to the intersection is $\delta = (z_{bottom}-z_o)/\Omega_z$.

   C. $z_{min} \geq z_{top} > z_{max}$. The vector pierces the top surface of the finite tube and the desired distance to the intersection is $\delta = (z_{top}-z_o)/\Omega_z$.

   D. If both z_{min} and z_{max} are less than z_{bottom} or both are greater than z_{top}, then it is concluded that there is no physical intersection with the finite tube in question.

II. Point (x_o,y_o) is within the extension of the tube. In this case Equation (5.2.1-2) yields a positive and a negative root. Provision should be made to account for subcases when the vector Ω is parallel or nearly parallel to the z-axis;

Equation (5.2.1-2) should indicate two imaginary roots in such a subcase. If the z-coordinate of the point (x_0,y_0,z_0) is greater than z_{top} and Ω_z is less than zero, then the vector Ω pierces through the top of the finite tube and the desired distance to the intersection is $\delta = (z_{top}-z_0)/\Omega_z$. If it happens that the z-coordinate of the point (x_0,y_0,z_0) is less than z_{bottom} and Ω_z is greater than zero, then the vector Ω pierces through the bottom of the finite tube and the desired distance is given as $\delta = (z_{bottom}-z_0)/\Omega_z$. The positive root d_{max} is used to calculate z_{max} from Equation (5.2.5-6) and the following subcases are recognized:

A. If $z_0 > z_{top}$ and $z_{max} < z_{top}$, then the vector Ω pierces through the top of the finite tube, and the desired distance is given as $\delta = (z_{top}-z_0)/\Omega_z$.

B. When $z_0 < z_{bottom} < z_{max}$, the vector Ω pierces through the bottom of the finite tube, and the desired distance is given as $\delta = (z_{bottom}-z_0)/\Omega_z$.

C. Otherwise, there is no physical intersection.

The aforementioned procedure to determine if the vector Ω physically intersects a finite tube and to determine the distance to the intersection if it takes place is repeated for each internally protruding tubular extension inside the container cylinder while keeping track of an index specifier of the tube in the case of physical intersection and recording the desired distance as δ_i (i= 1,2,3 for the sample, the source, and the detector tubes, respectively, with δ_i=0 for no intersection). Since it is

simultaneously, as shown in Figure 5.2.5-2, the desired distance to the closest physical intersection with a finite tube is taken to be the non-zero minimum of the set $\{\delta_i\}$

$$\delta = \min\{\delta_i\} \qquad ; \; i = 1,2,3$$

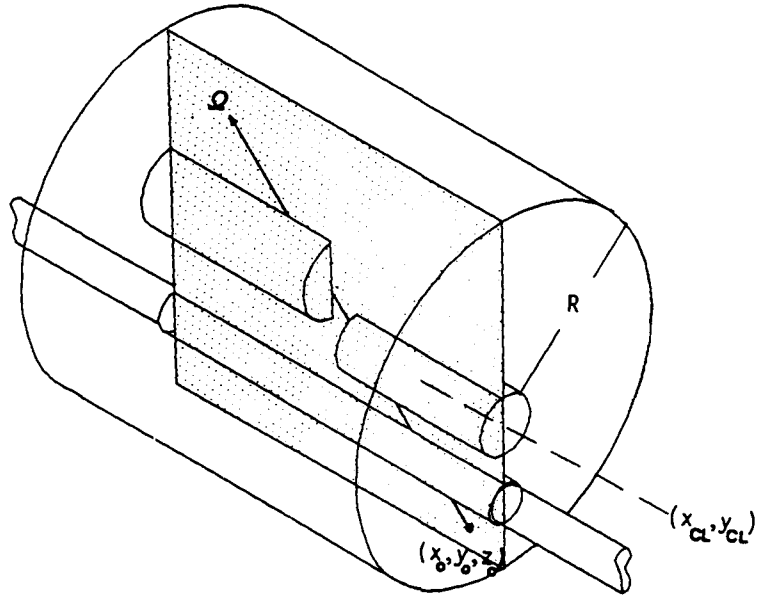

Figure 5.2.5-2 Tracking within the cylindrical container tank.

Finally, in the case when it is concluded that the vector Ω does not intersect any of the finite tubes, the procedure of the solid circular cylinder of Section 5.2.1 is used to determine the intersection surface of and the distance to the cylindrical container tank.

After the distance δ to the boundary of the cell in the direction of flight Ω is obtained by one of the procedures in Section 5.2, the distance to an interaction is sampled as discussed next.

5.3 Sampling the Distance to Interaction (Path Length)

The common procedure of sampling the path length in a multi-region (multi-cell) geometry assuming successive infinite media was used. A distance D^* to an interaction is sampled assuming an infinite medium of the current cell composition. If this distance exceeds the distance to the boundary of the present cell in the dirction of travel, then the position coordinates are advanced to the cell boundary and the procedure of infinite medium of the adjacent cell composition is assumed to sample a path length. This procedure is repeated successively until an interaction is sampled within the cell under consideration or until the traveling radiation leaks out of the system.

The path length sampled from the exponential pdf governing the interaction probability within a medium is given by Equation (A-1) as:

$$D^* = - \frac{1}{\Sigma_t} \ln\xi \qquad (5.3\text{-}1)$$

When the random number $\xi \in (0,1)$, then $D^* \in (0,\infty)$.

An exception is made when the intercepted boundary is an external boundary of the system (in which case the neutron is assumed to not have a chance to re-enter the cell geometry). In this case, the neutron is forced to remain within the geometry (within the distance to the boundary) with a weight equal to the probability of not escaping the cell, namely:

$$W_{D^*} = 1 - e^{-\Sigma_t \delta} \qquad (5.3\text{-}2)$$

(This is shown to be a variance reduction technique in Appendix A, by eliminating the loss of neutron histories that would have escaped outside the system). Thus, the neutron is forced to have its collision within the cell; the path length is sampled from the altered pdf of Equation (A-2) as:

$$D^* = -\frac{1}{\Sigma_t} \ln\left[1 - \xi(1 - e^{-\Sigma_t \delta})\right] \qquad (5.3\text{-}3)$$

5.4 Decision Whether the Neutron is Still Within the Cell

This decision is made by comparing the path length D^* to an interaction, sampled in Section 5.3, with the distance to the cell boundary δ in the direction of flight that has been computed in Section 5.2.

Should the sampled distance exceed the distance to the boundary (i.e., if $D^* \geq \delta$), it is concluded that no interaction occurs in the cell and the neutron escapes the current cell. The neutron position cartesian coordinates are advanced in the direction Ω to the cell boundary (refer to Section 5.7 for an explanation of how this is achieved to overcome round-off errors) by using the parametric Equations (5.2-1) in order to position the point (x_0, y_0, z_0), where the neutron had its previous collision, to the point (x_n, y_n, z_n) located just inside the neighboring cell along direction Ω. Otherwise, when $D^* < \delta$, it is decided that an interaction occurs within the cell and the cartesian coordinates of

the neutron position in the phase space are relocated to the collision position (x_n, y_n, z_n) using Equations (5.2-1) with d replaced by the sampled distance (path length to the collision) D^*, and the collision event is handled.

5.4.1 Sampling the Collision Event

At the point where it was decided that the neutron had a collision, the type of interaction, whether it is absorption, scattering, etc., has to be sampled. The "expected value" concept, a variance reduction technique which consists of replacing the cumulative density function sampling scheme to sample the reaction type, as shown in Appendix B, may result in having to terminate the history upon absorption without a favorable contribution to the desired results with the deterministic probability of scattering, namely Σ_s/Σ_t. In this case the weight of the neutron is reduced by the scattering probability $W_{sc} = \Sigma_s/\Sigma_t$, that is, the random process of occurrence of interactions is replaced by its expected value.

5.4.2 Treatment of the Scattering Event

The scattering event, decided upon in Section 5.4.1, is simulated by sampling the scattering parameters to determine the scattered neutron state in the phase space. The state of the scattered neutron is determined by sampling the energy and/or the scattering angle of the neutron after being scattered. Therefore, an appropriate scattering model has to be chosen, which in turn

requires that the element (nucleus) with which the neutron had its scattering interaction be sampled.

An energy limit of 2 eV was decided upon (Appendix C) below which the thermal scattering (the monatomic gas) model was used; otherwise, a non-thermal scattering model (either the elastic billiard ball model or the inelastic scattering model) was used. Mathematical representations of these models are discussed in Sections 5.4.2.1 and 5.4.2.2, respectively.

The element involved in the scattering reaction is sampled from the scattering cdf (discrete function). The element, having the identifier i' = m+1, is sampled by determining that value of m which satisfies:

$$\sum_{i=0}^{m} \Sigma_{i,s} < \xi\Sigma_s \leq \sum_{i=0}^{m+1} \Sigma_{i,s} \qquad (5.4.2\text{-}1)$$

where $\Sigma_s = \sum_{i=1}^{M} \Sigma_{i,s}$

and $\Sigma_{0,s} = 0$

where $\Sigma_{i,s}$ is the macroscopic scattering cross section for the i-th element in the cell; M is the number of elements in the cell.

5.4.2.1 Thermal Scattering, The Monatomic Gas Model

The integrand on the right hand side of Equation (2.1.5-11) is proportional to the probability density function given by Equation (2.1.5-8), which represent the target nucleus velocity distribution in the transformed variable x. Carter and Cashwell (1975) give a simplified rejection scheme, with about 40% efficiency, to sample a target nucleus velocity from this distribution when $x < 3$

(equivalent to target velocities **V** > 9kT). The total probability of $x > 3$ is less than 0.00125. Therefore, neglecting target velocities for $x > 3$ should not introduce any significant biasing in the sampling scheme. The distribution of μ, the cosine of the angle between the target nucleus velocity **V** and the neutron velocity v_n is given by the cosine law, namely:

$$f'(\mu) = \sqrt{v_n^2 + V^2 - 2v_n V\mu} \qquad (5.4.2.1\text{-}1)$$

or in terms of the new transformed variables $\alpha = \beta v_n$ and x, where β and x are defined by Equations (2.1.5-7) and (2.1.5-6), respectively.

$$f(\mu) = C\sqrt{\alpha^2 + x^2 - 2\alpha x\mu} \qquad (5.4.2.1\text{-}2)$$

where C is a normalization coefficient. This equation can be sampled analytically as:

$$\mu=\frac{1}{2\alpha x}[\alpha^2+x^2-(|\alpha-x|^3-\xi(|\alpha-x|^3-(\alpha-x)^3))^{2/3}] \qquad (5.4.2.1\text{-}3)$$

The following scheme for sampling the monatomic gas kernel is adopted from (Carter and Cashwell, 1975).

I. Sample the target nucleus velocity from the transformed dimensionless variable x (restricted to $0 \leq x \leq 3$) from Equation (2.1.5-8) (Maxwellian) by the rejection technique as:

   A. Evaluate $[p(x)]_{max}$ by setting the derivative $dp(x)/dx$ equal to zero. The x at which this maximum value occurs is $x = \pm 1$. This value of x is substituted into Equation

(2.1.5-8) to obtain a numerical value for $[p(x)]_{max}$ of 0.830214995.

B. Sample a variable x_1 on the possible range of $x \in (0,3)$ as $x_1 = 3\,\xi$, since when $\xi \in (0,1)$, then $x_1 \in (0,3)$.

C. Evaluate the pdf $p(x)$ of Equation (2.1.5-8) at this value of x, namely:

$$p(x_1) = \frac{4}{\sqrt{\pi}}\, x_1^2\, e^{-x_1^2}$$

D. Evaluate a variable $\eta = \xi\,[p(x)]_{max}$; if $\eta > p(x_1)$, reject x_1 as the sampled variable and repeat step B. If $\eta \leq p(x_1)$, accept $x^* \equiv x_1$, as to be the randomly sampled variable of the target nucleus velocity.

II. Sample the cosine of the angle (denoted μ_t) between the target nucleus and neutron directions using direct sampling from Equation (5.4.2.1-3) with x replaced by x^*. The accepted value of x is sampled in step I.D above.

III. Sample the azimuthal angle ϕ about the direction of flight of the incident neutron uniformly by Equation (5.1-4). Knowing the incident neutron direction of flight $(\Omega_x,\Omega_y,\Omega_z)$, the "scattering" angle is sampled in step II ($\mu_t=\cos\theta$), and the azimuthal angle ϕ. Equations (5.1-1) are used to evaluate the direction cosines of the target nucleus $(\Omega^T_x,\Omega^T_y,\Omega^T_z)$. Then the direction cosines relative to the master coordinates $(\Omega^T_x,\Omega^T_y,\Omega^T_z)$ are obtained from Equations (5.4.3-1). If the neutron is assumed to be oriented isotropically after the scattering in the center-of-mass frame, the polar angle θ_0 and

the azimuthal angle ϕ_0 are sampled from the isotropic sampling of Equations (5.1-3) and (5.1-4), respectively. The direction cosines, in the center-of-mass system, of the neutron after the collision $(\hat{\Omega}_x, \hat{\Omega}_y, \hat{\Omega}_z)$ are calculated from Equations (5.1-1) with θ and ϕ replaced by θ_0 and ϕ_0, respectively. The final neutron energy E' and direction of flight cosines $(\Omega'_x, \Omega'_y, \Omega'_z)$ in the laboratory system are given by :

$$E' = \frac{E}{(A+1)^2}\,(X^2+Y^2+Z^2) \qquad (5.4.2.1\text{-}4)$$

$$\Omega'_x = \frac{X}{\sqrt{X^2+Y^2+Z^2}}$$

$$\Omega'_y = \frac{Y}{\sqrt{X^2+Y^2+Z^2}}$$

$$\Omega'_z = \frac{Z}{\sqrt{X^2+Y^2+Z^2}} \qquad (5.4.2.1\text{-}5)$$

where

$$X = \Omega_x + A\left(\delta\hat{\Omega}_x + \frac{X^*}{\alpha}\hat{\Omega}_x^I\right)$$

$$Y = \Omega_y + A\left(\delta\hat{\Omega}_y + \frac{X^*}{\alpha}\hat{\Omega}_y^I\right)$$

$$Z = \Omega_z + A\left(\delta\hat{\Omega}_z + \frac{X^*}{\alpha}\hat{\Omega}_z^I\right)$$

$$\delta = \sqrt{1 + \left(\frac{X^*}{\alpha}\right)^2 - \frac{2X^*}{\alpha}\mu_l}$$

Appendix C shows that sampling the monatomic gas kernel by this procedure is equivalent to the well-known Wigner-Wilkins proton gas theoretical model (Duderstadt and Hamilton, 1976).

5.4.2.2 Non-Thermal Scattering Treatment

The element i', sampled to be responsible for the scattering, might exhibit a significant cross section for the inelastic scattering interaction. This is dependent on the energy of the incident neutron, if it is high enough above the threshold of this reaction. Table 5.4.2.2 lists the first nuclear level excitation energy for some elements of interest, constituents of the monitoring system. In this work only Pb was modeled to undergo inelastic scattering, up to the 35^{th} discrete level. Therefore, if the element, sampled above, happened to be Pb, then the scattering type is sampled from the discrete cummulative distribution of the scattering cross sections as:

If $\xi \leq \sigma_{is}(E)/\sigma_s(E)$, where σ_{is} and σ_s are the microscopic inelastic and total (elastic and inelastic) scattering cross sections (σ_{is} is the summation of the 35 discrete level excitation cross sections), then the scattering is deemed to be inelastic and the responsible (m+1) discrete level is sampled when the inequality

$$\sum_{k=1}^{m} \sigma_{is,k} < \xi\sigma_{is} \leq \sum_{m}^{m+1} \sigma_{is,k}$$

is satisfied. Otherwise, when $\xi > \sigma_{is}(E)/\sigma_s(E)$, the scattering is elastic.

The angular scattering for Pb is highly anisotropic even when viewed in the center-of-mass system. The anisotropic law is supplied as Legendre polynomial expansions, the cosine of the

1st Excitation Level (MeV)	Isotope	Natural Abundance (%)	Observed * Inelastic γ-ray (MeV)
4.43	C-12	98.892	4.439
6.052(6.131)	O-16	99.759	6.131
0.439	Na-23	100.00	0.44
1.36853	Mg-24	78.60	N.A.
0.58	Mg-25	10.11	N.A.
1.81	Mg-26	11.29	N.A.
0.842	Al-27	100.00	0.843
1.780	Si-28	92.18	1.779
1.28	Si-29	4.71	1.273
2.23	Si-30	3.12	2.235
1.22	Cl-35	75.53	1.22
0.84	Cl-37	24.47	N.L.
1.74	Ca-40	96.79	N.L.
1.95	Ca-44	2.06	N.L.
0.8894	Ti-46	7.99	N.A.
0.16	Ti-47	7.32	N.A.
0.9833	Ti-48	73.99	N.A.
1.31	Ti-49	5.46	N.A.
1.55	Ti-50	5.25	N.A.
0.7831	Cr-50	4.31	0.7831
1.4336	Cr-52	83.76	N.L.
0.563	Cr-53	9.55	0.564
0.8353	Cr-54	2.38	0.8348
0.1259	Mn-55	100.00	N.A.
1.409	Fe-54	5.84	1.4084
0.8469	Fe-56	91.68	0.8468
0.01439	Fe-57	2.17	N.L.
0.8105	Fe-58	0.31	N.L.
1.45	Ni-58	67.76	N.A.
1.3325	Ni-60	26.16	N.A.
0.0674	Ni-61	1.25	N.A.
1.172	Ni-62	3.66	N.A.
1.34	Ni-64	1.16	N.A.
0.669	Cu-63	69.1	N.L.
0.77	Cu-65	30.9	N.L.
1.04	Ge-70	20.55	N.A.
0.69(0.835)	Ge-72	27.37	N.A.
0.0135	Ge-73	7.67	N.A.
0.596	Ge-74	36.74	N.A.
0.5632	Ge-76	7.67	N.A.
1.54	Mo-92	15.86	N.A.
0.871	Mo-94	9.12	N.A.
0.2042	Mo-95	15.7	N.A.
0.778	Mo-96	16.5	N.A.
0.665	Mo-97	9.45	N.A.
0.7868	Mo-98	23.75	N.A.
0.5355	Mo-100	9.62	N.A.
0.6327	Cd-106	1.22	N.A.
0.63	Cd-108	0.88	N.A.
0.6576	Cd-110	12.39	N.A.
0.247	Cd-111	12.75	N.A.
0.6174	Cd-112	24.07	N.A.
0.3	Cd-113	12.26	N.A.
0.5581	Cd-114	28.86	N.A.
0.8993	Pb-204	1.4	N.A.
0.8033	Pb-206	25.1	N.A.
0.5696	Pb-207	21.7	N.A.
2.6145	Pb-208	52.3	N.A.

* From SIGRMCCS listings, MCNP

Table 5.4.2.2 The first nuclear level excitation energy for some elements of interest.

scattering angle, $\mu = \cos\psi$, being sampled from Equation (D-2), repeated here for convenience:

$$\frac{1}{2}(\mu+1) + \sum_{n=1}^{NL} \frac{a_n(E)}{2} [P_{n+1}(\mu) - P_{n-1}(\mu)] = \xi$$

The desired μ can then be obtained by a numerical root finding scheme (e.g., the bi-section method).

The outgoing neutron energy after being scattered through the sampled angle ψ is computed from Equation (2.1.5-12).

The scattering angle ψ is transformed into the laboratory system where the neutron tracking is done by Equation (2.1.5-13), whereas the azimuthal angle around the incident direction is sampled by Equation (5.1-4). In the case of neutron scattering by hydrogen, the corresponding equations to compute the scattered neutron energy and the scattering angle in the laboratory system are simplified and given by Equations (5.4.2.2-1) and (5.4.2.2-2), respectively.

$$E' = \xi E \qquad (5.4.2.2\text{-}1)$$

$$\cos\theta = (\xi)^{1/2} \qquad (5.4.2.2\text{-}2)$$

where $\xi \in (0,1)$.

When the sampled element responsible for the scattering is not modeled to undergo inelastic scattering, then the billiard ball model was used directly. The polar and azimuthal scattering angles were determined by Equations (5.1-3) and (5.1-4) respectively. Post scattering laboratory energy and polar angle were obtained from Equation (2.1.5-12) and (2.1.5-13), respectively.

5.4.3 Computing the Direction Cosines of the Neutron Flight Direction Leaving the Scattering Point

After the scattering angle θ (lab system) and the rotational angle ϕ are sampled, the emerging neutron direction cosines (with respect to the master cartesian coordinates) can be computed (Cashwell and Everett, 1959), given the incident (before scattering) direction cosines as Ω_x, Ω_y, and Ω_z from:

$$\Omega_x' = \Omega_x \cos\theta + \Omega_x\Omega_z \frac{\sin\theta \cos\phi}{\sqrt{1-\Omega_z^2}} - \Omega_y \frac{\sin\theta \sin\phi}{\sqrt{1-\Omega_z^2}}$$

$$\Omega_y' = \Omega_y \cos\theta + \Omega_y\Omega_z \frac{\sin\theta \cos\phi}{\sqrt{1-\Omega_z^2}} - \Omega_x \frac{\sin\theta \sin\phi}{\sqrt{1-\Omega_z^2}}$$

$$\Omega_z' = \Omega_z \cos\theta - \sqrt{1-\Omega_z^2} \sin\theta \cos\phi \qquad (5.4.3\text{-}1)$$

In the case when $(1-\Omega^2_z)^{\frac{1}{2}}$ approaches zero (for practical applications if $|\Omega_z| > 0.99999$) the degenerate forms of Equations (5.4.3-1) are given as (Schaeffer, 1973):

$$\Omega_x' = \sin\theta \cos\phi$$

$$\Omega_y' = \sin\theta \sin\phi$$

$$\Omega_z' = \Omega_z \cos\theta \qquad (5.4.3\text{-}2)$$

5.5 Scoring Routine

Since it is of interest in this work to score the prompt gamma rays from neutron capture in some elements of interest in the core sample, the scoring routine is performed only when the neutron being

tracked is in the core sample material (cells 14, 15, 17, 22, and 23). At each point of collision inside the core sample, the expected value technique was used to score an expected value of contribution to the desired result. This expected value is constructed as probability of occurrences. For example, the probability that the collision is a radiative capture reaction is:

$$P_a = \frac{\Sigma_a(E)}{\Sigma_t(E)} \qquad (5.5\text{-}1)$$

where Σ_a and Σ_t are the macroscopic absorption and total cross sections, respectively.

The probability that the radiative capture takes place in the j-th constituent element of interest in the core sample is:

$$P_{a,j} = \frac{\Sigma_{a,j}(E)}{\Sigma_a(E)} \qquad (5.5\text{-}2)$$

The probability that upon radiative capture in the j-th element, the k-th characteristic capture gamma ray is emitted is:

$$P_{a,j,k} = \frac{\Sigma_{a,j}(E)}{\Sigma_a(E)} \Upsilon_{j,k} \qquad (5.5\text{-}3)$$

where $\Upsilon_{j,k}$ is the branching ratio of the k-th capture gamma ray when emitted by element j.

The probability that the isotropically emitted gamma ray (Kinsey, 1979) is emitted within the solid angle $\Delta\Omega$ subtended by the detector at the point of collision is the fractional solid angle:

$$P_\Omega = \frac{\Delta\Omega}{4\pi} \qquad (5.5\text{-}4)$$

The prompt gamma rays when emitted from the elements of interest are forced to be emitted within the solid angle subtended by the finite size detector at the point of neutron capture. This is accomplished by restricting the otherwise isotropically emitted gamma rays ($0 \leq \theta \leq \pi$ and $-\pi \leq \phi \leq \pi$) to limited ranges of polar and azimuthal angles determined by the relative position and distance between the point of emission and the detector. Thus, θ and ϕ are sampled over these limited ranges and the corresponding weight is the fractional solid angle subtended by the detector. Gardner *et al.* (1987) treated the forcing of radiation scattered or emitted from an arbitrary point to a right circular cylinder detector. The algorithm used here to determine the limiting polar and azimuthal angles and the solid angle is based on the reported work by Mickael *et al.* (1988). The general approach of this algorithm is outlined in Appendix F; more details can be found in the aforementioned references.

The probability that a gamma ray of energy E emitted at a point will traverse a distance x_i in the direction of flight in material i possessing a mass attenuation coefficient $(\mu/\rho)_i$ at the given energy E and density ρ_i is given as:

$$P_x = \prod_{i=1}^{M} e^{-(\frac{\mu}{\rho})_i \rho_i x_i}$$

or

$$P_x = e^{\sum_{i=1}^{M} -(\frac{\mu}{\rho})_i \rho_i x_i} \qquad (5.5\text{-}5)$$

The summation (from 1 to M) is carried over all the materials

located between the point of emission and the detector. The gamma ray path from the point of emission to the detector is defined by the polar angle θ and the azimuthal angle ϕ (sampled from the limited ranges). The distance through the sample and various construction and shielding materials has to be computed. In this work, detailed attenuation by the sample, shields, construction materials, moderator, the detector casing and air surrounding the crystal, along with a reasonable approximation of the associated detector support structure, were considered. The attenuation and traversed thicknesses through the source tube were considered only when it happens that the path of the gamma ray under consideration intercepts the tube containing the source. Considerable effort was exerted to write and test computational subroutines to determine the successive path lengths through the heterogeneous constituents of a tube assembly in any arbitrarily conceivable direction of penetration from the point of emission within the sample to the detector. The general approach of tracking inside coaxial cylindrical and annular configurations intersected by planes that are perpendicular to the major axis is outlined as:

I. For a cylindrical geometry, knowing the direction of flight vector Ω and the point of emission p within the cylinder (emission from within the core sample), the z-coordinate of the point of emission determines the relative location with respect to given planes perpendicular to the major axis colinear with the z-direction, say z_1 and z_2, as illustrated in Figure 5.5(a).

II. Solving the quadratic equation for the roots of intersection between the vector Ω and the equation of a circle (planar projection of the tube) should yield one positive and one negative root. The positive root is chosen to compute the coordinates of the intersection point in the direction of flight. The z-coordinate of the point of intersection determines the intersection to be on either side of a plane, at say z, as shown in Figure 5.5(b).

III. The projection of the radial distance r on the x-y plane at z is determined by first computing the distance from the point p to the plane at z as:

$$d = \frac{(z-z_p)}{\Omega_z} \qquad (5.5\text{-}6)$$

The x and y coordinates of the intersection point at the plane z are computed from the parametric equations:

$$x = x_p + \Omega_x\, d$$

$$y = y_p + \Omega_y\, d$$

Given that the major axis of the tube is at (x_c,y_c), the projection of the radial distance is computed from:

$$d_r = \sqrt{(x-x_c)^2 + (y-y_c)^2} \qquad (5.5\text{-}7)$$

This radial distance, when compared with a given radius (say a tube of radius r_1), determines whether the subsequent region should be region I or region II, as shown in Figure 5.5(c).

IV. For a conical shape inside a cylindrical geometry, the radial distance d_r, when compared with the radii r_1 at plane z_1 and

r_2 at plane z_2, determines whether or not the equation of the conical surface has to be solved for the intersection point, as can be seen from Figure 5.5(d).

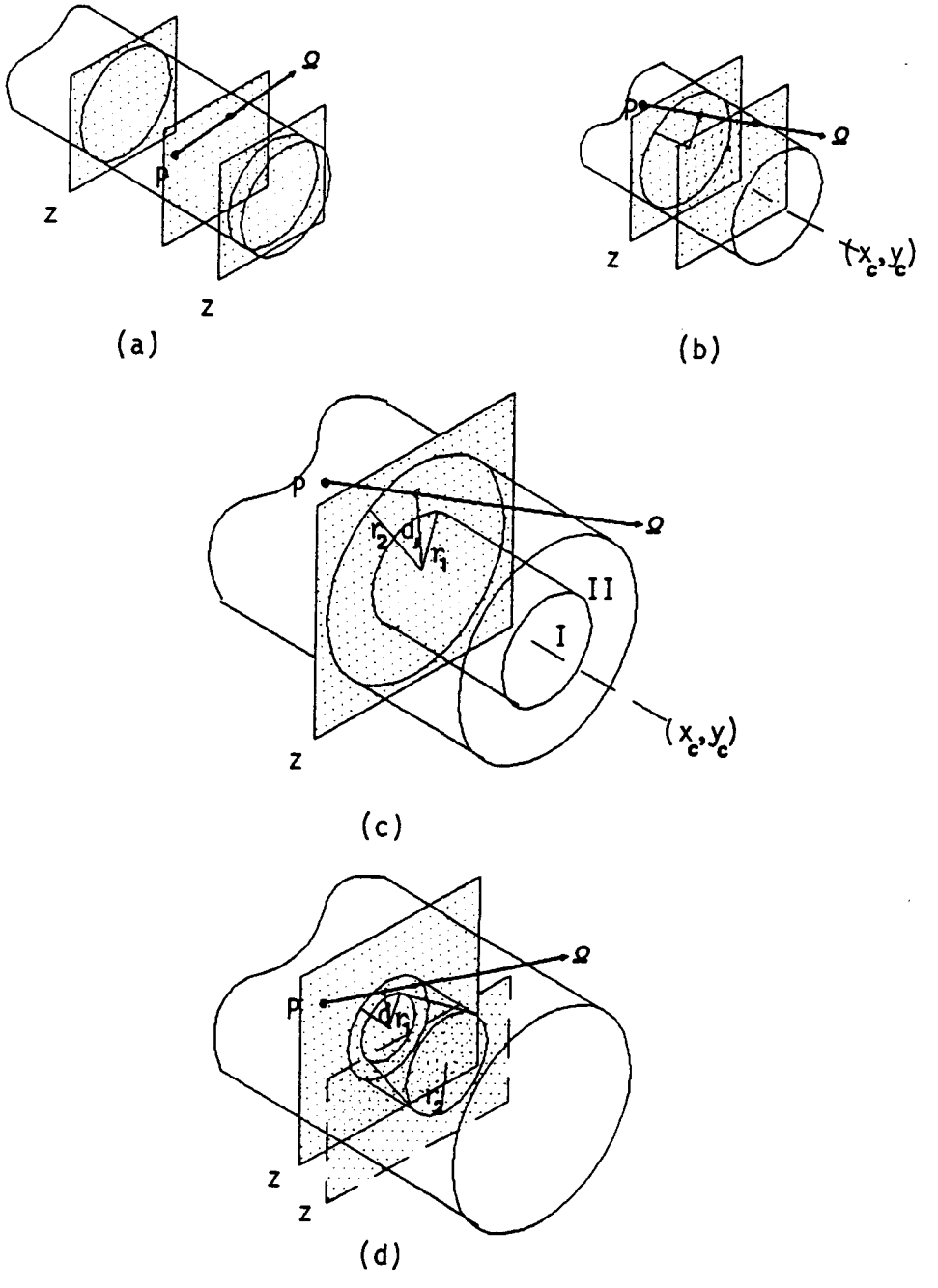

Figure 5.5 General geometry illustrations to determine the length/material traversed between the source and the detector.

V. Conveniently, the position coordinates can be updated to each interaction point while keeping track of the distance traversed, along with an index identifier of the material that comprises the penetrated medium. This material index allows the distances through the same materials to be summed up. The direction of flight Ω has to remain unchanged.

VI. The above procedures are repeated until the intersection point is at the detector surface.

The probability that a gamma ray of energy E, impinging upon the effective volume of the detector, will contribute to the counts under the full energy peak at E is the experimentally obtained and reported photopeak efficiency values (see Section 5.9) at the incident energy E:

$$P_{count} = \zeta_{photopeak}(E) \qquad (5.5\text{-}8)$$

The gamma rays reaching the detector are forced to contribute to the net count area under the relevant photopeaks according to their respective photopeak efficiencies (expressed as net counts per incident gamma ray). The detector intrinsic efficiency is dependent on the point and angle of entry of the gamma ray. Therefore, it is assumed that suitable experimental efficiency values are averaged over the emanation point and incident angles, and therefore the efficiency is only dependent on the detector size, gamma ray energy, and the specific peak (photopeak, single escape, or double escape) under consideration. Thus, the intrinsic detector efficiency is independent of the gamma ray position coordinate. The relative

detection efficiencies for different gamma ray peaks depend not only on characteristics of the gamma ray detector and the nature of the spatial distribution of the source of gamma rays, but also on the gamma ray attenuation in the sample and in the materials which surround the detector.

Neutron interactions within the detector, that result in events which are recorded in the spectra, such as the recoil-broadened 0.596 MeV and 0.691 MeV lines from the $^{74}Ge(n,n'\gamma)$ and the $^{72}Ge(n,n'\gamma)$ reactions, respectively, are not modeled. The 0.691 MeV line, which is produced by neutrons with energies > 0.7 MeV, is useful in that it provides a measure of the total number of fast neutrons which have interacted within the detector and hence of the degree of neutron damage; this can provide an early warning of consequent deterioration of the detector energy resolution.

Therefore, the expected probability of contribution is the probability that Equations (5.5-1) through (5.5-5) and Equation (5.5-8) occur simultaneously, that is:

$$P_{score} = W_n \; P_a \; P_{a,j,k} \; P_\Omega \; P_x \; P_{count} \qquad (5.5\text{-}9)$$

where W_n is the absolute weight of the neutron prior to the collision.

Effectively, the net (interference-free) peak area count rate of the k-th gamma line emitted by the j-th element of interest in the sample having a fractional weight (concentration) of w_j is given by:

$$R_{k,j}=N_j\left[\gamma_{j,k}\sigma_{a,j}\zeta_k \int_{\text{sample}} dr\ N(r) \int_{\theta_{min}}^{\theta_{max}}\int_{\phi_{min}}^{\phi_{max}} \frac{d\Omega}{4\pi}\ e^{-\sum_{i=1}^{M}\left(\frac{\mu}{\rho}\right)_i\rho_i x_i}\ dx_i\right] \tag{5.5-10}$$

where:

$R_{k,j}$ is the net peak area count rate from the k-th line emitted by the j-th element.

N_j is the number density of the j-th element.

$T_{j,k}$ is the branching ratio for the k-th gamma line emitted by the j-th element.

$\sigma_{a,j}$ is the microscopic neutron capture cross section.

ζ_k is the intrinsic detector efficiency for the k-th gamma ray energy

$N(r)$ is the neutron density in units of (neutron/cm^3/s)

$(\mu/\rho)_i$ is the mass attenuation coefficient for material i of density ρ, and

x_i is the distance, in the direction of flight, that the gamma ray has to traverse in material i to reach the detector.

The integration is over the solid angle that the detector subtends from the point of emission of the capture gamma ray.

5.6 Termination of the History

Two physical processes are responsible for neutron losses, namely absorption and escape. Absorption is accounted for by reducing the weight of the neutron by its absorption probability at each collision (i.e., by multiplying the weight before the collision by the non-absorption probability). Escape is accounted for by

reducing the weight by the escape probability (when the sampled path length exceeds the distance to an outer physical boundary of the system, as explained in Section 5.3).

It is seen that no matter how many collisions the neutron suffers, the weight will never become zero. There has to be some way of "killing" the neutrons while conserving the total neutron weight.

Terminating the history when the neutron energy slows down past a low pre-specified cutoff energy is not desirable since calculations of thermal parameters are of interest. Instead Russian Roulette is employed to decide the fate of a neutron when its weight is reduced below a pre-specified cutoff weight limit (W_{min}), determined such that subsequent contributions to the desired results are insignificant below this weight and the fraction of computer time in tracking the neutron further is a waste.

Russian Roulette (Carter and Cashwell, 1975) is a variance reduction technique implemented such that when the neutron absolute weight W becomes smaller than the minimum permissible weight W_{min}, i.e., $W < W_{min}$, a random number $\xi \in (0,1)$ is sampled and compared with the ratio W/W_{min}. If $\xi \leq W/W_{min}$, then the neutron survives and its weight is adjusted (increased by the ratio W_{min}/W) to be W_{min} and the history is continued either within the cell or in the neighboring cell (following the succession of Sections 5.2 through 5.4).

If $\xi > W/W_{min}$, the neutron perishes (is killed), and the history is terminated. The simulation is continued starting with

Section 5.1, and the whole procedure is repeated as many times as necessary to achieve the accuracy needed for the solution or until the total specified number of histories is exhausted.

5.7 Cell Boundary Interface Complications

Due to round-off and truncation errors in representing numbers on a digital computer, the following difficulty may arise. A point is supposed to lie on a surface bounding a cell when the neutron escapes interactions in the current cell and is relocated to be on the boundary. In reality, this relocation might be within $\pm\epsilon$ of the boundary. When the geometrical equations are solved to determine the distance to the next boundary, this will lead to a serious error because of the logic in decisions involved in the determination of positive or negative roots. This complication can be avoided by advancing the point so that it lies a small distance wholly within the neighboring cell it is supposed to enter next. This is believed to be the most satisfactory treatment except at corners or if very thin regions are present (Kalos and Whitlock, 1986).

The above treatment was implemented in the neutron tracking subroutines such that a test is made to ensure that the particle is within the cell before solving for the roots of intersection of the flight vector and the equation of the cell surface. Then all the logical decisions are based on the neutron being within the cell geometry. The advancement of the neutron to the next cell had it escaped its present cell is dealt with as follows. After sampling

the distance to the boundary in the direction of flight, say δ, then the path length is sampled, say D^*. If the sampled distance presumably locates the neutron within a small distance ϵ (10^{-8} cm) inside the boundary (same cell), that is, if $D^* \geq \delta-\epsilon$, then the neutron is advanced to the next cell in the direction of flight and is located just beyond the boundary within the new cell by stretching the distance on the right hand side of the above inequality slightly, say to $(\delta-\epsilon) + 2\epsilon$.

The position coordinates are computed by Equation (5.2-1) with d replaced by the distance $(\delta+\epsilon)$.

5.8 Correlated Sampling

To generate the desired detector responses in this work, it is of interest to obtain the responses while the elemental concentrations are small to allow treating the problem as perturbations of a single case with strong positive correlation. The correlated sampling technique (Spanier and Gelbard, 1969) can be utilized to avoid separate Monte Carlo calculations for each system of elemental concentrations. Instead, it is possible to correlate the problems by using a single set of particle histories. The base (reference elemental concentrations) problem is simulated and the effects of the perturbations to obtain the other elemental concentrations are calculated at each collision by weight factors that account for the relative changes in the collision process.

Separate simulations for each elemental concentrations, in addition to being very impractical, may not provide accurate

information about the differential effects, due to fact that the statistical uncertainties in the estimates may mask the differences being sought. However, in the correlated sampling technique, only the effects of the perturbation are subject to statistical fluctuations.

In the special case when the neutron is in a cell occupied by the core sample material (whose prompt gamma ray response is of interest), namely cells 14, 15, 17, 22, and 23, the unbiased path length sampling is done through Equation (5.3-1). In the non-reentrant case, Equation (5.3-3) is used. In both cases Σ_t evaluated at the reference elemental concentrations. The relative weights, used to force non-escape and subsequent interaction to take place within the sampled path length D^* in the core sample (at reference elemental concentration) at different elemental concentrations, are computed from:

$$W_{D^*,\perp} = \frac{\Sigma_{t,\perp}\ e^{-\Sigma_{t,\perp}\ \delta}}{\Sigma_{t,\perp_{ref}}\ e^{-\Sigma_{t,\perp_{ref}}\ D^*}} \qquad (5.8\text{-}1)$$

The relative weights that no interaction takes place within δ in the sample at all elemental concentrations are computed as:

$$W_{\delta,\perp} = \frac{e^{-\Sigma_{t,\perp}\ \delta}}{e^{-\Sigma_{t,\perp_{ref}}\ \delta}} \qquad (5.8\text{-}2)$$

It should be noticed that relative weights are not computed for materials other than the core sample material, since neutron transport within these materials is essentially independent of the core sample elemental concentrations.

Within the core sample when the element involved in the scattering of the neutron is sampled by Equation (5.4.2-1) where Σ_s values are evaluated at the reference elemental concentrations, the relative weights to force the scattering to be with the same responsible sampled element at all elemental concentrations are computed as:

$$W_{sc,i',\perp} = \frac{\frac{\Sigma_{i',s,\perp}}{\Sigma_{s,\perp}}}{\frac{\Sigma_{i',s,\perp_{ref}}}{\Sigma_{s,\perp_{ref}}}} \qquad (5.8\text{-}3)$$

At each collision in the core sample, the expected value given by Equation (5.5-9) is scored as the desired contribution, and Equations (5.5-1) and (5.5-3) are evaluated at the reference elemental concentrations. The first term in the summation of Equation (5.5-5) (defining material number one to be the core sample material) is evaluated at the reference elemental concentration of the core sample.

The relative weights at different elemental concentrations for the first term of Equation (5.5-5) are computed as:

$$W_{P_{x,1,\perp}} = \frac{e^{-(\frac{\mu}{\rho})_{1,\perp} \rho_{1,\perp} x_1}}{e^{-(\frac{\mu}{\rho})_{1,\perp_{ref}} \rho_{1,\perp_{ref}} x_1}} \qquad (5.8\text{-}4)$$

The relative weights for Equations (5.5-1) and (5.5-3) combined are:

$$W_{P_{a,j,\perp}} = \frac{\frac{\Sigma_{a,j,\perp}}{\Sigma_{t,\perp}}}{\frac{\Sigma_{a,j,\perp_{ref}}}{\Sigma_{t,\perp_{ref}}}} \qquad (5.8\text{-}5)$$

5.9 Features of the Simulation

The geometrical representation of the monitoring system is very accurate with reasonable approximations in modeling the Cf-252 encapsulation and the housing of the detector proper that contains the detector support structure. Inherently, the cell-to-cell interface is assumed to be a perfect match, which is somehow questionable when the interface is between two physically different cells. To overcome this difficulty,fabrication tolerances are restricted to be minimal and can be assumed as practically close match in between the material-to-material interface. Furthermore, the path length over-shooting of Section 5.7 somehow relaxes this constraint.

The neutron transport simulation is an accurate detailed treatment of continuous neutron energy with extensive pointwise cross section data from ENDF/B-V. Nuclear absorption and scattering reactions are accounted for in all the elements in the material constituents of the monitoring system. The scattering reaction is assumed to be predominantly isotropic elastic scattering, except in the lead shield surrounding the source capsule where the neutron energy spectrum is approximately the Cf-252 neutron spectrum, which is a hard spectrum, and inelastic scattering in Pb is significant. Hence, inelastic scattering in Pb due to the first 35 discrete nuclear excitation levels is considered in addition to the elastic scattering. Due to the high mass ratio of the Pb nucleus and the hard neutron spectrum in this vicinity, the

scattering is anisotropic and is modeled as such.

Inelastic scattering is not accounted for in heavy nuclei that exhibit a possibility of inelastic scattering reactions, as shown in Table 5.4.2.2, and comprise a small weight fraction of the material, since under these conditions there is usually a small probability of occurrence for inelastic scattering. Specific examples are the heavy elements in the core sample, where the neutron flux is thought to be well thermalized. The ratio of thermal (0-2 eV) to epithermal (2 eV - 15 keV) neutron flux densities is essentially constant beyond about 10 cm from a point source of Cf-252 in fresh water, the thermal flux density being several times higher than the epithermal flux density (Senftle *et al.*, 1974). The heavy elements in the stainless steel source encapsulation are modeled to account for absorption and isotropic elastic scattering reactions, because it is thought that the small energy and angular dependency resulting from anisotropic inelastic scattering will be washed away in the neutron flux at the region of interest (the core sample), since the neutrons have to transport through the Pb shield and a considerable path length of good moderators (polyethylene and water).

Scattering of neutrons at thermal energies ($E \leq 2$ eV), comparable to the thermal agitation energy of the nuclei comprising the medium, is treated by the monatomic gas model. This model is thought to adequately describe the physical process since it accounts for energy upscattering as well as downscattering. Furthermore, any of the neutron wave effects, referred to in Section 2.1, that are not accounted for by this model are assumed to be

insignificant for high mass ratio elements and are downscaled in the light elements by the use of experimentally measured and reported cross section data for water and polyethylene in the energy range below 2 eV where these aforementioned effects are observed.

The prompt gamma ray emission and attenuation are treated in detail. The questionable use of a prompt gamma production spectrum resulting from thermal neutron captures is not a serious limitation, since the epithermal to thermal ratio of the neutron fluxes in the core sample is low. These prompt gamma ray yields are used from the compilation of Lone *et al.* (1981).

The solid angle subtended by the detector at the collision point is determined exclusively for each point of collision where the prompt gamma ray of interest is forced to be emitted in the core sample material. The paths in various materials, traversed in the direction of flight of the emitted gamma ray and that have been forced to intercept the detector, are computed in detail, and the attenuation factors of the gamma ray are computed. The mass attenuation coefficients as a function of the gamma ray energy for these materials are obtained from the compilation of Storm and Israel (1970).

Experimentally determined values of the photopeak efficiency of the Ge(Li) detector were taken from Knoll (1979) and are shown graphically in Figure 5.9-1. It should be understood that it is assumed that the incident gamma ray is averaged from emissions (sources) uniformly distributed around the detector and not exclusive at the centerline axis of the detector.

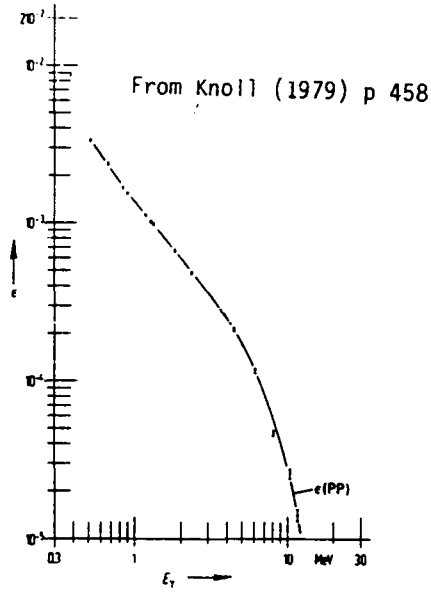

Figure 5.9-1 Absolute photopeak efficiency values for a Ge(Li) detector.

Variance reduction techniques are used to increase the likelihood that the history will contribute favorably to the desired result. The neutrons are forced to remain within the boundaries of the monitoring system and are not allowed to escape. The neutrons are forced to undergo a scattering interaction at each collision point throughout the simulation. The expected value technique is used exclusively in non-analog simulation to score the prompt gamma rays of interest in the detector using experimentally measured and reported values of detector efficiency to replace the Monte Carlo simulation of the gamma ray detection and transport inside the detector. Russian Roulette is used to decide the fate of the neutron when its absolute weight reaches the cutoff weight limit

without introducing biasing in the process.

Correlated sampling (Spanier and Gelbard, 1969) was used, where the histories generated for a reference elemental concentration of the core sample are used concurrently to generate the prompt gamma ray responses for all other elemental concentrations using well-defined physical principles. This effectively allows the generation of the calibration curve for gamma ray counting rates at various elemental concentrations for any element of interest in one execution of the Monte Carlo program with the stipulation that this curve is normalized at the reference elemental concentration.

6. MCNP MONTE CARLO CODE

The Monte Carlo Neutron and Photon Transport Code (MNCP) is a very general code developed at Los Alamos National Laboratory with approximately 250 person-years of collaborated efforts. It is used about 60 Cray hours per month by Los Alamos users. To say the least, it is the state-of-the-art Monte Carlo code.

In this chapter no attempts will be made to describe the code or its applicability to the solution of an ever increasing number of problems; rather, the voluminous MCNP manual (Briesmeister, 1986) should be consulted whenever a question arises about the code. This chapter is intended to investigate the capability of MNCP to handle discrete neutron-induced photon lines and to list the input parameters necessary to utilize this feature to obtain the photopeak response as a function of elemental concentrations in the sample. The photopeak responses are then compared with the responses obtained from the code (MCNCP) developed in this work.

6.1 Neutron-Induced Photon Production Data

MCNP has an optional mode (MODE:N P), in which, upon a neutron interaction in the medium, uncorrelated photons are sampled randomly (up to 10 per collision) to be emitted at that site. In fact, they are stored in data banks and are tracked throughout the medium after the neutron tracking has been accomplished. The energy distribution and the intensity of these emitted photons are sampled from tabulated distributions (32 equally probable cosine bins)

specifically processed from ENDF/B-V cross section data and tailored for MCNP. These photons are tracked in the medium, and the Detailed Physics or the optional Simple Physics treatment may be specified for the photons to undergo the simulated processes of Section 2.2.3. It is obvious that a photon tally accumulated at any position consists of direct contributions due to the photons arriving uncollided from the source, in addition to an associated spectrum due to scattering processes in between the source and the point under consideration. This feature is tailored to furnish dosimetry calculations when the full energy spectrum of photons is desired.

In this work, as referred to in Section 2.2.4, the net area under the photopeak (response) of interest is mainly due to the unscattered full energy contributions. The expected detector background in an experimental setup consists of contributions from scatterings in the vicinity of the detector as well as within the detector. Therefore, the background in a real situation is expected to be slightly higher. Thus, detailed tracking of the photons through the processes of Section 2.2.3 is a waste of computer time. Furthermore, the distribution sampled to generate the photons, although predominantly due to neutron captures, also is composed of photon production due to inelastic scattering and other contributions that might be significant.

MCNP version 3B has a unique option (PIKMT card) that enables the user to turn on selected "monoenergetic" photons resulting from neutron capture reactions in specific elements. Currently, only

partial data are available for some elements, and none is available for some. Nevertheless, this option was utilized to compare the results obtained from the computer code MCNCP (Monte Carlo Neutron Capture Photon Production Code) developed by the author with those obtained from MCNP.

6.2 Discrete Photon Lines

Whenever one is interested in a small subset of the entire photon energy spectrum (such as the discrete line spectrum resulting from neutron captures in an element of interest in this work), MCNP version 3B provides a biasing capability to bias the spectrum of neutron-induced (in the coupled neutron-photon mode) photons to produce only those that are of interest (PIKMT card). These photons could be produced at neutron collision sites from isotopes other than the isotope with which the neutron collided. This feature of biasing the photon productions is the first production version of collision biasing in MCNP.

The data for the discrete photon lines are generally from the ENDF/B-V evaluations and are available from Los Alamos National Laboratory, listed in file SIGRMCCS.

For the elements listed in Table 4.4-4 whose capture gamma rays are of interest, there exist no specified "signature photons" for Mg nor for Mn. Data for Ti, Cr, and Fe have no gamma ray lines due to neutron capture. Table 6.2-1 shows some of the tabulated data for Cl.

Element	Capture γ-ray Energy (MeV)	Identifier mt number
Cl	5.717	102010
	6.108	102007
	6.620	102005
	7.413	102003

Table 6.2-1 Discrete photon lines from neutron captures in Cl (SIGRMCCS listings)

6.3 Tallying Discrete Photon Lines

Tallying the gamma rays arriving at the location of the circular cylindrical detector was accomplished by specifying a DXTRAN sphere (a variance reduction technique in MCNP). The prompt gamma rays have only a small probability of being emitted in a direction so as to intersect the detector. To ameliorate this deficiency the DXTRAN concept was used to "force" the capture gamma rays toward the region occupied by the detector. The DXTRAN inner sphere has to enclose the entire detector volume. This technique deterministically forces the gamma rays to be emitted in the solid angle subtended by the DXTRAN outer sphere at the site of collision and deterministically transports the γ-rays, without collisions, to the surface of the DXTRAN sphere. The energy spectrum of a discrete gamma when emitted at the sample is not a discrete spectrum once inside the DXTRAN sphere. Rather it consists of discrete lines with a continuum background, as explained next. After forcing the emission and transmission of the "pseudo γ-rays" into the DXTRAN sphere, the physical gamma ray is treated and tracked in a normal

fashion and, if it happens that the tracked gamma ray reaches the DXTRAN sphere, then it is killed to balance the weight of the gamma rays that are forced toward the sphere. Once the "pseudo γ-ray" is at the DXTRAN sphere, the DXTRAN game of forcing the direction and the transport towards a desired region is stopped because the gamma ray is already in the desired region and because it is impossible to define the aforementioned solid angle.

The "pseudo γ-ray" at the surface of the sphere is treated as a "real γ-ray" tracked and transported in a random walk process. Therefore, it is expected that a monoenergetic gamma ray at the surface of the DXTRAN sphere will result in a spectrum due to gamma ray interaction mechanisms with the materials within the sphere. This energy spectrum is shown, for illustrative purposes, in Figures 6.3-1A and 6.3-1B. Inspection of the two figures clearly shows that the relative magnitudes of the peaks in the lowest chlorine concentration spectrum differ appreciably from the corresponding relative magnitudes among the peaks in the highest chlorine concentration spectrum. The deviation is mainly due to the fact that at high chlorine concentrations, the spatial and energy distribution of the neutron flux within the core sample are significantly different. The epithermal to thermal neutron flux ratios are different, resulting in the aforementioned yield difference (see Section 2.2.1) of the capture gamma ray emission. Furthermore, the magnitude of the corresponding peaks in both figures are not a factor of nine different in spite of the fact that the highest to lowest chlorine concentrations is a factor of nine.

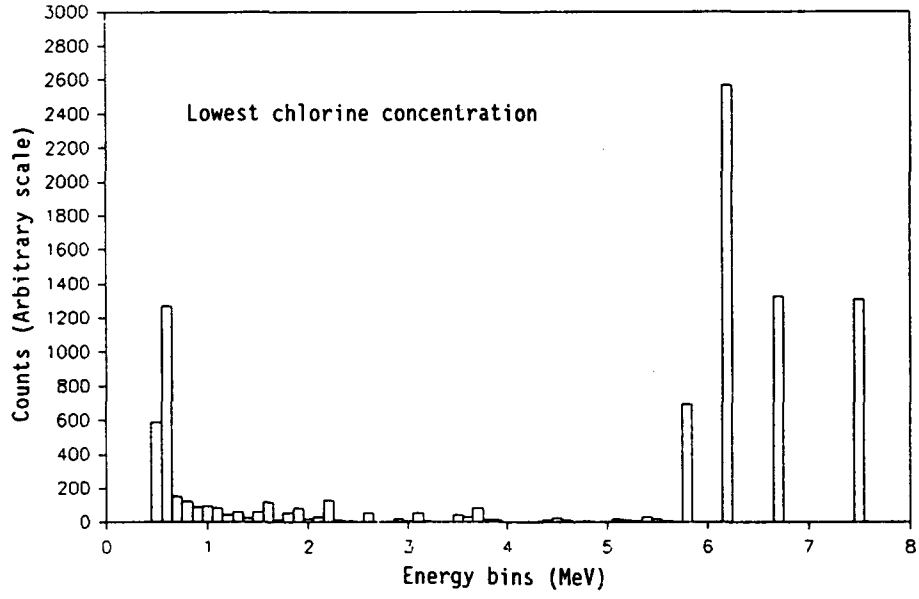

Figure 6.3-1A The energy spectrum, in the vicinity of the detector, of monoenergetic photons emitted at the sample (Lowest Chlorine Concentration)(MCNP).

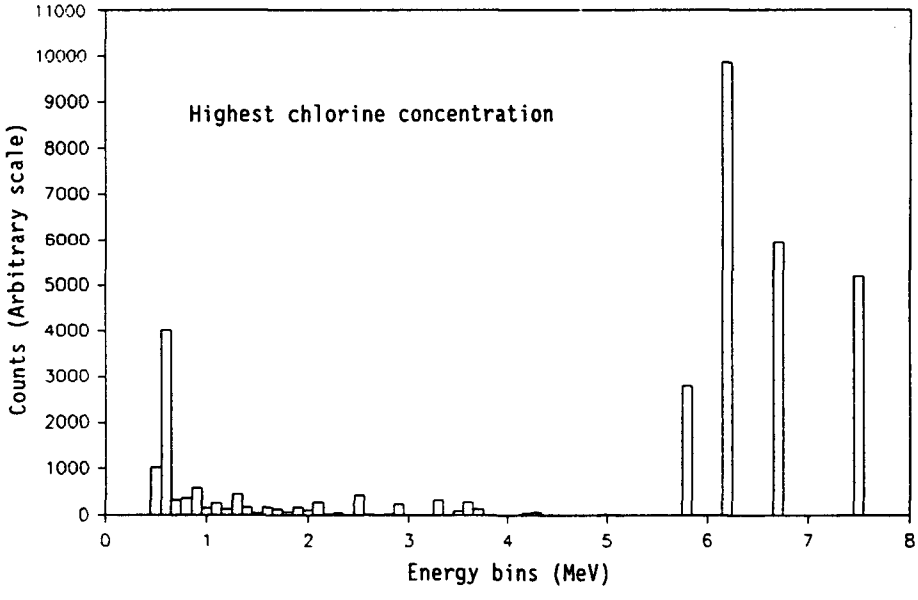

Figure 6.3-1B The energy spectrum, in the vicinity of the detector, of monoenergetic photons emitted at the sample (Highest Chlorine Concentration)(MCNP).

This non-linearity is further investigated in Chapter 7. The net counts under a desired peak is therefore deduced by subtracting out the background continuum. It should be mentioned that some of the discrete (capture) gamma ray data are "almost discrete" because the emitted gamma ray energies are given to be within $E \pm \delta$, where δ is less than 1% of the energy E. This should be kept in mind when deciding on tally energy bins. The relative strength (branching ratio) of individual discrete gamma rays should be used as a tally multiplier to determine the number of photons produced with that energy.

The simulation of a real physical detector (not a point detector) was accomplished by tallying the gamma ray current at the top, side, and bottom surfaces of a cylindrical geometry (detector) in order to determine the gamma ray current incident into the detector volume. The tally segment card and the cosine card were used to tally the gamma rays in the "positive" direction entering the bottom of the detector and in the "negative" direction entering the top of the detector. The tally energy card was used to single out the response of an energy bin around the photopeak energy. The detector full energy (photopeak) responses were estimated knowing the efficiency of the detector as a function of incident gamma ray energy (Figure 5.9-1) and the branching ratio of the discrete energy capture gamma ray. These branching ratios were not used in the PIKMT card; rather, the discrete gamma rays were sampled with equal probability to improve statistics. A listing of a sample input file for MCNP is given in Appendix I.

6.4 Correlated Sampling in MCNP

Of interest in this work is the variation of the photopeak responses due to variations in the elemental concentrations in the sample. The inherent statistical fluctuations of the Monte Carlo method makes it impossible to assess that a small perturbation in the elemental concentration of the sample is responsible for the observed variations in the photopeak responses unless appropriate means are taken for controlling the sequence of the random numbers, in both the perturbed and the unperturbed problem. If both problems were started with the same initial pseudorandom number (seed), and the same sequence of random numbers were used for each history, then it could be said that in subsequent histories only the perturbation in the elemental concentrations causes the sequence to diverge. MCNP always uses the same pseudorandom number in the first history of a problem (unless the user specifies otherwise via the debug information card DBCN). Also the increment of the random number in between histories is internally controlled. At the beginning of a new history the random number sequence is increased by 4297 random numbers from the beginning of the previous history regardless of how many random numbers were used in the previous history. This quantity was deemed not enough for the problem at hand (on the average, it takes about 7300 random numbers to simulate one neutron history). Therefore, the increment value should be increased to be at least 9000, by altering the source code in MCNP (Entry ADVIJK in subroutine RAND). The random number generator RAND seems to have a

constraint such that a formula that is not valid if the values of the variables within the formula exceed pre-specified values (the increment 4297 does not violate this condition).

7. RESULTS, COMPARISONS, AND DISCUSSIONS

The developed computer program MCNCP models the proposed monitoring system by the Monte Carlo procedures of Chapter 5.

To predict the detector photopeak responses as a function of elemental concentrations, an "average" core sample composition (see Table 4.4-3) was chosen as the reference (base) elemental concentrations. The mass of each element of interest (Mg, Cl, Ti, Cr, Mn, or Fe) was changed sequentially to cover an arbitrary range of interest, namely, 0.2, 0.4, 0.6, 0.8, 1.2, 1.4, 1.6, and 1.8 times the mass of that element in the reference elemental concentrations while the masses of the remaining constituents of the sample were kept invariant, although the density and the weight percent were adjusted accordingly (constant volume).

The relative responses, normalized to a value of unity at the reference elemental concentrations, of the changed element were calculated according to the correlated sampling procedure of Section 5.8. The outputs are given in tabular forms in Appendix H and are presented graphically in Figures 7-1 through 7-6.

Due to the lack of funds to construct an experimental setup to test and validate the predicted photopeak responses from MCNCP, testing the code was facilitated by comparing its predicted results with results obtained from the well-established MCNP code. As mentioned in Section 6.2, MCNP does not have a full set of data for discrete capture gamma rays for all the elements of interest in this work. Therefore, the comparison between the results obtained from

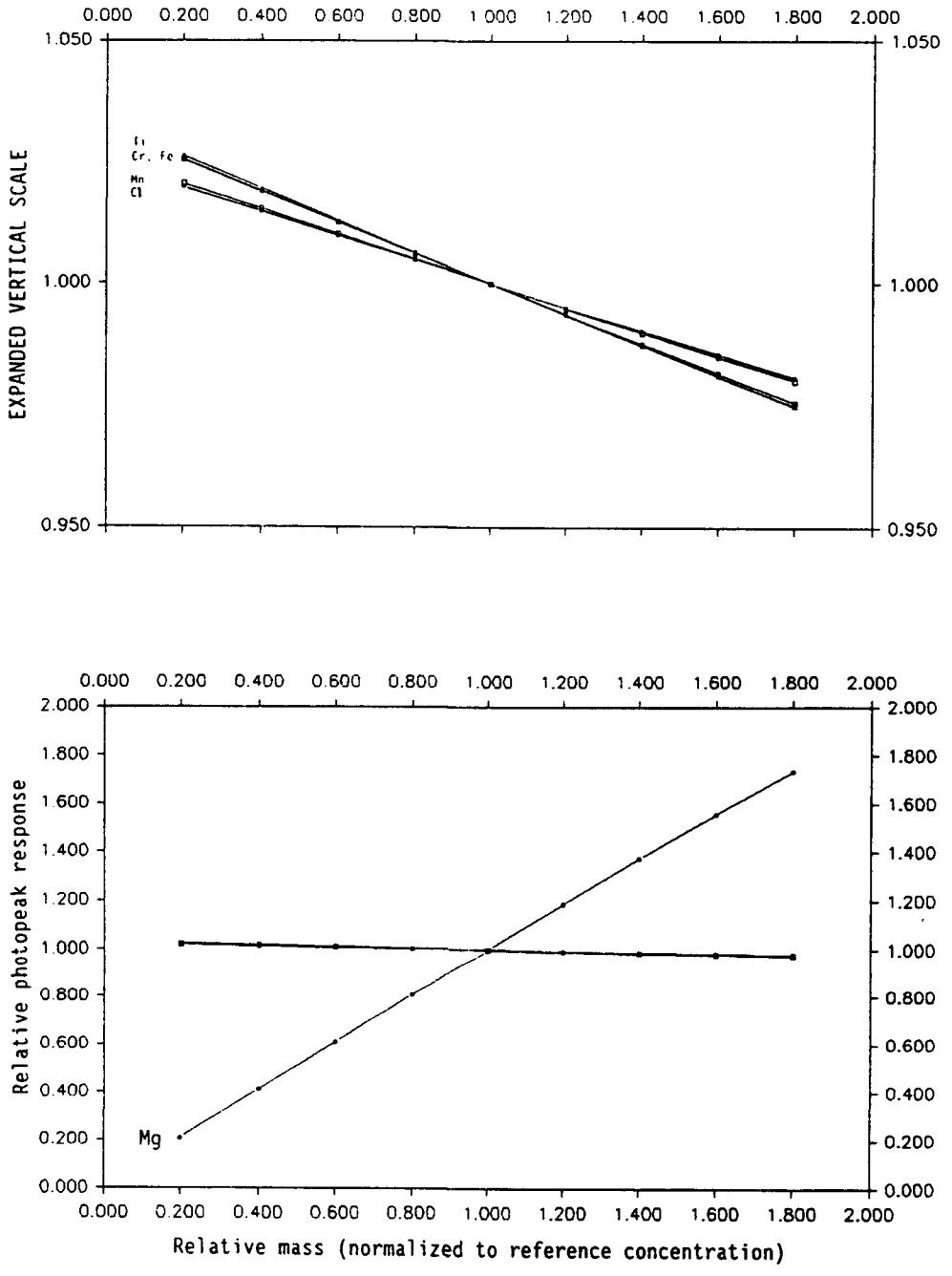

Figure 7-1 The relative variation of the photopeak response as a function of elemental concentrations of magnesium in the "seafloor core sample"

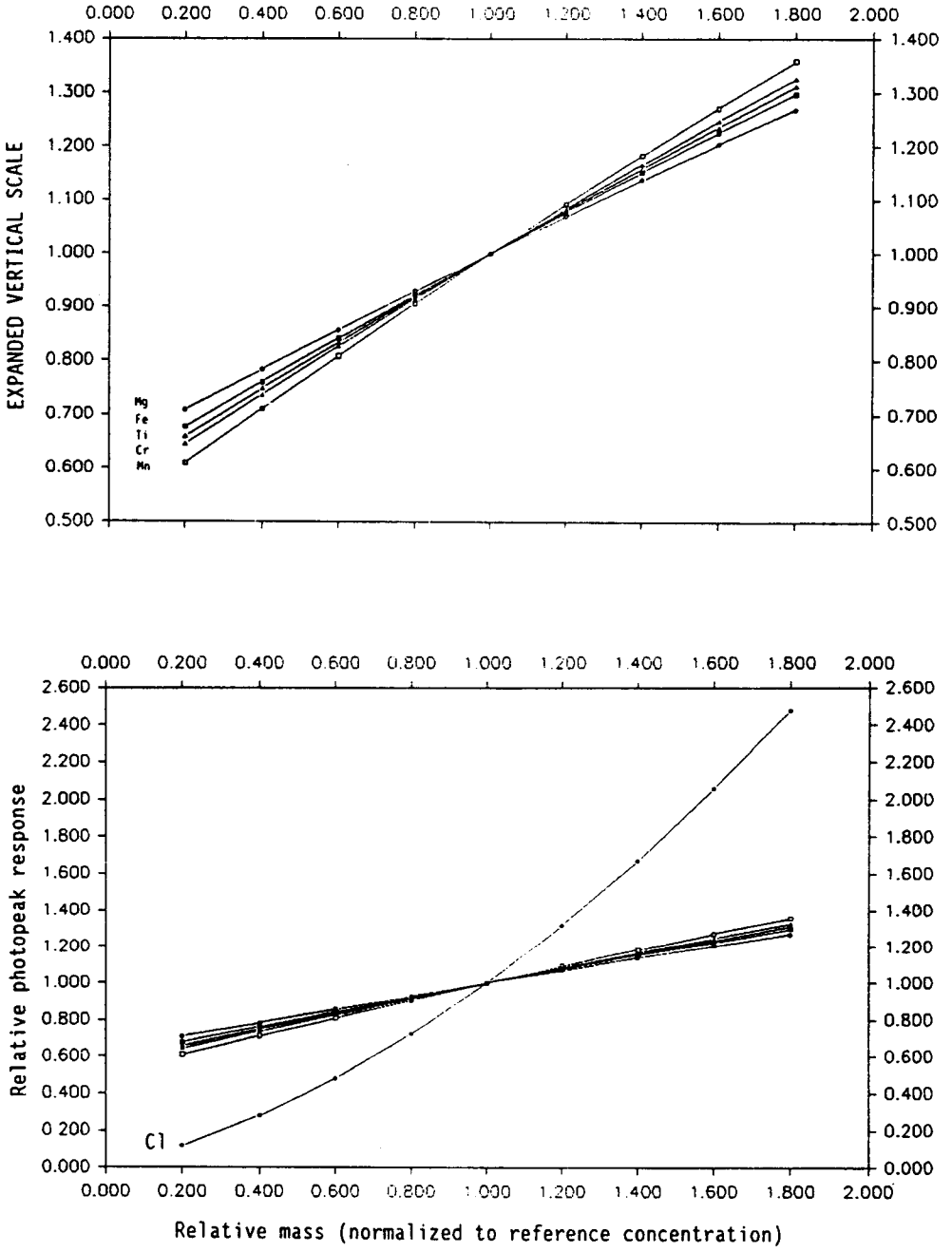

Figure 7-2 The relative variation of the photopeak response as a function of elemental concentrations of chlorine in the "seafloor core sample"

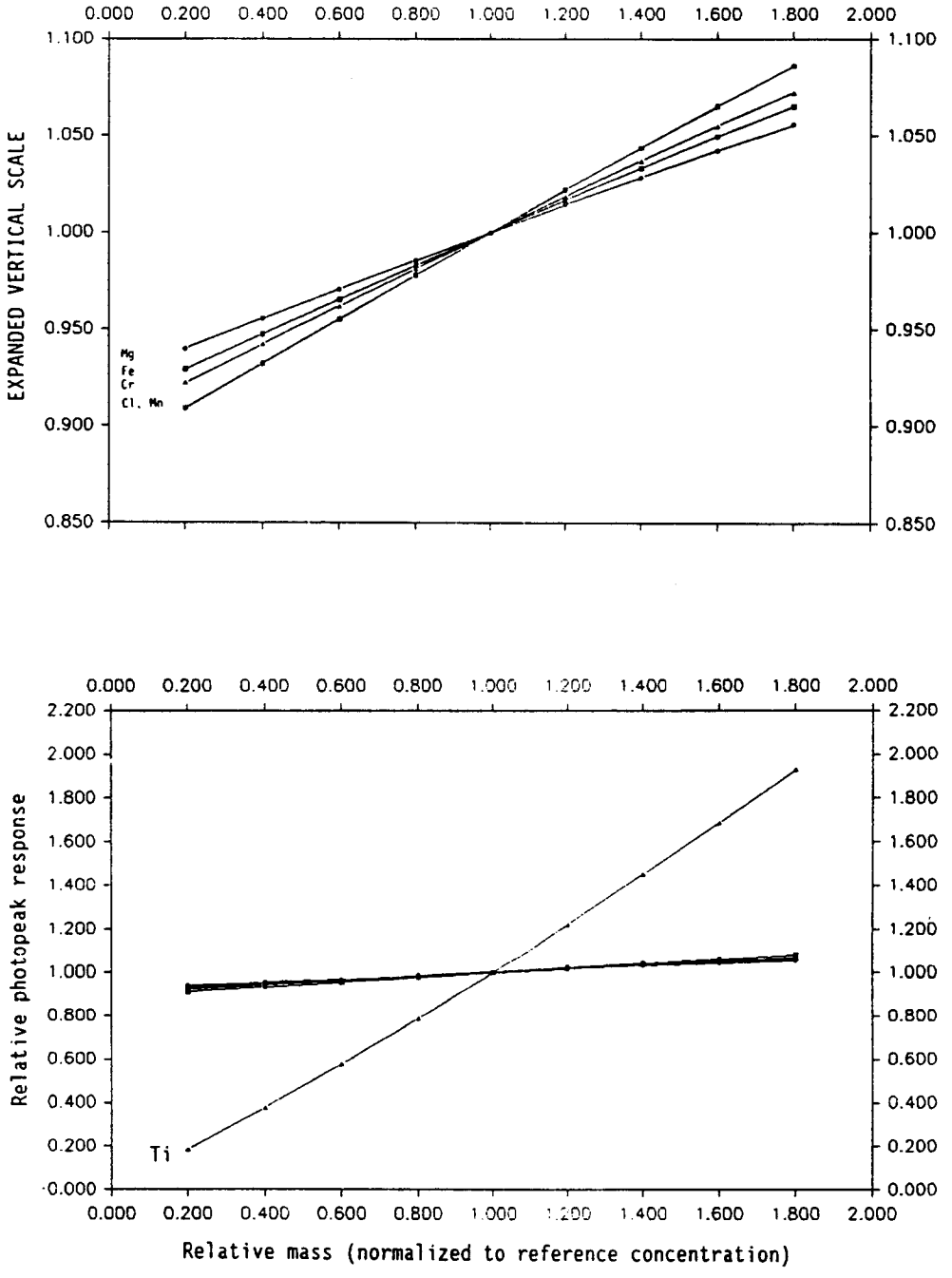

Figure 7-3 The relative variation of the photopeak response as a function of elemental concentrations of titanium in the "seafloor core sample"

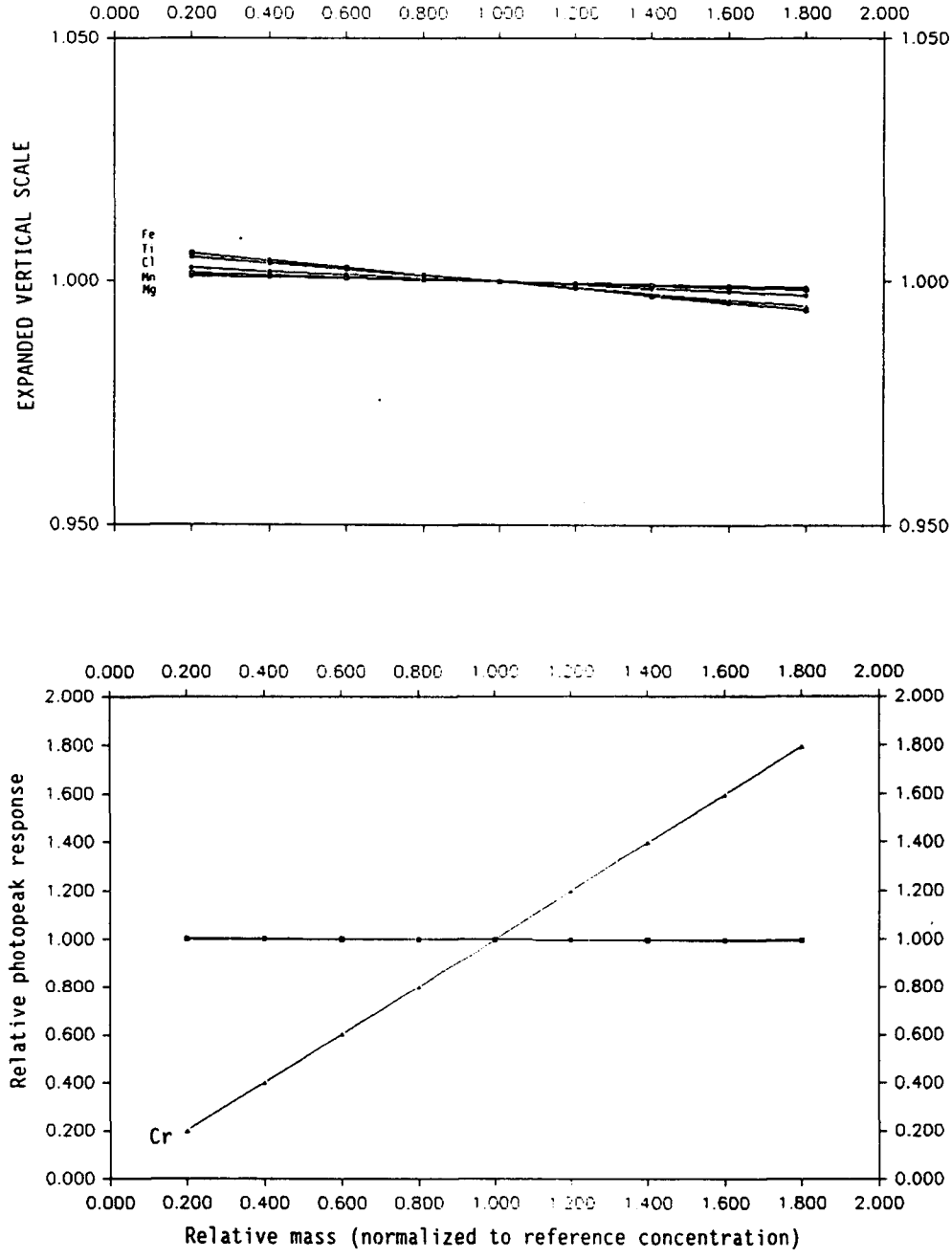

Figure 7-4 The relative variation of the photopeak response as a function of elemental concentrations of chromium in the "seafloor core sample"

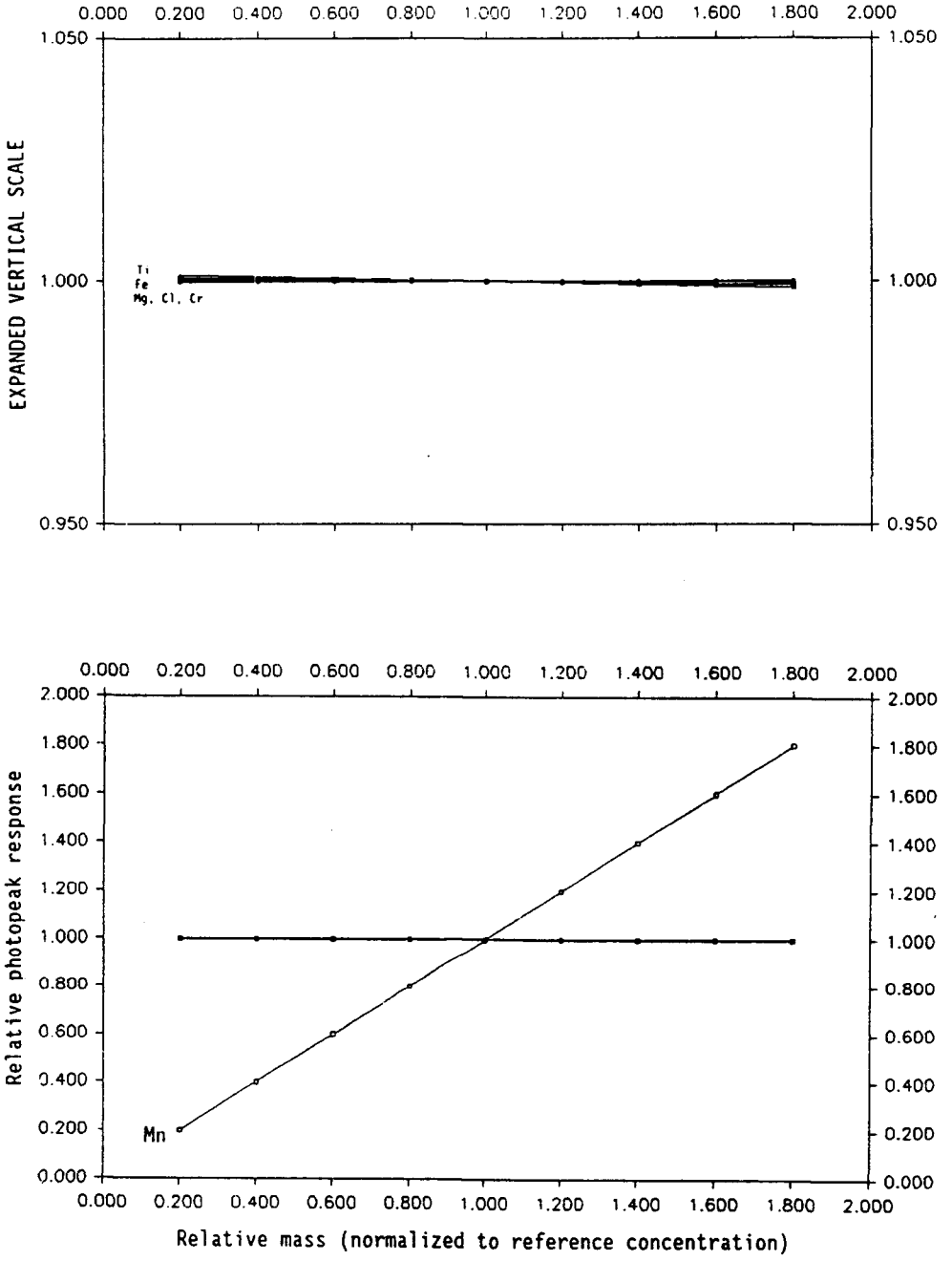

Figure 7-5 The relative variation of the photopeak response as a function of elemental concentrations of manganese in the "seafloor core sample"

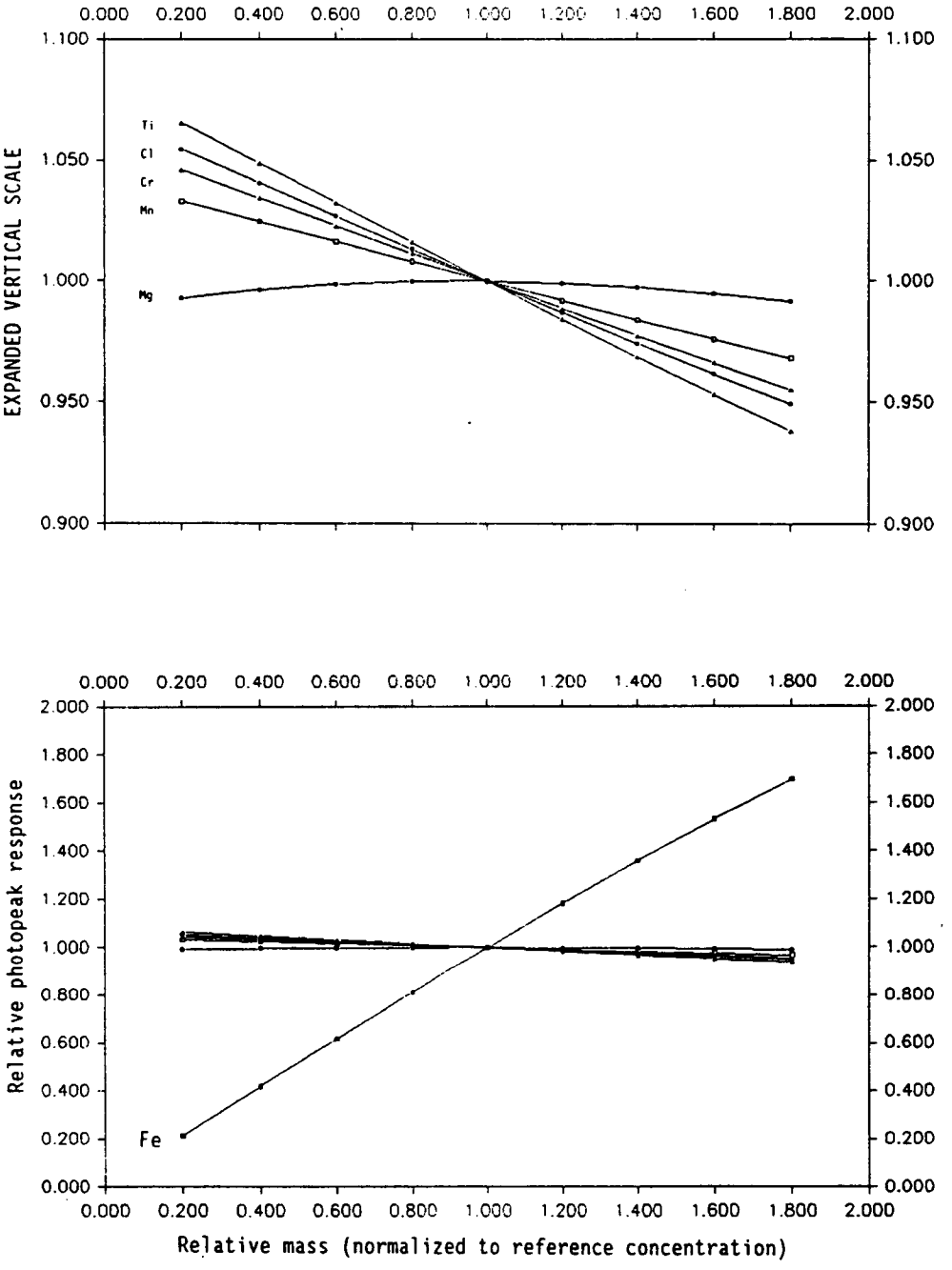

Figure 7-6 The relative variation of the photopeak response as a function of elemental concentrations of iron in the "seafloor core sample"

MCNCP and the results from MCNP was based on comparing four discrete capture gamma lines available from neutron captures in Cl, namely 5.7153, 6.1109, 6.6195, and 7.4138 MeV. The chlorine mass was changed sequentially to cover the same range of interest in both MCNP and MCNCP. The masses of the elements exclusive of chlorine were kept invariant but the weight percentages were adjusted appropriately. Tables 7-1 and 7-2 summarize the pertinent data obtained from MCNP. To simulate the same range of variation in the Cl concentration, nine different computer runs are necessary with MCNP with appropriate values of the weight percentage of the various elements in the core sample, in contrast to a single correlated run with MCNCP.

Element	Capture γ-ray Energy (MeV)	Absolute response per source neutron
Cl	5.717	3.1199×10^{-11}
	6.11	4.9960×10^{-10}
	6.619	1.2405×10^{-10}
	7.414	5.8106×10^{-11}

Based on the branching ratios from SIGRMCCS and the estimated detector photopeak efficiency at the reference elemental concentrations.

Table 7-1 The absolute photopeak responses for chlorine at the reference elemental concentrations, obtained from MCNP.

Elemental concentration number	Cl Neutron capture γ-ray photopeak response			
	5.715 MeV	6.11 MeV	6.619 MeV	7.414 MeV
1	0.3362	0.2988	0.2603	0.2851
2	0.5125	0.5290	0.5116	0.5272
3	0.7064	0.7323	0.6918	0.6552
4	0.8972	0.8461	0.7126	0.7769
5	1.0	1.0	1.0	1.0
6	1.4788	1.2808	1.2759	1.3018
7	0.9486	1.0005	1.1180	1.0572
8	1.4146	1.4163	1.2776	1.2044
9	1.3529	1.1413	1.1548	1.1492

The responses are normalized to the reference elemental concentrations (5)

Table 7-2 The relative photopeak responses for chlorine at different concentrations in the core sample (MCNP).

Reference to Figures 7-1 through 7-6 shows, in general, that the photopeak responses increase with increasing concentrations of the element of interest. The non-linear relationship is pronounced in trace elements with significantly large neutron absorption cross sections (e.g., Cl; σ_a = 33.5 b, the resonance integral I_γ = 13.7 b), especially when present in larger concentrations. The general observable trend is that when the photopeak response variation with concentration is almost linear (Cr and Mn), the variation of the response of the remaining elements of interest in the sample is almost nil or just slightly decreasing. On the other hand, when the photopeak response of the varied element increases but is charaterized by a negative curvature with respect to the x-axis (Mg and Fe), the decrease in the response of the remaining elements is

more enhanced. The variations of Cl and Ti result in an increasing photopeak response with a positive curvature with respect to the x-axis and the response for the remaining elements increases noticeably. The photopeak responses from the remaining elements of interest in the sample were expected to decrease slightly due to the competition for neutron absorption in favor of the element that has been increased in mass. To further investigate this behavior and to carry out the intended comparison with results obtained from MCNP, the monitoring system was simulated using MCNP (the nuclear cross section data used in the developed MCNCP code were extracted from the same data used in MCNP). The results, given in Table 7-2 and represented graphically in Figure 7-7, when compared with Figure 7-2 show significant deviations at the higher concentrations of chlorine. Nevertheless, the lower concentrations show close agreement (same trend of relationship between the relative photopeak responses and the elemental concentrations) between the results from MCNCP and MCNP, as shown in Figure 7-8.

MCNCP is "insensitive" to the neutron absorptions with energies above thermal energies and treats such neutron absorptions (as far as photon production is concerned) as thermal absorptions. Hence the resulting capture gamma ray spectrum and intensities presumably have the same spectrum and yields as for thermal absorption. This was explained in Section 2.2.1, and the last paragraph cautioned that serious errors might result from this assumption.

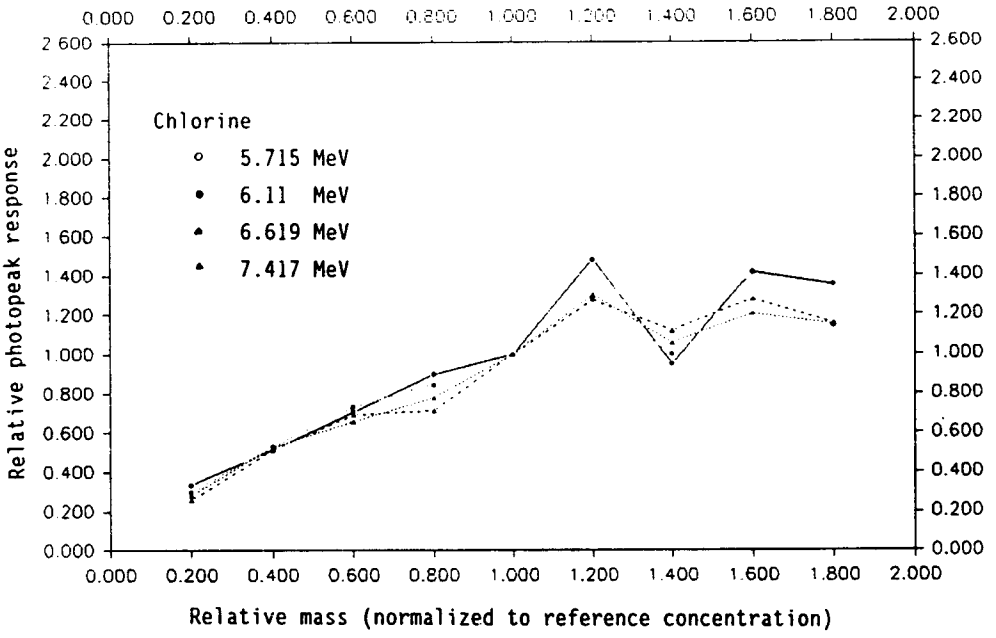

Figure 7-7 The relative variation of the photopeak response as a function of elemental concentrations of chlorine in the "seafloor core sample" (MCNP)

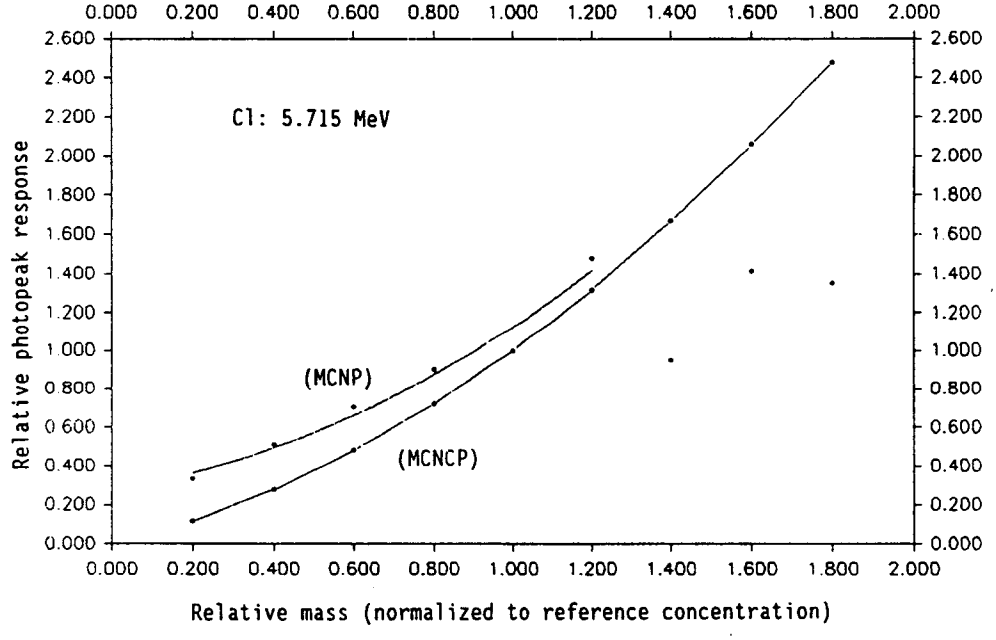

Figure 7-8 The relative variation of the photopeak response at 5.715 MeV as a function of elemental concentrations of chlorine in the "seafloor core sample" with the lower concentrations having been fit by a second order curve.

It was decided to investigate the neutron absorptions in the sample having energies above thermal by assessing the magnitude of the epithermal neutron flux relative to the thermal neutron flux within the core sample.

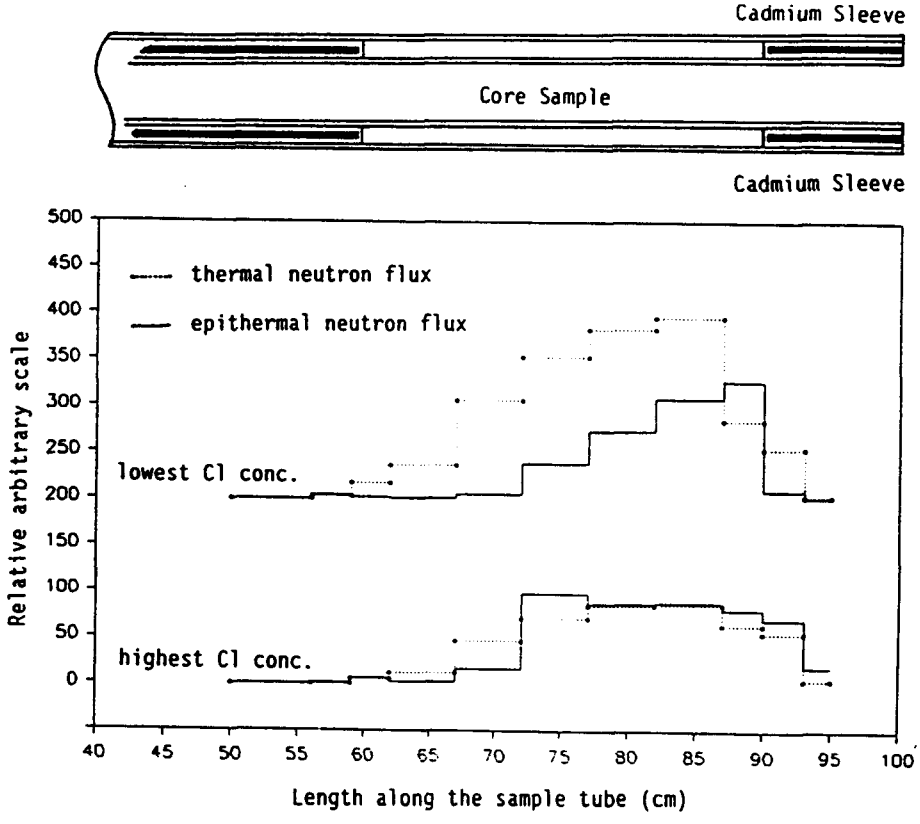

Figure 7-9 The average neutron flux within the core sample, obtained from MCNP.

Results from MCNP for the thermal neutron flux (< 2 eV) and the epithermal neutron flux (> 2 eV), averaged over sections of the core sample, are shown graphically in Figure 7-9. The neutron flux

at the lowest (0.2) and highest (1.8) relative chlorine concentrations in the core sample imply that the ratio of the thermal to the epithermal neutron flux is in excess of 1.5 for the lowest chlorine concentrations. At the highest concentration of chlorine, the epithermal neutron flux is roughly equal in magnitude to that of the thermal neutron flux. In fact, this behavior was observed at as low a relative chlorine concentration as 1.2, where the functional relationship between the photopeak response and the elemental concentration deteriorated as shown in Figure 7-7. Therefore, the deterioration in the relationship between the photopeak response and the elemental concentration can be explained as follows. The presence of the core sample perturbs the spatial and energy distribution of the neutrons. The neutron flux within the core sample is in turn the result of a balance between thermalizing effects and absorption by the various elements present (especially by those elements with high capture cross sections). Since the capture gamma ray production and its relative intensities are functions of the captured neutron energy, the harder epithermal neutron spectrum enhances the epithermal resonance absorptions, which have different relative intensities of capture gamma rays than those following absorptions of thermal neutrons. In fact this behavior is observable in the prompt gamma ray spectra of Figures 6.3-1A and 6.3-1B.

Allowances for these effects should be made in the design of the monitoring system and in the method of data utilization.

The variation of elemental concentrations, in principle, in

the sample can be deduced from the model given the photopeak response.

Finally, because of the exploratory nature of this work, low levels of precision were tolerated in the Monte Carlo runs. The results were deemed sufficiently accurate to indicate whether a practical experimental model is feasible and whether any improvements in the calculational efficiency or procedures should be expended.

8. SUMMARY AND RECOMMENDATIONS FOR FOLLOWUP STUDIES

A computer code was developed specifically to simulate the proposed monitoring system based on the neutron capture prompt gamma ray analysis (NCPGA) technique to predict the variations of the detector responses as a function of elemental concentrations of some elements of interest in the seafloor core sample by the Monte Carlo method. The code is refered to as MCNCP (Monte Carlo Neutron Capture Photon Production).

The neutron emission from the Cf-252 neutron source and its transport through the various media were treated in a detailed continuous energy variable. The emission and transmission (toward the detector) of capture gamma rays was treated deterministically. Various built-in variance reduction techniques in MCNCP were employed to make the computational task more economical and efficient.

It has been shown that the Monte Carlo method is conceptually simple even when irregular complicated boundaries and geometries exist. However, the logical decisions to cover every conceivable event make the programming difficult to construct and debug.

The model and the code have been developed to have the capability of handling arbitrary dimensions and relative positions between the sample tube, the detector tube, and the neutron source tube; thus lending MCNCP to suit the exploratory nature for optimization of system design. The optimization, in principle, could be investigated by increasing a parameter (e.g., the

hydrogeneous moderator between the neutron source and the sample) that results in an increase in the thermal neutron flux, especially in the vicinity of the neutron source. This increase is expected to enhance capture gamma ray production, but the same change will decrease the chance that the thermalized neutrons will reach the sample. Instead they diffuse thermally and wander in the moderator. Such counteracting processes, under the right conditions (e.g., proper geometry), may cancel in full or partially to render the signal (the photopeak response) nearly independent of the other parameters exclusive of the elemental concentrations of the sample. Therefore, a good system design and optimization would make the expression in the parentheses in Equation (5.5-10) a constant independent of the parameters that are difficult to control and of the composition of the other elements within the sample, if possible. This constant is then determined during calibration. To determine the relation between the counts under the photopeak and the elemental concentration, a sample for which the elemental concentrations are known from some other type of assay (e.g., chemical analysis) and which is fairly representitive of the expected samples that might be encountered in the field has to be used for calibration. This calibration may be invalidated if the system, when in use, encounters a sample having different neutron and gamma ray transport characteristics than that used in the calibration.

MCNCP is useful in reducing the expended time and costs by providing interpolation of results and by predicting conditions

which may be practically difficult to simulate experimentally. For example, it might be advantageous to use multiple distributed neutron sources around the sample. The code has been exclusively tested as individual subroutines and as an integrated unit. But it is conceivable that during the process of parameter and relative positioning changes, a difficulty might arise (built in error or warning messages help locate the source of the difficulty). It will be appreciated to bring any encountered difficulties or suggestions to the attention of Dr. S. E. Binney (Dept. of Nuclear Engineering, Oregon State University).

No "serious" attempts were made to make the code run fast and efficient, although the author feels that the following improvements may prove worthwhile to investigate.

The detailed continuous energy treatment of the neutron energy and the cross section data is time and storage consuming. If it can be shown that the desired results (responses) are not significantly affected when coarse group averaged data are employed, appreciable saving in computer space and time might be achieved. Further savings might be investigated by applying the probability table method to handle the voluminous cross section data (Cullen, 1974; Levitt, 1972).

Calculating the probability of capture gamma ray emission into the solid angle subtended by the detector at the point of emission at each interaction site within the core sample and the calculations of individual path lengths traversed by the emitted gamma rays in various materials are very time consuming. If the fractional solid

angle calculations can be simplified, e.g., by using the idea of a DXTRAN sphere or the effective target volume "geometrical efficiency" (Van Otten *et al.*, 1988) and if the path of the gamma rays travelling from a point within the sample to the detector can be computed from a distance vector at the center of the "volumetric effective solid angle" (might be feasible for small enough detectors), then a tremendous time saving can be achieved. The same approach, which might be an effective variance reduction technique, could be used to deterministically scatter neutrons, transporting them within the monitoring system toward the sample without a great sacrifice to the efficiency of the calculations.

It should not be difficult to incorporate a subroutine within MCNCP to calculate and provide information about the position (depth) of the neutron capture and gamma ray emission. This is useful to calculate the effective depth of neutron penetration within the core sample and the subsequent attenuation of emitted capture gamma rays within the sample (the attenuation of high energy gamma rays might be insignificant). In fact this depth already has been calculated in subroutine DSAMPTX by calculating the path length traversed between the point of emission and the outer surface of the sample tube for individual gamma rays.

BIBLIOGRAPHY

Anderson, D.L., W.H. Zoller, G.E. Gordon, and W.B. Walters, " Neutron-capture prompt gamma-ray spectrometry as a quantitative analytical method," Inst. Phys. Cong. Ser. No.62, pp. 655-667 (1982).

Armstrong, S.B., "The Energy-Dependent Total Neutron Cross Section of Polyethylene," Nucl. Sci. Eng. 23: pp. 192-194 (1965).

Bell, G.I. and S. Glasstone, Nuclear Reactor Theory, Robert E. Krieger Publishing Co., Malabar, Florida (1982).

Bevington, P.R., Data Reduction and Error Analysis for the Physical Sciences, Mc Graw-Hill Book Company, New York (1969).

Bischoff, F.G., M.L. Yeater, and W.E. Moore, "Monte Carlo Evaluation of Multiple Scattering and Resolution Effects in Double-Differential Neutron Scattering Cross-Section Measurements," Nuc. Sci. Eng. 48: pp. 266-280 (1972).

Boldeman, J.W., D. Culley, and R.J. Cawley, "The Fission Neutron Spectrum from the Spontaneous Fission of ^{252}Cf," Trans. Am. Nucl. Soc. 32, 733 (1979).

Booth, T.E., "A Sample Problem for Variance Reduction in MCNP," Los Alamos National Laboratory report LA-10363-MS (June 1985).

Briesmeister, J.F. (Editor), "MCNP-A General Monte Carlo Code for Neutron and Photon Transport, Version 3A," LA-7396-M, Rev.2 (September 1986).

Carter, L.L. and E.D. Cashwell, Particle-Transport Simulation with the Monte Carlo Method, ERDA Critical Review Series TID-26607, Los Alamos Scientific Laboratory (1975).

Cashwell, E.D. and C.J. Everett, A Practical Manual on the Monte Carlo Method for Random Walk Problems, Pergamon Press, Inc., New York (1959).

Cember, H., Introduction to Health Physics, Pergamon Press, Oxford (1978).

Charbucinski, J., S.F. Youl, P.L. Eisler, and M. Borsaru, "Prompt neutron-gamma logging for coal ash in water-filled boreholes," Geophysics, 51: pp. 1110-1118 (1986).

Clark, T.C., R.P. Gardner, and K. Verghese, "A Monte Carlo Model for In-Situ Prompt Gamma-Ray Analysis Probes," Nucl. Instr. Meth. 193: pp. 365-370 (1982).

Clayton, C.G., "Neutron applications in the applied earth sciences," The Neutron and its Applications 1982, Inst. Phys., Bristol, Conf. Ser. No.64, pp. 451-456 (1983).

Clayton, C.G., A.M. Hassan, and M.R. Wormald, "Multi-element Analysis of Coal During Borehole Logging by Measurements of Prompt γ-Rays from Thermal Neutron Capture," Int. J. Appl. Radiat. Isot. 34: No.1, pp. 83-93 (1983).

Cullen, D.E., "Application of the Probability Table Method to Multigroup Calculations of Neutron Transport," Nuc. Sci. Eng. 55: pp. 387-400 (1974).

Doster, J.M., M. Lee, and R.P. Gardner, "Computational Model for Prompt Gamma-ray Analysis," Trans. Am. Nucl. Soc. 32: pp. 214-215. (1979).

Duderstadt, J.J. and L.J. Hamilton, Nuclear Reactor Analysis, John Wiley and Sons, Inc., New York (1976).

Duderstadt, J.J. and W.R. Martin, Transport Theory, John Wiley and Sons, Inc., New York (1979).

Duffey, D.A., A. El-Kady, and F.E. Senftle, "Analytical Sensitivities and Energies of Thermal Neutron Capture Gamma Rays," Nucl. Instr. Methods, 80, pp. 149-171 (1970).

Duffey, D. and P. Wiggins, "Equipment Designs for Neutron Capture Gamma Experiments with Cf-252," 1978 Proc. 3rd Int. Symp. Neutron Capture Gamma-Ray Spectroscopy and Related Topics (Brookhaven) pp 606-608 (1978).

Elias, E. and T. Gozani, "Nuclear Assay of Coal-volume 2, Coal Composition Determination by Prompt Neutron Activation Analysis-Theoretical Modeling," EPRI CS-989 (1980).

Evans, R.D., The Atomic Nucleus, Mc Graw-Hill Inc., New York (1972).

Everett, C.J. and E.D. Cashwell, "A Monte Carlo Sampler," Los Alamos Scientific Laboratory report LA-5061-MS, New Mexico (1972).

Failey, M.P., D.L. Anderson, W.H. Zoller, and G.E. Gordon, "Neutron-Capture Prompt γ-Ray Activation Analysis for Multielement Determination in Complex Samples," Anal. Chem. 51: No. 13, pp. 2209-2221 (1979).

Foderaro, A., The Elements of Neutron Interaction Theory, The MIT Press, Cambridge, Massachusetts (1971).

Foster, R.A., and T.N.K. Godfrey, "MCNP-A General Monte Carlo Code for Neutron and Photon Transport," in Monte-Carlo Methods and Applications in Neutronics, Photonics and Statistical Physics, Proceedings, Cadarache Casle, France, pp. 33-55, Lecture Notes in Physics, Springer-Verlag (1985).

Gamma, X-Ray and Neutron Techniques for the Coal Industry, Proceedings of an Advisory Group Meeting on Gamma, X-Ray and Neutron Techniques for the Coal Industry/ Organized by the Int. Atomic Energy Agency and held in Vienna, 4-7 December 1984, IAEA, Vienna (1986).

Gardner, R.P., H.K. Choi, M. Mickael, A.M. Yacout, Y. Jin, and K. Verghese, "Algorithms for Forcing Scattering Radiation to Spherical, Planar Circular, and Right Circular Cylindrical Detectors for Monte Carlo Simulation," Nucl. Sci. Eng., :95, pp. 245-256 (1987).

Garrett, C.W., W.E. Selph, P.N. Stevens, and H.C. Claiborne, "Interactions of Radiation with Matter," in Reactor Shielding for Nuclear Engineers, N.M Schaeffer (Ed.), U.S. Atomic Energy Commission, TID-25951 (1973).

Glascock, M.D., "Practical Applications of Neutron-Capture Reactions and Prompt Gamma Rays," Inst. Phys. Conf. Ser. No.62, pp. 641-654 (1982).

Gozani, T., "Physics of Recent Applications of PGNAA for On-line Analysis of Bulk Materials," in Capture Gamma-Ray Spectroscopy and Related Topics-1984, Int. Symp., Knoxville, Tenn., S. Raman (Ed.), pp. 828-846, Am. Inst of Physics, Conf. Proc. No.125 (1985).

Grau, J.A., A.S. Antkiw, R.C. Hertzog, R.A. Manente, and J.S. Schweitzer, "In Situ Neutron Capture Spectroscopy of Geological Formations," in Capture Gamma-Ray Spectroscopy and Related Topics-1984, Int. Symp., Knoxville, Tenn., S. Raman (Ed.), pp. 828-846, Am. Inst of Physics, Conf. Proc. No.125 (1985).

Green, L., J.A. Mitchell, and N.M. Steen, "The Californium-252 Fission Neutron Spectrum from 0.5 to 13 MeV," Nucl. Sci. Eng. 50: pp. 257-272 (1973).

Greenwood, R.C., "Practical Applications of Neutron Capture Gamma Rays," in Neutron Capture Gamma-Ray Spectroscopy, ed. R.E. Chrien and W.R. Kane, pp. 441-459, Plenum Press, New York (1978).

"Guide For Fabricating and Handling Cf-252 Sources," U.S. Atomic Energy Commission, NTIS-SRO-153, Aiken, South Carolina (January 1971).

Hendrick, J.S., and T.E. Booth, "MCNP Variance Reduction Overview," in Monte-Carlo Methods and Applications in Neutronics, Photonics and Statistical Physics, Proceedings, Cadarache Casle, France, pp. 83-92, Lecture Notes in Physics, Springer-Verlag (1985).

Henklemann, R., "The Role of Neutron-Capture Gamma-Rays in Element Analysis," in Neutron Capture Gamma-Ray Spectroscopy, ed. R.E. Chrien and W.R. Kane, pp. 624-625, Plenum Press, New York (1978).

Henry, A.F., Nuclear-Reactor Analysis, The MIT Press, Cambridge, Massachusetts (1975).

Isenhour, T.L. and G.H. Morrison, "Modulation Techniques for Neutron Capture Gamma Measurements in Activation Analysis," Anal. Chem. 38: pp. 162-167 (1966).

Jurney, E.T., "Application of the Thermal (n,γ) Reaction to Elemental Analysis," in Neutron Capture Gamma-Ray Spectroscopy and Related Topics, Proc. 3rd Int. Symp. (Brookhaven), pp. 461-474 (1978).

Kalos, M.H. and P.A. Whitlock, Monte Carlo Method, Vol. I, John Wiley and Sons, Inc., New York (1986).

Kalos, M.H., F.R. Nakache, and J. Celnik, "Monte Carlo Methods in Reactor Computations," in Computing Methods in Reactor Physics, H. Greenspan, C.N. Kelber, and D. Okrent, Eds., p 365, Gordon and Breach Science Publishers, New York (1968).

Kinsey, R., (Revised by), "Data Formats and Procedures for the Evaluated Nuclear Data File, ENDF," Brookhaven National Laboratory report, BNL-NCS-50496 (ENDF-102), 2nd Edition (ENDF/B-V) (1979).

Knoll, G.F., Radiation Detection and Measurements, John Wiley and Sons, Inc., New York (1979).

Koppel, J.U., and J.A. Young, "Neutron Scattering by Polyethylene," Nucl. Sci. Eng., 21, pp. 268-270 (1965).

Kraner, H.W., R.H. Pehl, E.E. Haller, "Fast Neutron Radiation Damage of High Purity Germanium Detectors," IEEE No-22, 1, pp. 149-159 (1975).

Lamarsh, J.R., Introduction to Nuclear Reactor Theory, Addison-Wesley Publishing Co., Inc., Reading, Massachusetts (1972).

Levitt, L.B., "The Probability Table Method for Treating Unresolved Neutron Resonances in Monte Carlo Calculations," Nucl. Sci. Eng. 49: pp. 450-457 (1972).

Lewis, E.E., and W.F. Miller, Jr., Computational Methods of Neutron Transport, John Wiley and Sons, Inc., New York (1984).

Lindstorm, R.M., and D.L. Anderson, "Analytical Neutron-Capture Gamma-ray Spectroscopy: Status and Prospects," in Capture Gamma-Ray Spectroscopy and Related Topics-1984, Int. Symp., Knoxville, Tenn., pp. 810-819, Am. Inst of Physics, Conf. Proc. No.125 (1985).

Little, R.C., and R.E. Seamon, "Nuclear Data for MCNP," in Monte-Carlo Methods and Applications in Neutronics, Photonics and Statistical Physics, Proceedings, Cadarache Casle, France, pp. 13-25, Lecture Notes in Physics, Springer-Verlag (1985).

Lone, M.A., R.A. Leavitt, and D.A. Harrison, Prompt Gamma Rays from Thermal-Neutron Capture, Atomic Data and Nuclear Data Tables 26: pp. 511-559 (1981).

Lukander, T. and S. Uusitalo, "On-line Neutron Capture Gamma Analysis with a Ge Detector," in Neutron Capture Gamma Ray Spectroscopy, R.E. Chrien and W.R. Kane (Eds.), Plenum Press, New York (1978).

Mickael, M., R.P Gardner, and K. Verghese, "An Improved Method for Estimating Particle Scattering Probabilities to Finite Detectors for Monte Carlo Simulation," Nucl. Sci. Eng. 99: pp. 251-266 (1988).

Moxham, R.M., A.B. Tanner, and F.E. Senftle, "In Situ Neutron Activation Analysis of Bottom Sediments, Anacostia River, Washington, D.C.," MTS Journal v. 11, No. 1, pp 14-20 (1976).

Nakamura, S., Computational Methods in Engineering and Science with Applications to Fluid Dynamics and Nuclear Systems, Robert K. Krieger Pub. Co., Malabar, Florida (1986).

Nargolwalla, S.S., A. Rehman, B. St. John-Smith, O. Legrady, and J. Strever, "Neutron Activation Borehole Logging of Geological Materials," Annual Progr. Rep. (15 December 1972 - 15 December 1973), Scintrex Ltd., Concord, Ontario (1973).

Nichols, J.P., "Design Data for ^{252}Cf Neutron Source Experiments," Nucl. Appl., 4, 382 (1968).

Noakes, J.E. and J.L. Harding, "New Techniques in Seafloor Mineral Exploration," Marine Technology V. 5 No. 6, pp. 41-44 (1971).

Noakes, J.E., and J.L. Harding, "Nuclear Techniques for Seafloor Mineral Exploration," Oceanology International Exhibition and Conference, Brighton, paper 0182 1.3 (1982).

Perkins, R.W., W.A. Haller, H.G. Rieck, L.A. Rancitelli, and N.A. Wogman, "Cf-252 Neutron Activation for Remote Surface Analysis," Isot. Rad. Tech., 9: No. 3, pp. 264-267 (1972).

Peterson, C.D. and S.E. Binney, "Compositional Variations of Coastal Placers in the Pacific Northwest, USA," Marine Mining, 7: pp. 397-416 (1988).

Press, W.H., B.P. Flannery, S.A. Teukolsky, and W.T. Vetterling, Numerical Recipes The Art of Scientific Computing, Cambridge University Press, New York (1988).

Profio, A.E., Radiation Shielding and Dosimetry, John Wiley and Sons, Inc., New York (1979).

Rainbow, M.T., "Monte Carlo Simulation of an Iron Ore Analyser," Int. J. Appl. Radiat. Isot. 36: No. 11, pp. 889-892 (1985).

Reynolds, G.M., T. Maung, V.J. Orphan, T. Gozani, E. Elias, and H. Bozorgmanesh, "System Optimization for Prompt-Neutron Activation Analysis of Coal," Trans. Am. Nucl. Soc., 27: pp. 161-162 (1977).

Rubinstein, R.Y., Simulation and the Monte Carlo Method, John-Wiley and Sons., Inc., New York (1981).

Sanders, L.G., "The Application of Monte Carlo Computations to Formation Analysis by Neutron Interactions," Int. J. Appl. Radiat. Isot. 34: No. 1, pp. 173-198 (1983).

Schaeffer, N.M. (ed.), Reactor Shielding for Nuclear Engineers, U.S. Atomic Energy Comission, TID-25951 (1973).

Schmidt, E. and P.F. Rose, "Monte Carlo Calculations of Neutron Induced Prompt γ Spectra," Int. J. Appl. Radiat. Isot. 35: No.8, pp. 796-798 (1984).

Selph, W.E. and C.W. Garrett, "Monte Carlo Methods for Radiation Transport," in Reactor Shielding for Nuclear Engineers, ed. N.M. Schaeffer, U.S. Atomic Energy Commission, TID-25951, pp. 207-257 (1973).

Senftle. F.E., A.G. Evans, D. Duffey, and P.F. Wiggins, "Construction Materials for Neutron Capture-Gamma-Ray Measurements Assembly Using Californium-252," Nucl. Tech. 10: pp 204-210 (February 1971).

Senftle, F.E., A.B. Tanner, P.W. Philbin, J.E. Noakes, J.D. Spaulding, and J.L Harding, "In-Situ Capture Gamma-Ray Analyses for Sea-Bed Exploration: A Feasibilty Study," Proceedings of a Panel on Nuclear Techniques in Geochemistry and Geophysics, IAEA, Vienna, pp. 75-91 (1974).

Sohrabpour, M. and S.R. Bull, "Elemental Sensitivity Data Modeling for In Situ Neutron Capture Gamma-Ray Experiments," Nucl. Instr. Meth. 161: pp. 281-289 (1979).

Spanier, J. and E.M. Gelbard, Monte Carlo Principles and Neutron Transport Problems, Addison-Wesley Publishing Co., Reading, Massachusetts (1969).

Stelson, P.H., J.K. Dickens, S. Raman, and R.C. Trammell, "Deterioration of Large Ge(Li) Diodes Caused by Fast Neutrons," Nucl. Instr. Meth. 98: pp. 481-484 (1972).

Storm, E. and H.I. Israel, "Photon Cross Sections from 1 KeV to 100 MeV for Elements Z=1 to Z=100," LA-3753 (1970).

Tanner, A.B., R.M. Moxham, and F.E. Senftle, "A Probe for Neutron Activation Analysis in a Drill Hole Using Cf-252, and a Ge(Li) Detector Cooled by a Melting Cryogen," Nucl. Instr. Meth. 100: pp. 1-7 (1972).

Thomas, B.W., C.G. Clayton, V.V.C. Ranasinghe, and I.M. Blair, "Mineral Exploration of Sea bed by Towed Sea bed Spectrometers," Int. J. Appl. Radiat. Isot. 34: No. 1, pp. 437-449 (1983).

Uusitalo, S., E. Mãkinen, and D.O. Riska, "On-line Neutron-Capture Gamma Analysis of Ore Concentrates," Inst. Phys. Conf. Ser. No. 62, pp. 682-683 (1982).

Van Otten, P., R. Van De Vyver, E. Van Camp, E. Kerkhove, P. Berkvens, H. Ferdinande, D. Ryckbosch, A. De Graeve, and L. Van Hoorebeke, "A General Monte Carlo Calculation for the Geometrical Efficiency of a Detection System," Nucl. Instr. Meth. in Physics Research A267: pp. 183-192 (1988).

Von Egidy, T., F. Gonnenwein, and B. Maier (Eds.) Neutron Capture Gamma-Ray Spectroscopy and Related Topics 1981. Proceedings of the Fourth Int. Symp. on Neutron Capture Gamma-Ray Spectroscopy and Related Topics, Grenoble, France, 7-11 September 1981. Conf. Series no. 62, The Institute of Physics, Bristol and London (1982).

Walker, J., "Uses of Neutrons in Engineering and Technology," in The Neutron and its Applications-1982, Inst. Phys., Bristol, Conf. Ser. No. 64, pp. 435-446 (1983).

Wiggins, P., F.E. Senftle, and D. Duffey, "Geochemical Mapping of the Ocean Floor Using Neutron Capture Gamma Rays," Trans. Marine Tech. Soc. 2: 1165 (1970).

Wormald, M.R., C.G. Clayton, I.S. Boyce, and D. Martimer, "A Method of Measuring the Ash Content of Coal in Moving Wagons," Int. J. Appl. Radiat. Isot. 30: pp. 297-314 (1979).

Wormald, M.R. and C.G. Clayton, "In-Situ Analysis of Coal by Measurement of Neutron-Induced Prompt γ-Rays," Int. J. Appl. Radiat. Isot. Vol.34, No. 1, pp. 71-82 (1983).

APPENDICES

APPENDIX A

Importance Sampling as a Variance Reduction Method

In many transport phenomena, it is possible to render that portions of a pdf in the phase space might be more likely to contribute to the desired result than the rest of the distribution. These regions are said to therefore be more important and the pdf could be mathematically altered to emphasize these regions, and the variance of the result may be correspondingly reduced.

Importance sampling can be illustrated by considering a function f(x) defined on the interval [a,b]. The variation of x on [a,b] is governed by the pdf p(x). The expected value of the function f(x) in the interval is:

$$\langle \tau \rangle = \int_a^b f(x)\ p(x)\ dx$$

Suppose that for convenience or to reduce the error in x, one wishes to sample x from an altered pdf constructed as $p^*(x)$. It is required that the expected value is unaltered through the use of an appropriate weight function:

$$\langle \tau \rangle = \int_a^b f(x)\ p^*(x)\ w(x)\ dx$$

The weight function w(x) clearly should have the form:

$$w(x) = \frac{p(x)}{p^*(x)}$$

The variances as obtained from both distributions are:

$$\sigma^2 = \int_a^b [f(x)-\tau]^2\, p(x)\, dx$$

$$= \int_a^b f^2(x)\, p(x)\, dx - \tau^2$$

and

$$\tilde{\sigma}^2 = \int_a^b \tilde{f}^2(x)\, p^*(x)\, dx - \tau^2$$

where

$$\tilde{f}(x) \equiv f(x)\, w(x)$$

$$\tilde{\sigma}^2 = \int_a^b [f(x)\, w(x)]^2\, p^*(x)\, dx - \tau^2$$

$$= \int_a^b [f(x)\, \frac{p(x)}{p^*(x)}]^2\, p^*(x)\, dx - \tau^2$$

$$= \int_a^b \frac{p(x)}{p^*(x)}\, f^2(x)\, p(x)\, dx - \tau^2$$

Both σ^2 and $\tilde{\sigma}^2$ are positive and for the variance to be reduced in the new altered pdf sampling, the weight $p(x)/p^*(x)$ must be <1 over the portion of the interval that is deemed important.

The above method can be implemented in a Monte Carlo simulation, given a pdf $p(x)$ on $x\in[a,b]$. An importance function $I(x)$, which is designed to emphasize the important region of $[a,b]$, is defined, and the new altered pdf $p^*(x)$ is constructed such that:

$$p^*(x) = C\, p(x)\, I(x)$$

where C is a normalization constant such that

$$\int_a^b p^*(x)\, dx = 1$$

To prevent biasing, it is required that the total number of sampled variables from each interval of the two distributions is the same, which defines the weight function:

$$w(x)\ p^*(x)\ dx = p(x)\ dx$$

The random variable x is sampled from the modified distribution $p^*(x)$ and the history is weighted by w(x).

A discrete function may be defined to define a truncated path length. The pdf that governs the path length between collisions is given by:

$$p(x)\ dx = \mu\ e^{-\mu x}\ dx \quad ,x\epsilon(0,\infty) \tag{A-1}$$

When the region of interest is within a small distance, say δ, of the cell boundary, a discrete importace function I(x) can be defined to emphasize the region inside the cell and to undermind the regions beyond the distance δ (since any particle that exits the cell is considered lost) such that:

$$I(x) = 1 \qquad ;x\epsilon(0,\delta)$$

$$I(x) = 0 \qquad ;x\epsilon(\delta,\infty)$$

The modified pdf is

$$p^*(x)\ dx = C\ p(x)\ I(x)\ dx$$

The normalization constant

$$C = \frac{1}{\sum_{n=1}^{2} I_n(x) \int_{\Delta x_n} p(x)\ dx}$$

$$= \frac{1}{(1)\int_0^{\delta} \mu\ e^{-\mu x}\ dx + (0)\int_{\delta}^{\infty} \mu\ e^{-\mu x} dx}$$

$$C = \frac{1}{1 - e^{-\mu\delta}}$$

Therefore,

$$p^*(x)\ dx = \frac{\mu\ e^{-\mu x}\ dx}{1 - e^{-\mu\delta}} \qquad ;x\epsilon(0,\delta) \qquad (A\text{-}2)$$

and the weight is

$$w(x) = \frac{p(x)}{p^*(x)} = 1 - e^{-\mu\delta}$$

This result is equivalent to the "common sense" of forcing an interaction to take place within $[0,\delta]$.

It is obvious that, since $p(x)/p^*(x) < 1$, that this procedure would result in reducing the variance.

APPENDIX B

Sampling the Type of Interaction

This scheme is based on sampling from a discrete cummulative distribution function (cdf) that is constructed by summing up the macroscopic j-th type cross section for the i-th element, $\Sigma_{i,j}$, over all constituents of the medium where the transport phenomenon is taking place. Thus, the total macroscopic cross section of the j-th type reaction for the medium is

$$\Sigma_j(E) = \sum_{i=1}^{M} \Sigma_{i,j}(E)$$

where M is the total number of elements in the medium.

The total macroscopic cross section Σ_t for the medium is obtained by summing over all possible interaction types (a total of N types), i.e.,

$$\Sigma_t(E) = \sum_{j=1}^{N} \Sigma_j(E)$$

Therefore, the probability that the j-th type interaction takes place is $p_j = \Sigma_j/\Sigma_t$ and the type of interaction (m+1) is sampled by determining the value of m that satisfies:

$$\sum_{j=0}^{m} \Sigma_j < \xi\Sigma_t \leq \sum_{j=0}^{m+1} \Sigma_j$$

where $\Sigma_0 = 0$ by definition and ξ is a random number uniformly distributed on (0,1).

An absorption of a neutron by any element removes that neutron from the system and no further tracking is possible. If this absorption is by an element whose neutron capture gamma ray response is not of interest, the neutron history is terminated before a favorable contribution to the desired response. This in fact increases the variance. Thus, it can be seen that, provided the absorption type reaction is one of the reactions under consideration, when a neutron absorption reaction is sampled, the history is terminated inefficiently.

APPENDIX C

The Proton Gas Model

The probability that a neutron with the laboratory energy E will collide with a monatomic hydrogen gas in thermal equilibrium at the temperature T and emerge with an energy between E' and $E' + dE'$ is given by the Wigner-Wilkins proton gas model:

$$p(E \rightarrow E') = f(E) \begin{cases} \operatorname{erf}\sqrt{\frac{E'}{kT}} & ;E'<E \\ e^{\frac{(E-E')}{kT}} \operatorname{erf}\sqrt{\frac{E}{kT}} & ;E'>E \end{cases} \qquad \text{(C-1)}$$

where the normalization factor f(E) is independent of E'.

The upscattering in neutron energy in the thermal region neutron scattering reactions is illustrated in Figure C-1 that shows a graph of Equation (C-1) at three different energies of the neutron prior to the scattering. Figure C-2 shows the Monte Carlo sampled monatomic gas model of Section 5.4.2.1 in comparison to the calculated Wigner-Wilkins model.

A neutron of 80 kT (kT = 0.0253 eV at room temperature) energy scatters almost isotropically. Therefore, it is safe to assume that the gas model should be used only when the neutron energy (prior to scattering) is below 2 eV (80 kT).

Except for the inherent statistical fluctuations in the Monte Carlo results, the agreement in Figure C-2 is evident.

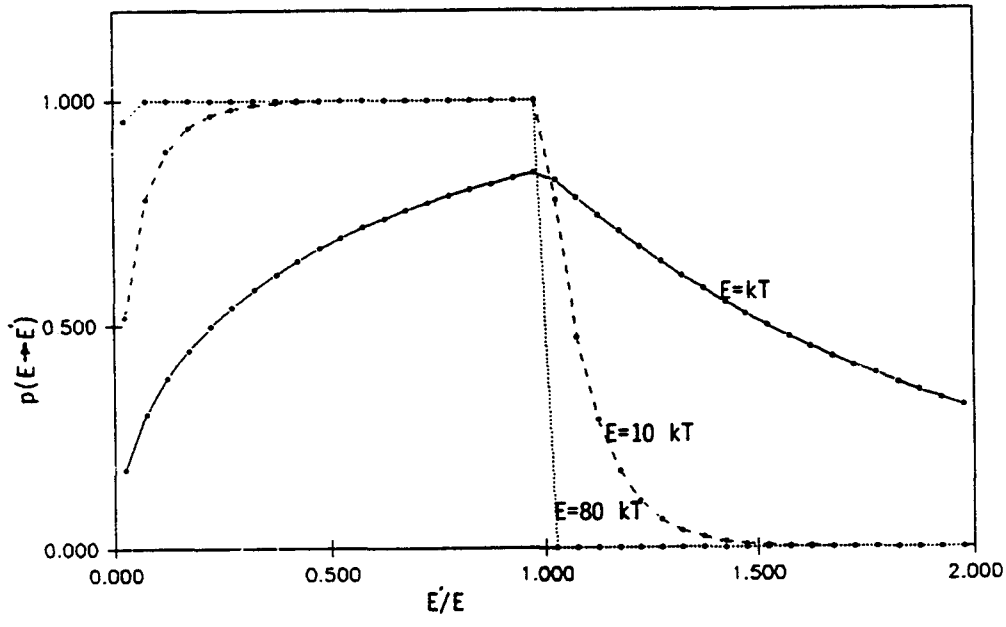

Figure C-1 The scattering probability distribution given by the proton gas model.

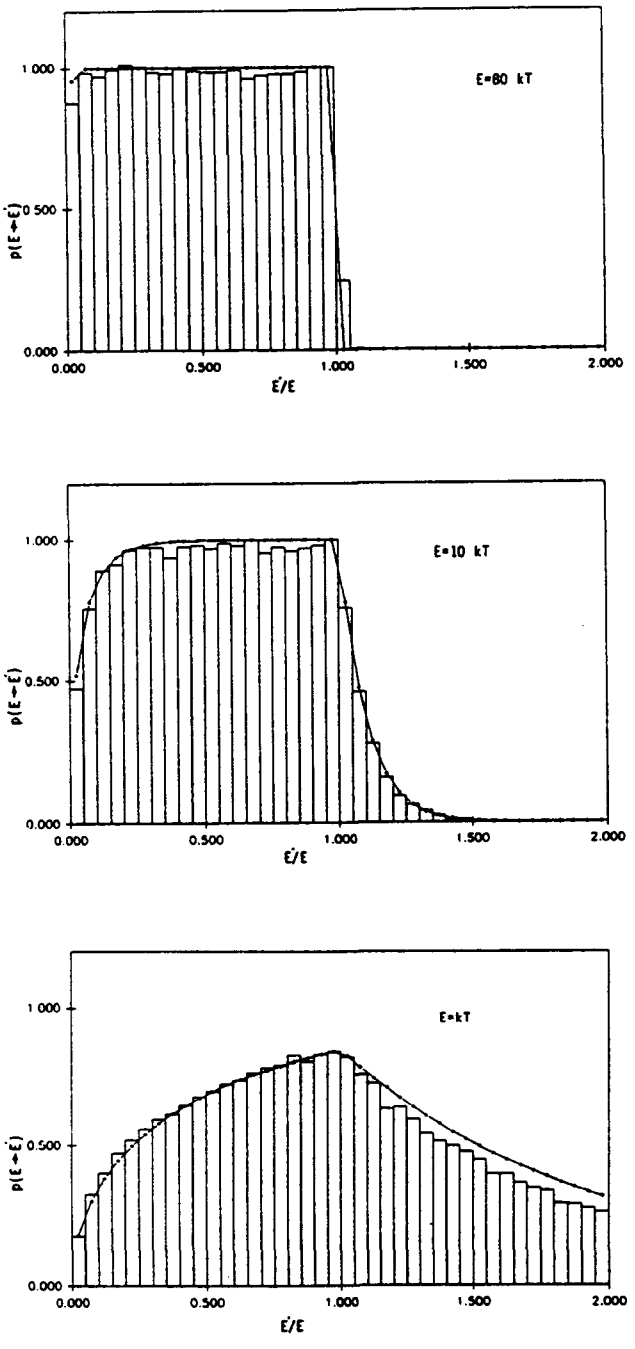

Figure C-2 The monatomic gas model, sampled by the Monte Carlo method (histogram), at three different neutron temperatures as compared to Equation (C-1) (solid curve).

APPENDIX D

Angular Distribution of Scattered Neutrons

ENDF/B-V data are given for a series of incident neutron energies in order of increasing energy. The angular distributions are expressed as normalized probability distributions, i.e.,

$$\int_{-1}^{1} p(\mu,E)\ d\mu \equiv 1$$

where $p(\mu,E)$ is the probability that a neutron of incident energy E will be scattered into the interval $d\mu$ about an angle whose cosine is μ. Since the angular distribution of scattered neutrons is generally assumed to have azimuthal symmetry, the polar angular distributions may be represented as Legendre polynomial series:

$$p(\mu,E) = \frac{2\pi}{\sigma_s(E)} \frac{d\sigma(\Omega,E)}{d\Omega} = \sum_{n=0}^{NL} \frac{2n+1}{2}\ a_n(E)\ P_n(\mu) \quad (D\text{-}1)$$

where:

μ is the cosine of the scattering angle in either the laboratory or the center-of-mass system, depending on the data furnished,

E is the energy of the incident neutron in the laboratory system,

$\sigma_s(E)$ is the scattering cross section (e.g., elastic) at energy E,

n is the order of the Legendre polynomial,

$d\sigma(\Omega,E)/d\Omega$ is the differential scattering cross section in units of barns per steradian, and

a_n is the n-th Legendre polynomial coefficient of expansion; it is understood that $a_0 = 1$.

The given coefficients $a_n(E)$ are tabulated as a function of discrete incident neutron energies. The coefficients at intermediate neutron energies that are not tabulated may be obtained by linear interpolation (Kinsey, 1979).

To sample the angular distribution in Monte Carlo simulation, the Legendre expansion coefficients are interpolated at the incident neutron energy of interest, say E. Then the cosine of the scattering angle μ may be sampled directly from:

$$\int_{-1}^{\mu} p(\mu',E)\ d\mu' = \xi \qquad ,\xi\epsilon(0,1)$$

or

$$\xi = \sum_{n=0}^{NL} \frac{2n+1}{2}\ a_n(E) \int_{-1}^{\mu} p_n(\mu')\ d\mu'$$

$$= \frac{1}{2}\ a_0(E) \int_{-1}^{\mu} p_0(\mu')\ d\mu' + \sum_{n=1}^{NL} \frac{2n+1}{2}\ a_n(E) \int_{-1}^{\mu} p_n(\mu')\ d\mu'$$

$$= \frac{1}{2}(\mu+1) + \sum_{n+1}^{NL} \frac{2n+1}{2} a_i(E)\ \frac{P_{n+1}(\mu')-P_{n-1}(\mu')}{2n+1}\Bigg|_{-1}^{\mu}$$

$$= \frac{1}{2}(\mu+1) + \sum_{n=1}^{NL} \frac{a_n(E)}{2}[p_{n+1}(\mu)-p_{n-1}(\mu)-p_{n+1}(-1)+P_{n-1}(-1)]$$

The last two terms in the RHS brackets vanish since

$$p_n(-1) = (-1)^n$$

hence,

$$\xi = \frac{1}{2}\,(\mu+1) + \sum_{n+1}^{NL} \frac{a_n(E)}{2}\,[P_{n+1}(\mu) - P_{n-1}(\mu)] \qquad (D\text{-}2)$$

A numerical root-locating scheme is employed to solve for μ (e.g., the bisection method).

APPENDIX E

Some Vector Properties Relevant to Tracking

Direction cosines

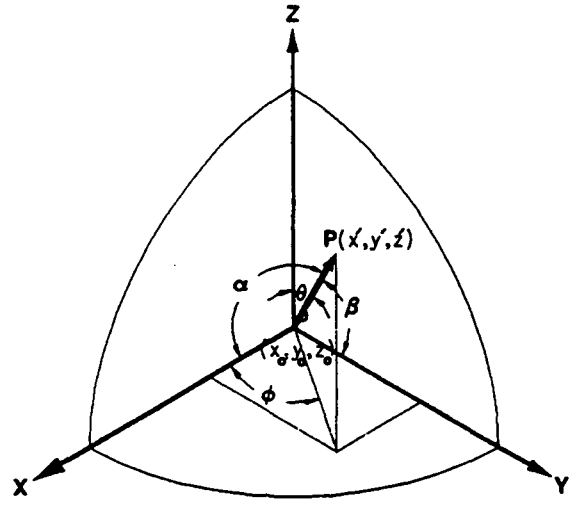

Figure E-1 Direction cosines in cartesian coordinates.

In reference to the cartesian coordinates shown in Figure E-1, the distance δ from point (x_0,y_0,z_0) to point (x',y',z') is:

$$\delta = \sqrt{(x'-x_0)^2 + (y'-y_0)^2 + (z'-z_0)^2} \qquad \text{(E-1)}$$

and the x, y, and z projections of the vector P are given as:

$$\begin{aligned} x' - x_0 &= \delta \cos\alpha \\ y' - y_0 &= \delta \cos\beta \\ z' - z_0 &= \delta \cos\theta \end{aligned} \qquad \text{(E-2)}$$

The following variables can be defined as direction cosines:

$$\Omega_x = \cos\alpha$$

$$\Omega_y = \cos\beta$$

$$\Omega_z = \cos\theta \qquad \text{(E-3)}$$

Therefore, one can write the expressions in Equation (E-2) as:

$$\frac{x'-x_0}{\delta} = \Omega_x \quad , \quad \frac{y'-y_0}{\delta} = \Omega_y \quad , \quad \frac{z'-z_0}{\delta} = \Omega_z \qquad \text{(E-4)}$$

or

$$x' = x_0 + \Omega_x \delta$$

$$y' = y_0 + \Omega_y \delta$$

$$z' = z_0 + \Omega_z \delta \qquad \text{(E-5)}$$

Notice that $\Omega_X^2 + \Omega_y^2 + \Omega_Z^2 = 1$.

The normalization can be verified by substituting the expressions in Equation (E-4) for Ω_X, Ω_y, and Ω_Z and using the distance of Equation (E-1).

The Equations (E-4) allow one to determine the direction cosines of a line between any two points in a 3-D space. Furthermore, given an initial point in the 3-D space, a particle direction, and a particle path length, one can determine the final particle position via the parametric Equations (E-5).

Vector Representation and Parametric Equations

A vector P spanning the distance from point (x_0,y_0,z_0) to point (x_1,y_1,z_1) can be represented as:

$$P = a\,\hat{i} + b\,\hat{j} + c\,\hat{k}$$

where a, b, and c are called the direction numbers and i, j, and k are unit vectors in the x, y, and z direction, respectively. By substituting for the direction numbers, the vector may be written in particular as:

$$P = (x_1-x_0)\,\hat{i} + (y_1-y_0)\,\hat{j} + (z_1-z_0)\,\hat{k}$$

Since parallel vectors have proportional direction numbers, therefore, a vector Q in the same direction as P may be written as:

$$Q = \Omega_x\,\hat{i} + \Omega_y\,\hat{j} + \Omega_z\,\hat{k}$$

where Ω_X,Ω_y, and Ω_Z are the direction cosines. Thus, any vector between two points may be described by the direction cosines of that path, and the parametric representation of lines between points follows, namely

$$x = x_0 + \Omega_x\,\delta$$

$$y = y_0 + \Omega_y\,\delta$$

$$z = z_0 + \Omega_z\,\delta$$

The parameter δ is recognized as the distance between points (x_0,y_0,z_0) and (x,y,z).

Some Properties of Vectors and Direction Cosines

The cosine of the angle Ψ between the vectors $P_1 = \Omega_{X1}\,\hat{i} + \Omega_{y1}\,\hat{j} + \Omega_{Z1}\,\hat{k}$ and $P_2 = \Omega_{X2}\,\hat{i} + \Omega_{y2}\,\hat{j} + \Omega_{Z2}\,\hat{k}$ is obtained by the dot

product $P_1 \cdot P_2$, i.e., $\cos\Psi = \Omega_{x1}\Omega_{x2} + \Omega_{y1}\Omega_{y2} + \Omega_{z1}\Omega_{z2}$. It can be shown that two parallel vectors have $\cos\Psi = 1$ or $\Psi = 0$, and two perpendicular vectors have $\cos\Psi = 0$.

Relationship between θ, ϕ, and the direction cosines

The polar angle θ and the azimuthal angle ϕ are used to compute the cartesian coordinates associated with the vector P as

$$x = 0 + \delta \sin\theta \cos\phi$$

$$y = 0 + \delta \sin\theta \sin\phi$$

$$z = 0 + \delta \cos\theta$$

which are recognized as the parametric representations of the line for point (0,0,0) to point (x,y,z). Therefore,

$$\Omega_x = \sin\theta \cos\phi$$

$$\Omega_y = \sin\theta \sin\phi$$

$$\Omega_z = \cos\theta$$

APPENDIX F

General Algorithm to Calculate the Solid Angle

(Adopted from Mickael, 1988)

If the axes are translated (and rotated in the case that the incident particle direction at the point of interaction is not collinear with the new translated axis, although this is irrelevant in the case of isotropic capture gamma ray emission at the point of interaction), the new cartesian coordinate system should have the origin (0,0,0) at the interaction point as shown in Figure F-1.

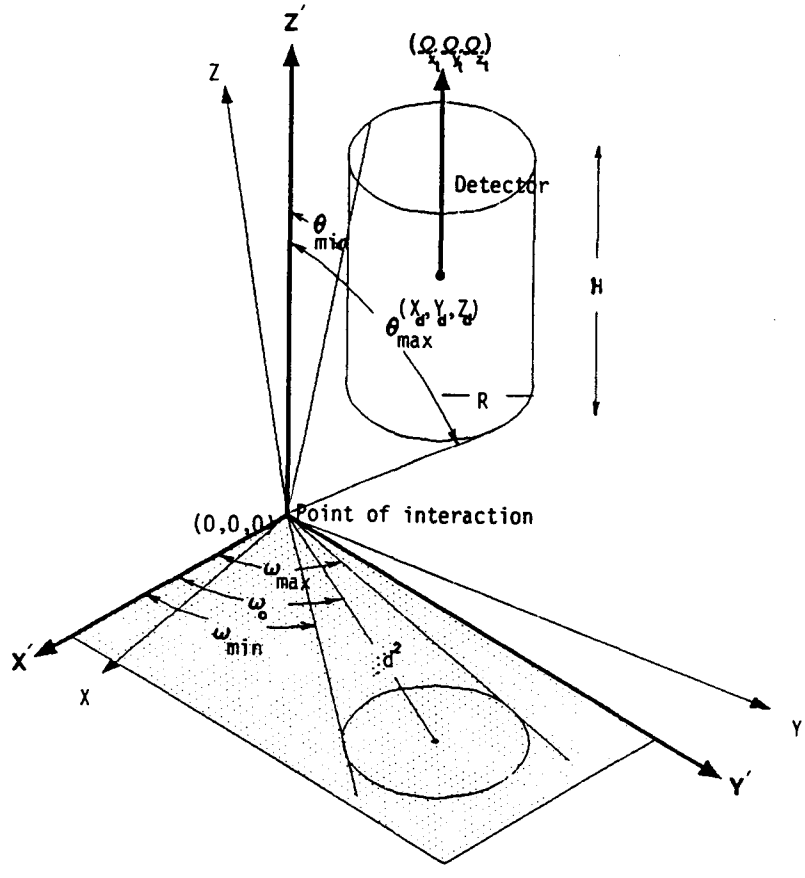

Figure F-1 Limiting polar and azimuthal angles for the solid angle subtended by the detector at the origin.

Let (x_0,y_0,z_0) be the cartesian coordinates of the interaction point relative to the master coordinate system, $(\Omega_{xo},\Omega_{yo},\Omega_{zo})$ be the direction cosines of the incident particle (gamma ray) direction (for isotropic emission at this point, these are arbitrarily taken to be (0,0,1), (x_d,y_d,z_d) be the cartesian coordinates of the detector geometrical center, R and H be the radius and the height of the detector, respectively, and $(\Omega_{xt},\Omega_{yt},\Omega_{zt})$ be the direction cosines of the major axis of the detector (in the proposed monitoring system in this work, this axis is collinear with the master axis on the z-axis and $\Omega_{xt}=0$, $\Omega_{yt}=0$, $\Omega_{zt}=1$). It has been recognized that the calculations of the limiting angles can be simplified when measured from the direction that is parallel to the detector z-axis, for then the projection of the intersection of the polar angle cone with the circular cylinder in the perpendicular plane to the direction is a circle rather than an ellipse. If the axes are translated such that the interaction point coordinates are at the new coordinate origin, then the detector center coordinates are

$$X_d = x_d - x_0$$

$$Y_d = y_d - y_0$$

$$Z_d = z_d - z_0$$

The direction cosines that are parallel to the detector z-axis are:

$$\dot{\Omega}_x = \Omega_{xt}$$

$$\dot{\Omega}_y = \Omega_{yt}$$

$$\dot{\Omega}_z = \Omega_{zt}$$

and the transferred axis such that the detector axis lies on the z-axis results in the coordinates:

$$X'_d = \Omega_{zt}(\Omega_{xt}X_d + \Omega_{yt}Y_d)(1-\Omega_{zt}^2)^{-1/2} - (1-\Omega_{zt}^2)^{-1/2} Z_d$$

$$Y'_d = (\Omega_{xt}Y_d - \Omega_{yt}X_d)(1-\Omega_{zt}^2)^{-1/2}$$

$$Z'_d = \Omega_{xt}X_d + \Omega_{yt}Y_d + \Omega_{zt}Z_d$$

Notice that if $\Omega_{zt}=1$, then X'_d, Y'_d, and Z'_d are identical to X_d, Y_d, and Z_d. The position of the interaction point with respect to the detector is determined by first calculating:

$$d^2 = X_d'^2 + Y_d'^2$$

$$Z_B = Z'_d - \frac{H}{2}$$

$$Z_T = Z'_d + \frac{H}{2}$$

$$\omega_0 = \tan^{-1}\left(\frac{Y'_d}{X'_d}\right)$$

The following cases are recognized:

Case I: $d^2 \geq R^2$

The cosines of the limiting polar angles are given by:

$$\nu_{min} = \frac{Z_B}{\sqrt{(d+R)^2 + Z_B^2}} \qquad ; Z_B>0$$

$$\nu_{min} = \frac{Z_B}{\sqrt{(d-R)^2 + Z_B^2}} \qquad ; Z_B<0$$

and

$$\nu_{max} = \frac{Z_T}{\sqrt{(d-R)^2 + Z_T^2}} \qquad ; Z_T > 0$$

$$\nu_{max} = \frac{Z_T}{\sqrt{(d+R)^2 + Z_T^2}} \qquad ; Z_T < 0$$

Cosines ν_1 and ν_2 are defined as

$$\nu_1 = \frac{Z_T}{\sqrt{r_c^2 + Z_T^2}}$$

$$\nu_2 = \frac{Z_B}{\sqrt{r_c^2 + Z_B^2}}$$

where

$$r_c^2 = d^2 - R^2$$

For a sampled $\nu \in (\nu_{min}, \nu_{max})$, the limiting azimuthal angles are

$$\omega_{min} = \omega_0 - \Delta\omega$$

$$\omega_{max} = \omega_0 + \Delta\omega$$

where

$$\Delta\omega = \cos^{-1}\left(\frac{Z_T^2(1-\nu^2) + r_c^2\nu^2}{2dZ_T\nu\sqrt{1-\nu^2}}\right) \qquad ; \nu_1 \le \nu \le \nu_{max}$$

$$\Delta\omega = \sin^{-1}\left(\frac{R}{d}\right) \qquad ; \nu_2 < \nu < \nu_1$$

$$\Delta\omega = \cos^{-1}\left(\frac{Z_B^2(1-\nu^2) + r_c^2\nu^2}{2dZ_B\nu\sqrt{1-\nu^2}}\right) \qquad ; \nu_{min} \le \nu \le \nu_2$$

Case II: $d^2 \le R^2$

The cosines of the limiting polar angles are given by

$$\nu_{min} = \frac{Z_B}{\sqrt{(d+R)^2 + Z_B^2}} \qquad ; Z_B > 0$$

$$\nu_{min} = -1 \qquad ; Z_T < 0$$

and

$$\nu_{max} = 1 \qquad ;Z_B>0$$

$$\nu_{max} = \frac{Z_T}{\sqrt{(d+R)^2 + Z_T^2}} \qquad ;Z_T<0$$

If ν_c is defined as

$$\nu_c = \frac{Z_B}{\sqrt{(d-R^2) + Z_B^2}} \qquad ;Z_B>0$$

$$\nu_c = \frac{Z_T}{\sqrt{(d-R^2) + Z_T^2}} \qquad ;Z_T<0$$

when ν is sampled from $\nu \in (\nu_{min},\nu_{max})$, the limiting azimuthal angles, shown in Figure F-2, are given by

$$\omega_{min} = \omega_0 - \Delta\omega$$

$$\omega_{max} = \omega_0 + \Delta\omega$$

where

$$\Delta\omega = \pi \qquad ;\nu_c \le \nu \le \nu_{max} \quad \text{and} \quad Z_B>0$$

$$\text{or } \nu_{min} \le \nu \le \nu_c \quad \text{and} \quad Z_T<0$$

$$\Delta\omega = \cos^{-1}\left(\frac{Z_T^2(1-\nu^2) + r_c^2\nu^2}{2dZ_T\nu\sqrt{1-\nu^2}}\right) \qquad ;\nu_c<\nu<\nu_{max};Z_T<0$$

$$\Delta\omega = \cos^{-1}\left(\frac{Z_B^2(1-\nu^2) + r_c^2\nu^2}{2dZ_B\nu\sqrt{1-\nu^2}}\right) \qquad ;\nu_{min}<\nu<\nu_c;Z_B>0$$

The fractional solid angle subtended by the detector at the interaction point (the probability that the emission is to intersect the finite detector) is calculated as:

$$W_\Omega = \int_{\nu_{min}}^{\nu_{max}} \int_{\omega_{min}}^{\omega_{max}} \Lambda(\nu,\omega)\, d\nu\, d\omega$$

where $\Lambda(\nu,\omega)$ is a transformed pdf. In the case of isotropic emission:

$$\Lambda(\nu,\omega)\ d\nu\ d\omega = \frac{1}{4\pi}\ d\nu\ d\omega$$

where ν and ω are the cosines of the limiting polar and azimuthal angles to the detector.

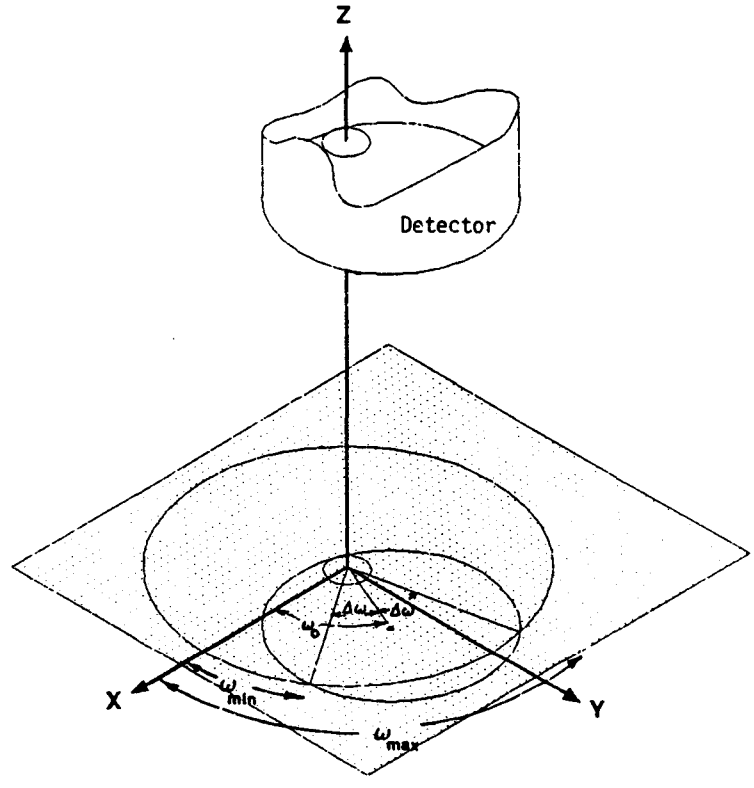

Figure F-2 The limiting azimuthal angles when the emission point is within the radius of the detector.

The probability that the emission is to intersect the cylindrical detector is calculated as follows: The limiting polar

and azimuthal angles are independent of each other for a subset of ν between the limiting polar angles. The integral in the expression for W_Ω is evaluated analytically whenever ν and ω are independent. For the integrals when the limiting azimuthal angles are dependent on ν, the angle can be evaluated based on an average value of ν between its limits with the integral of ω being carried out analytically.

When $d^2 \geq R^2$

$$W_\Omega = \Lambda(\nu,\omega)\Big|_{\omega=\omega^{\bullet}_{min}}^{\omega=\omega^{\bullet}_{max}}\Big|_{\nu=\nu_{min}}^{\nu=\nu_2} + \Lambda(\nu,\omega)\Big|_{\omega=\omega_{min}}^{\omega=\omega_{max}}\Big|_{\nu=\nu_2}^{\nu=\nu_1} + \Lambda(\nu,\omega)\Big|_{\omega=\omega^{*}_{min}}^{\omega=\omega^{*}_{max}}\Big|_{\nu=\nu_1}^{\nu=\nu_{max}}$$

where the superscript $(\bullet)$ indicates that the azimuthal angle is evaluated at an average value of the polar angle as

$$\frac{(\nu_2 + \nu_{min})}{2}$$

Similarly, for the superscript (*) the azimuthal angle is evaluated at

$$\frac{(\nu_{max} + \nu_1)}{2}$$

When $d^2 \leq R^2$

For $Z_T < 0$:

$$W_\Omega = \Lambda(\nu,\omega)\Big|_{\omega=\omega_{min}}^{\omega=\omega_{max}}\Big|_{\nu=\nu_{min}}^{\nu=\nu_c} + \Lambda(\nu,\omega)\Big|_{\omega=\omega^{\oplus}_{min}}^{\omega=\omega^{\oplus}_{max}}\Big|_{\nu=\nu_c}^{\nu=\nu_{max}}$$

and for $Z_B > 0$:

$$W_\Omega = \Lambda(\nu,\omega)\Big|_{\omega=\omega^{\circledast}_{min}}^{\omega=\omega^{\circledast}_{max}}\Big|_{\nu=\nu_{min}}^{\nu=\nu_c} + \Lambda(\nu,\omega)\Big|_{\omega=\omega_{min}}^{\omega=\omega_{max}}\Big|_{\nu=\nu_c}^{\nu=\nu_{max}}$$

The superscript ($\circledast$) indicates that the azimuthal angle is evaluated at an average value of the polar angle as

$$\frac{(\nu_c + \nu_{max})}{2}$$

and similarly for the superscript ($\otimes$) at

$$\frac{(\nu_c + \nu_{min})}{2}$$

APPENDIX G

Statistical Estimates

The most probable estimate of the mean μ of a population (of limited number N) is the average x of the observations:

$$\mu \cong \bar{x} \equiv \frac{1}{N} \sum_{i=1}^{N} x_i \qquad \text{(G-1)}$$

The best estimate of the variance in the mean σ_x^2 is given by the sample variance:

$$\sigma_{\bar{x}}^2 \cong s^2 \equiv \frac{1}{N-1} \sum_{i=1}^{N} (x_i - \bar{x})^2 \qquad \text{(G-2)}$$

When the values Σx_i and Σx_i^2 are accumulated, Equation (G-2) may be written in the form:

$$\sigma_{\bar{x}}^2 = \frac{1}{N-1} \left[\sum_{i=1}^{N} \{x_i^2 - 2\bar{x}x_i + (\bar{x})^2\} \right]$$

$$= \frac{1}{N-1} \left[\sum_{i=1}^{N} x_i^2 - 2\bar{x} \sum_{i=1}^{N} x_i + \sum_{i=1}^{N} (\bar{x})^2 \right]$$

$$= \frac{1}{N-1} \left[\sum_{i=1}^{N} x_i^2 - 2\bar{x}(N\bar{x}) + N(\bar{x})^2 \right]$$

$$= \frac{1}{N-1} \left[\sum_{i=1}^{N} x_i^2 - N(\bar{x})^2 \right]$$

and

$$\sigma_{\bar{x}} = \sqrt{\frac{1}{N(N-1)} \left[\sum_{i=1}^{N} x_i^2 - \frac{(\sum_{i=1}^{N} x_i)^2}{N} \right]} \qquad \text{(G-3)}$$

For the relative detector responses, it is necessary to

determine the standard deviation of a ratio. Given that R=x/y and a statistical ensemble of x and y values can be found using Equation (G-1), and σ_x and σ_y values from Equation (G-3), the theory of propagation of errors yields:

$$\sigma_R^2 \cong \sigma_{\bar{x}}^2\left(\frac{\partial R}{\partial x}\right)^2 + \sigma_{\bar{y}}^2\left(\frac{\partial R}{\partial y}\right)^2 + 2\sigma_{xy}^2\left(\frac{\partial R}{\partial x}\right)\left(\frac{\partial R}{\partial y}\right) \qquad \text{(G-4)}$$

where

$$\sigma_{xy}^2 \equiv \lim_{N\to\infty} \frac{1}{N} \sum_{i=1}^{N} (x_i - \bar{x})(y_i - \bar{y})$$

For a finite value of N,

$$\sigma_{xy}^2 = \frac{1}{N-1}\left[\sum_{i=1}^{N} (x_i y_i - x_i\bar{y} - \bar{x}y_i + \bar{x}\,\bar{y})\right]$$

$$= \frac{1}{N-1}\left[\sum_{i=1}^{N} x_i y_i - \bar{y}\sum_{i=1}^{N} x_i - \bar{x}\sum_{i=1}^{N} y_i + N\bar{x}\,\bar{y}\right]$$

and

$$\sigma_{xy} = \sqrt{\frac{1}{N(N-1)}\left[\sum_{i=1}^{N} x_i y_i - \frac{\sum_{i=1}^{N} x_i \sum_{i=1}^{N} y_i}{N}\right]} \qquad \text{(G-5)}$$

If the definition of Equation (G-4) is applied to R = x/y:

$$\sigma_R^2 = \sigma_{\bar{x}}^2\left(\frac{1}{y^2}\right) - 2\sigma_{xy}^2(R)\left(\frac{1}{y^2}\right) + \sigma_{\bar{y}}^2(R^2)\left(\frac{1}{y^2}\right) \qquad \text{(G-6)}$$

If Equations (G-3) and (G-5) are substituted into the corresponding values in Equation (G-6):

$$\sigma_R^2=\frac{1}{N(N-1)(\Sigma y_i)^2}\left[\left(\Sigma x_i^2-\frac{(\Sigma x_i)^2}{N}\right)N^2-2R\left(\Sigma x_i y_i-\frac{\Sigma x_i \Sigma y_i}{N}\right)N^2+R^2\left(\Sigma y_i^2-\frac{(\Sigma y_i)^2}{N}\right)N^2\right]$$

and

$$\sigma_R=\frac{1}{\sum_{i=1}^{N} y_i}\left[\left(\Sigma x_i^2-\frac{(\Sigma x_i)^2}{N}\right)-2R\left(\Sigma x_i y_i-\frac{\Sigma x_i \Sigma y_i}{N}\right)+R^2\left(\Sigma y_i^2-\frac{(\Sigma y_i)^2}{N}\right)\right]^{1/2}$$

$$\sigma_R=\frac{1}{\sum_{i=1}^{N} y_i}\left[\sum_{i=1}^{N} x_i^2-\frac{\Sigma x_i y_i}{N}-2R\sum_{i=1}^{N} x_i y_i+2\frac{\Sigma x_i \Sigma y_i}{N}\left(\frac{\Sigma x_i}{\Sigma y_i}\right)+R^2\Sigma y_i^2-\frac{\Sigma y_i \Sigma y_i}{N}\left(\frac{\Sigma x_i \Sigma x_i}{\Sigma y_i \Sigma y_i}\right)\right]^{1/2}$$

or

$$\sigma_R = \frac{1}{\sum_{i=1}^{N} y_i}\sqrt{\sum_{i=1}^{N} x_i^2 - 2R\sum_{i=1}^{N} x_i y_i + R^2\sum_{i=1}^{N} y_i} \qquad \text{(G-7)}$$

APPENDIX H

Printouts from MCNCP

MONTE CARLO SIMULATION

CAPTURE GAMMA RAY ANALYZER OF A SEAFLOOR CORE SAMPLE
Programmer: Abdullah M.S. Almasoumi (Nov. 1989)

Monitoring System Dimensions (cm):	
Container tank radius	= 50.00
Container tank height	=100.00
x-coordinate of the centerline of sample tube	= 0.00
y-coordinate of the centerline of sample tube	= 17.55
Radius of the core sample	= 3.75
Thickness of the casing around the sample	= 0.50
Thickness of the sample tube material	= 1.00
Thickness of the Cd annular shield	= 0.30
Thickness of the polyethylene surrounding the Cd	= 0.50
Length of the lower sample sleeve	= 59.00
Length of the upper sample sleeve	= 10.00
x-coordinate of the centerline of source tube	= 0.00
y-coordinate of the centerline of source tube	= -3.00
Radius of the Cf-252 neutron source capsule	= 0.50
Length of the Cf-252 neutron source capsule	= 5.00
Inner radius of the source tube	= 5.00
Thickness of the source tube construction material	= 1.00
Length of the Pb shield around the source	= 10.00
Length of the polyethylene shield above the Pb	= 10.00
x-coordinate of the centerline of detector tube	= 0.00
y-coordinate of the centerline of detector tube	= -3.00
Inner radius of the detector tube	= 6.25
Inner length of the detector tube	= 73.00
Thickness of the detector tube construction material	= 1.00
Thickness of the Cd wafer inside detector tube	= 0.30
Length of the Pb cone inside detector tube	= 5.00
Length of the detector Al casing	= 13.50
Radius of the detector Al casing	= 3.75
Height of the detector crystal	= 5.00
Radius of the detector crystal	= 2.50

Refer to Section 4.1 for detailed description of the monitoring system.

M.C. PREDICTED PHOTOPEAK RESPONSES OF CAPTURE GAMMA RAYS
(1000 histories)

Element	Energy (MeV)	Absolute Response (γ-ray/source n)	Std.dev.
Mg	0.5852	8.646D-17	3.386D-17
	1.8089	7.183D-17	3.046D-17
	2.8281	8.332D-17	3.674D-17
	3.9167	7.873D-17	3.555D-17
Cl	5.7153	4.099D-17	1.666D-17
	6.1109	1.375D-16	5.596D-17
	6.6195	4.638D-17	1.887D-17
	7.4138	3.809D-17	1.552D-17
	7.7902	3.088D-17	1.259D-17
Ti	0.3417	1.729D-16	7.353D-17
	1.3815	1.226D-15	4.874D-16
	6.4184	6.501D-17	2.578D-17
	6.7598	4.231D-17	1.678D-17
Cr	0.8351	3.024D-17	1.199D-17
	7.9393	1.916D-18	-3.674D-39 *
	8.8841	2.982D-18	-8.902D-39 *
Mn	7.0578	1.760D-18	-3.100D-39 *
	7.2438	1.718D-18	-2.953D-39 *
Fe	0.3522	2.023D-16	8.233D-17
	6.0185	2.023D-16	2.035D-17
	7.6311	9.047D-17	3.483D-17
	7.6455	7.624D-17	2.936D-17

* The expression for the standard deviation, Equation (G-3), contains a sum of the squares of the score per history (Σx_i); subroutine STATS in MCNCP accumulates the summation with the condition that when $x_i \leq 10^{-15}$, the quantity x^i is set to zero to avoid an underflow error on the PC. Apparently, this condition reduces the sum Σx_i enough to yield a very small negative value when Equation (G-3) was used.

NORMALIZED VARIATION OF RESPONSES WITH CONCENTRATION

Element no. 1 (Mg) has been changed sequentially

Element	Energy	Concentration *								
	(MeV)	1	2	3	4	5	6	7	8	9
Mg	0.5852	0.208	0.412	0.612	0.808	1.000	1.189	1.374	1.556	1.735
	1.8089	0.207	0.411	0.610	0.807	1.000	1.190	1.377	1.561	1.743
	2.8281	0.207	0.410	0.610	0.806	1.000	1.191	1.378	1.563	1.746
	3.9167	0.207	0.410	0.610	0.806	1.000	1.191	1.379	1.564	1.746
Cl	5.7153	1.020	1.015	1.010	1.005	1.000	0.995	0.990	0.986	0.981
	6.1109	1.026	1.019	1.013	1.006	1.000	0.994	0.987	0.981	0.975
	6.6195	1.020	1.015	1.010	1.005	1.000	0.995	0.990	0.986	0.981
	7.4138	1.020	1.015	1.010	1.005	1.000	0.995	0.990	0.986	0.981
	7.7902	1.019	1.015	1.010	1.005	1.000	0.995	0.990	0.986	0.981
Ti	0.3417	1.026	1.020	1.013	1.006	1.000	0.994	0.987	0.981	0.975
	1.3815	1.023	1.017	1.012	1.006	1.000	0.994	0.989	0.983	0.977
	6.4184	1.020	1.015	1.010	1.005	1.000	0.995	0.990	0.985	0.981
	6.7598	1.020	1.015	1.010	1.005	1.000	0.995	0.990	0.985	0.981
Cr	0.8351	1.025	1.019	1.013	1.006	1.000	0.994	0.988	0.982	0.976
	7.9393	1.021	1.016	1.010	1.005	1.000	0.995	0.990	0.985	0.980
	8.8841	1.021	1.015	1.010	1.005	1.000	0.995	0.990	0.985	0.980
Mn	7.0578	1.021	1.015	1.010	1.005	1.000	0.995	0.990	0.985	0.980
	7.2438	1.021	1.015	1.010	1.005	1.000	0.995	0.990	0.985	0.980
Fe	0.3522	1.025	1.019	1.013	1.006	1.000	0.994	0.988	0.982	0.976
	6.0185	1.020	1.015	1.010	1.005	1.000	0.995	0.990	0.985	0.981
	7.6311	1.020	1.015	1.010	1.005	1.000	0.995	0.990	0.985	0.981
	7.6455	1.020	1.015	1.010	1.005	1.000	0.995	0.990	0.985	0.981

* Relative to value at reference concentration no. 5

The photopeak responses are given at different concentrations of the element that has been changed sequentially. The reference elemental concentration is given in Table 4.4-3.

Given that the element i has a weight percentage w_i, the mass of the element i is changed sequentially as:

$$k\ (0.2)\ w_i\ \rho_{\text{core sample}} \quad ,k=1,2,..9$$

Where $m_{i,k}$ is the mass of the i-th element in the core sample at the k-th concentration.

NORMALIZED VARIATION OF RESPONSES WITH CONCENTRATION

Element no. 2 (Cl) has been changed sequentially

Element	Energy (MeV)	Concentration * 1	2	3	4	5	6	7	8	9
Mg	0.5852	0.708	0.783	0.857	0.929	1.000	1.069	1.137	1.204	1.269
	1.8089	0.706	0.782	0.856	0.929	1.000	1.070	1.138	1.206	1.272
	2.8281	0.708	0.783	0.857	0.929	1.000	1.069	1.138	1.204	1.270
	3.9167	0.710	0.785	0.858	0.930	1.000	1.069	1.137	1.203	1.269
Cl	5.7153	0.118	0.278	0.479	0.721	1.000	1.317	1.669	2.057	2.479
	6.1109	0.118	0.278	0.479	0.720	1.000	1.317	1.670	2.057	2.479
	6.6195	0.118	0.278	0.479	0.720	1.000	1.317	1.670	2.058	2.480
	7.4138	0.118	0.278	0.479	0.720	1.000	1.317	1.670	2.059	2.481
	7.7902	0.118	0.278	0.479	0.720	1.000	1.317	1.670	2.059	2.481
Ti	0.3417	0.660	0.748	0.834	0.918	1.000	1.080	1.159	1.236	1.311
	1.3815	0.632	0.727	0.820	0.911	1.000	1.087	1.173	1.256	1.338
	6.4184	0.626	0.723	0.817	0.909	1.000	1.089	1.176	1.261	1.344
	6.7598	0.626	0.723	0.817	0.909	1.000	1.089	1.176	1.261	1.344
Cr	0.8351	0.645	0.737	0.826	0.914	1.000	1.084	1.166	1.247	1.326
	7.9393	0.631	0.726	0.819	0.911	1.000	1.088	1.173	1.257	1.340
	8.8841	0.631	0.726	0.819	0.911	1.000	1.088	1.173	1.258	1.340
Mn	7.0578	0.609	0.710	0.809	0.905	1.000	1.092	1.183	1.272	1.358
	7.2438	0.609	0.710	0.809	0.905	1.000	1.093	1.183	1.272	1.358
Fe	0.3522	0.677	0.760	0.842	0.922	1.000	1.077	1.152	1.225	1.298
	6.0185	0.624	0.721	0.816	0.909	1.000	1.089	1.177	1.263	1.348
	7.6311	0.624	0.721	0.815	0.909	1.000	1.090	1.178	1.264	1.348
	7.6455	0.624	0.721	0.815	0.909	1.000	1.090	1.178	1.264	1.348

* Relative to value at reference concentration no. 5

See note at bottom of page 180

NORMALIZED VARIATION OF RESPONSES WITH CONCENTRATION

Element no. 3 (Ti) has been changed sequentially

Element	Energy	Concentration *								
	(MeV)	1	2	3	4	5	6	7	8	9
Mg	0.5852	0.940	0.955	0.971	0.985	1.000	1.014	1.028	1.042	1.056
	1.8089	0.932	0.950	0.967	0.983	1.000	1.016	1.032	1.048	1.064
	2.8281	0.930	0.948	0.965	0.983	1.000	1.017	1.034	1.050	1.066
	3.9167	0.929	0.947	0.965	0.983	1.000	1.017	1.034	1.051	1.067
Cl	5.7153	0.909	0.932	0.955	0.978	1.000	1.022	1.044	1.065	1.086
	6.1109	0.909	0.932	0.955	0.978	1.000	1.022	1.044	1.065	1.086
	6.6195	0.909	0.932	0.955	0.978	1.000	1.022	1.044	1.065	1.087
	7.4138	0.909	0.932	0.955	0.978	1.000	1.022	1.044	1.065	1.087
	7.7902	0.909	0.932	0.955	0.978	1.000	1.022	1.044	1.066	1.087
Ti	0.3417	0.185	0.377	0.577	0.785	1.000	1.222	1.451	1.687	1.929
	1.3815	0.184	0.377	0.577	0.785	1.000	1.223	1.453	1.690	1.934
	6.4184	0.184	0.377	0.577	0.785	1.000	1.223	1.453	1.690	1.935
	6.7598	0.184	0.377	0.577	0.785	1.000	1.223	1.453	1.690	1.935
Cr	0.8351	0.922	0.942	0.962	0.981	1.000	1.019	1.037	1.055	1.072
	7.9393	0.921	0.941	0.961	0.981	1.000	1.019	1.038	1.057	1.075
	8.8841	0.921	0.941	0.961	0.981	1.000	1.019	1.038	1.057	1.075
Mn	7.0578	0.909	0.932	0.955	0.978	1.000	1.022	1.044	1.065	1.086
	7.2438	0.909	0.932	0.955	0.978	1.000	1.022	1.044	1.065	1.086
Fe	0.3522	0.929	0.947	0.965	0.983	1.000	1.017	1.033	1.049	1.065
	6.0185	0.924	0.943	0.963	0.981	1.000	1.018	1.037	1.054	1.072
	7.6311	0.924	0.943	0.962	0.981	1.000	1.018	1.037	1.054	1.072
	7.6455	0.924	0.943	0.962	0.981	1.000	1.018	1.037	1.055	1.072

* Relative to value at reference concentration no. 5

See note at bottom of page 180

NORMALIZED VARIATION OF RESPONSES WITH CONCENTRATION

Element no. 4 (Cr) has been changed sequentially

Element	Energy	Concentration *								
	(MeV)	1	2	3	4	5	6	7	8	9
Mg	0.5852	1.001	1.001	1.001	1.000	1.000	1.000	0.999	0.999	0.999
	1.8089	0.997	0.998	0.998	0.999	1.000	1.001	1.002	1.002	1.003
	2.8281	0.995	0.997	0.998	0.999	1.000	1.001	1.002	1.003	1.004
	3.9167	0.995	0.996	0.997	0.999	1.000	1.001	1.003	1.004	1.005
Cl	5.7153	1.003	1.002	1.001	1.001	1.000	0.999	0.999	0.998	0.997
	6.1109	1.003	1.002	1.001	1.001	1.000	0.999	0.999	0.998	0.997
	6.6195	1.003	1.002	1.001	1.001	1.000	0.999	0.999	0.998	0.997
	7.4138	1.003	1.002	1.001	1.001	1.000	0.999	0.999	0.998	0.997
	7.7902	1.003	1.002	1.001	1.001	1.000	0.999	0.999	0.998	0.997
Ti	0.3417	1.005	1.004	1.003	1.001	1.000	0.999	0.997	0.996	0.995
	1.3815	1.002	1.001	1.001	1.000	1.000	1.000	0.999	0.999	0.998
	6.4184	0.999	0.999	0.999	1.000	1.000	1.000	1.001	1.001	1.001
	6.7598	0.999	0.999	0.999	1.000	1.000	1.000	1.001	1.001	1.001
Cr	0.8351	0.201	0.401	0.601	0.801	1.000	1.199	1.397	1.595	1.792
	7.9393	0.200	0.400	0.600	0.800	1.000	1.200	1.399	1.599	1.798
	8.8841	0.200	0.400	0.600	0.800	1.000	1.200	1.399	1.599	1.798
Mn	7.0578	1.002	1.001	1.001	1.000	1.000	1.000	0.999	0.999	0.998
	7.2438	1.002	1.001	1.001	1.000	1.000	1.000	0.999	0.999	0.998
Fe	0.3522	1.006	1.004	1.003	1.001	1.000	0.999	0.997	0.996	0.994
	6.0185	1.002	1.001	1.001	1.000	1.000	1.000	0.999	0.999	0.998
	7.6311	1.002	1.001	1.001	1.000	1.000	1.000	0.999	0.999	0.998
	7.6455	1.002	1.001	1.001	1.000	1.000	1.000	0.999	0.999	0.998

* Relative to value at reference concentration no. 5

See note at bottom of page 180

NORMALIZED VARIATION OF RESPONSES WITH CONCENTRATION

Element no. 5 (Mn) has been changed sequentially

Element	Energy	Concentration *								
	(MeV)	1	2	3	4	5	6	7	8	9
Mg	0.5852	1.000	1.000	1.000	1.000	1.000	1.000	1.000	1.000	1.000
	1.8089	0.998	0.998	0.999	0.999	1.000	1.001	1.001	1.002	1.002
	2.8281	0.997	0.998	0.999	0.999	1.000	1.001	1.001	1.002	1.003
	3.9167	0.997	0.998	0.998	0.999	1.000	1.001	1.002	1.002	1.003
Cl	5.7153	1.000	1.000	1.000	1.000	1.000	1.000	1.000	1.000	1.000
	6.1109	1.000	1.000	1.000	1.000	1.000	1.000	1.000	1.000	1.000
	6.6195	1.000	1.000	1.000	1.000	1.000	1.000	1.000	1.000	1.000
	7.4138	1.000	1.000	1.000	1.000	1.000	1.000	1.000	1.000	1.000
	7.7902	1.000	1.000	1.000	1.000	1.000	1.000	1.000	1.000	1.000
Ti	0.3417	1.001	1.001	1.001	1.000	1.000	1.000	0.999	0.999	0.999
	1.3815	1.000	1.000	1.000	1.000	1.000	1.000	1.000	1.000	1.000
	6.4184	0.998	0.999	0.999	1.000	1.000	1.000	1.001	1.001	1.002
	6.7598	0.998	0.999	0.999	1.000	1.000	1.000	1.001	1.001	1.002
Cr	0.8351	1.000	1.000	1.000	1.000	1.000	1.000	1.000	1.000	1.000
	7.9393	0.998	0.999	0.999	1.000	1.000	1.000	1.001	1.001	1.002
	8.8841	0.998	0.999	0.999	1.000	1.000	1.000	1.001	1.001	1.002
Mn	7.0578	0.200	0.400	0.600	0.800	1.000	1.200	1.401	1.601	1.802
	7.2438	0.200	0.400	0.600	0.800	1.000	1.200	1.401	1.601	1.802
Fe	0.3522	1.001	1.001	1.000	1.000	1.000	1.000	1.000	0.999	0.999
	6.0185	0.996	0.997	0.998	0.999	1.000	1.001	1.002	1.003	1.003
	7.6311	0.996	0.997	0.998	0.999	1.000	1.001	1.002	1.003	1.004
	7.6455	0.996	0.997	0.998	0.999	1.000	1.001	1.002	1.003	1.004

* Relative to value at reference concentration no. 5

See note at bottom of page 180

NORMALIZED VARIATION OF RESPONSES WITH CONCENTRATION

Element no. 6 (Fe) has been changed sequentially

Element	Energy	Concentration *								
	(MeV)	1	2	3	4	5	6	7	8	9
Mg	0.5852	0.993	0.996	0.999	1.000	1.000	0.999	0.997	0.995	0.991
	1.8089	0.957	0.969	0.981	0.991	1.000	1.008	1.015	1.021	1.026
	2.8281	0.946	0.961	0.975	0.988	1.000	1.011	1.020	1.029	1.037
	3.9167	0.939	0.956	0.972	0.987	1.000	1.012	1.024	1.034	1.043
Cl	5.7153	1.055	1.041	1.027	1.013	1.000	0.987	0.974	0.962	0.949
	6.1109	1.054	1.040	1.027	1.013	1.000	0.987	0.974	0.962	0.950
	6.6195	1.055	1.041	1.027	1.013	1.000	0.987	0.974	0.962	0.949
	7.4138	1.055	1.041	1.027	1.013	1.000	0.987	0.974	0.962	0.949
	7.7902	1.055	1.041	1.027	1.013	1.000	0.987	0.974	0.962	0.949
Ti	0.3417	1.066	1.049	1.032	1.016	1.000	0.984	0.969	0.953	0.938
	1.3815	1.043	1.032	1.022	1.011	1.000	0.989	0.979	0.968	0.957
	6.4184	1.024	1.018	1.012	1.006	1.000	0.994	0.988	0.981	0.975
	6.7598	1.024	1.018	1.012	1.006	1.000	0.994	0.988	0.981	0.975
Cr	0.8351	1.046	1.034	1.023	1.011	1.000	0.989	0.977	0.966	0.955
	7.9393	1.014	1.010	1.007	1.004	1.000	0.996	0.993	0.989	0.985
	8.8841	1.014	1.010	1.007	1.004	1.000	0.996	0.993	0.989	0.985
Mn	7.0578	1.033	1.025	1.016	1.008	1.000	0.992	0.984	0.976	0.968
	7.2438	1.033	1.025	1.016	1.008	1.000	0.992	0.984	0.976	0.968
Fe	0.3522	0.212	0.418	0.618	0.812	1.000	1.182	1.359	1.531	1.697
	6.0185	0.204	0.407	0.607	0.805	1.000	1.193	1.384	1.572	1.757
	7.6311	0.204	0.407	0.607	0.805	1.000	1.193	1.384	1.572	1.758
	7.6455	0.204	0.407	0.607	0.805	1.000	1.193	1.384	1.572	1.758

* Relative to value at reference concentration no. 5

See note at bottom of page 180

APPENDIX I

Sample Input File for MCNP

```
1 MCNP   VERSION  3B3  LD=                              19-NOV-89  00:44:
 ******************************************************************************          PROBID =   19-NOV-89  00:44:

  1-      NCPGR SEAFLOOR CORE ANALYZER (ABDULLAH ALMASOUMI)
  2-      C
  3-      C    Cell definition cards
  4-      C
  5-          1    7    -1.0    -1 19 -29 2 40      $WATER
  6-          2    7    -1.0    -40 19 -35 13       $WATER
  7-          3    7    -1.0    -40 35 -39 13       $WATER
  8-          4    7    -1.0    -1 29 -39 40        $WATER
  9-          5    7    -1.0    -1 39 -30 41        $WATER
 10-          6    7    -1.0    -41 39 -30 13       $WATER
 11-          7    7    -1.0    -1 30 -34 41 10     $WATER
 12-          8    7    -1.0    -41 30 -33 10 13    $WATER
 13-          9    7    -1.0    -41 33 -34 10 13    $WATER
 14-         10    5    -.969   -2 19 -28 3         $TUBE MATERIAL (POLY)
 15-         11    5    -.969   -2 28 -29           $TUBE MATERIAL (POLY)
 16-         12    3    -.969   -3 19 -20 8         $POLYETHYLENE
 17-         13   11    -8.96   -8 19 -22           $COPPER
 18-         14   10    -2.699  -4 20 -21 8         $ALUMINUM
 19-         15    3    -.969   -3 20 -22 4         $POLYETHYLENE
 20-         16   10    -2.699  -4 21 -22 6         $ALUMINUM
 21-         17    0          -6 21 -23 8          $AIR
 22-         18   10    -2.699  -8 22 -23           $ALUMINUM
 23-         19    3    -.969   -3 22 -26 5         $POLYETHYLENE
 24-         20   10    -2.699  -5 22 -25 6         $ALUMINUM
 25-         21    0          -6 23 -24 7          $AIR
 26-         22    0          -6 24 -25            $AIR
 27-         23   12    -5.36   -7 23 -24           $DETECTOR (APPROXIMATED WITH GALLIUM)
 28-         24   10    -2.699  -5 25 -26           $ALUMINUM
 29-         25    3    -.969   -3 26 9             $POLYETHYLENE
 30-         26    6    -11.35  -9 26 -27           $LEAD CONE
 31-         27    4    -8.65   -3 27 -28           $CADMIUM
 32-         28    5    -.969   -10 30 -31          $TUBE MATERIAL (POLY)
 33-         29    5    -.969   -10 31 -34 11       $TUBE MATERIAL (POLY)
 34-         30    6    -11.35  -11 31 -32          $LEAD
 35-         31    6    -11.35  -11 32 -33 12       $LEAD
 36-         32    9    -7.84   -12 32 -33          $S.S. 316
 37-         33    3    -.969   -11 33 -34          $POLYETHYLENE
 38-         34    5    -.969   -13 19 -34 14       $TUBE MATERIAL (POLY)
 39-         35    3    -.969   -14 19 -35 15       $POLYETHYLENE
 40-         36    4    -8.65   -15 19 -35 16       $CADMIUM
 41-         37    3    -.969   -16 19 -35 17       $POLYETHYLENE
 42-         38    3    -.969   -14 35 -36 17       $POLYETHYLENE
 43-         39    0          -14 36 -37 17        $AIR
 44-         40    3    -.969   -14 37 -38 17       $POLYETHYLENE
 45-         41    3    -.969   -14 38 -34 15       $POLYETHYLENE
 46-         42    4    -8.65   -15 38 -34 16       $CADMIUM
 47-         43    3    -.969   -16 38 -34 17       $POLYETHYLENE
 48-         44    8    -.969   -17 19 -34 18       $SAMPLE CASING (POLY)
 49-         45    1    -2.45236587 -18 19 -35          $CORE SAMPLE
 50-         46    1    -2.45236587 -18 35 -38          $CORE SAMPLE
 51-         47    1    -2.45236587 -18 38 -34          $CORE SAMPLE
 52-         48    0          (1:-19:34) -51       $INNER ENVELOPE
 53-         49    0          51                   $UNIVERSE
 54-
 55-     C
 56-     C    Surface definition cards
 57-     C
 58-     C
 59-     C    Surfaces 1-39 are to describe the physical geometry,
 60-     C             40-50 are used for tally, importance, and definition
 61-     C             purposes only. An additional outer surface 51 may be
 62-     C             added for geometry check
 63-     C
 64-         1    CZ    50.0
 65-         2   C/Z    0.0 -3.0 7.25
 66-         3   C/Z    0.0 -3.0 6.25
 67-         4   C/Z    0.0 -3.0 4.75
 68-         5   C/Z    0.0 -3.0 3.75
 69-         6   C/Z    0.0 -3.0 3.55
 70-         7   C/Z    0.0 -3.0 2.5
```

```
71-          8   C/Z    0.0 -3.0 0.9
72-          9   K/Z    0.0 -3.0 60.2 0.25 1
73-         10   C/Z    0.0 -3.0 6.0
74-         11   C/Z    0.0 -3.0 5.0
75-         12   C/Z    0.0 -3.0 0.5
76-         13   C/Z    0.0 22.55 6.55
77-         14   C/Z    0.0 22.55 5.55
78-         15   C/Z    0.0 22.55 5.05
79-         16   C/Z    0.0 22.55 4.75
80-         17   C/Z    0.0 22.55 4.25
81-         18   C/Z    0.0 22.55 3.75
82-         19    PZ    0.0
83-         20    PZ    48.2
84-         21    PZ    50.2
85-         22    PZ    54.2
86-         23    PZ    62.3
87-         24    PZ    67.3
88-         25    PZ    67.5
89-         26    PZ    67.7
90-         27    PZ    72.7
91-         28    PZ    73.0
92-         29    PZ    74.0
93-         30    PZ    79.0
94-         31    PZ    80.0
95-         32    PZ    85.0
96-         33    PZ    90.0
97-         34    PZ    100.0
98-         35    PZ    59.0
99-         36    PZ    59.5
100-        37    PZ    89.5
101-        38    PZ    90.0
102-        39    PZ    77.0
103-        40   C/Z    0.0 27.55 10.55
104-        41   C/Z    0.0 22.55 27.00
105-        42    PZ    56.0
106-        43    PZ    62.0
107-        44    PZ    67.0
108-        45    PZ    72.0
109-        46    PZ    77.0
110-        47    PZ    82.0
111-        48    PZ    87.0
112-        49    PZ    93.0
113-        50    PY    -3.0
114-        51    SZ    50.0 80.0
115-
116-    C
117-    C   Source particles are neutrons but gamma rays will be generated
118-    C   at neutron collisions
119-    C
120-    MODE N P
121-    C
122-    C   Isotropic point neutron source of Cf-252 with D1 energy
123-    C   distribution
124-    C   The SDEF with SUR=51 card is used for geometry debugging
125-    C
126-    C   SDEF  SUR=50 NRM=-1
127-    C
128-    SDEF  POS=0.0 -3.0 86.0  ERG=D1 DIR=D2 VEC=0 .8364234 -.5480837
129-    SI1  Maxwell fission spectrum with temperature of 1.424 MeV
130-    SP1   -2 1.424
131-    SI2  Continuous exponential directional bias
132-    SB2   -31 3.5
133-    C   Initial direction of flight. Mu is sampled w.r.t. VEC
134-    C
135-    C   Specification of cell importance w.r.t. neutron transport. Cells
136-    C   that are likely to transport neutrons towards the sample are
137-    C   considered more important
138-    C
139-    IMP:N 1 1 3 2 1 3 1 3 1 1 3 1 8R 2 1 1 2 1 1 1 2 1 2 1 1 1 2 1 3R 3 3
140-          2 1 2 3 3 3 3 0 0
141-    C
142-    C   Force collisions to take place when the neutron is in the sample
143-    C
144-    FCL:N 44J 0.5 1.0 0.5 0 0
```

```
C
C   Specification of cell importance w.r.t. gamma ray trnsmisssion.
C   Cells that are likely to be traversed by photons towards the
C   detector are considred important. Otherwise, photons scattered
C   off other cells are "killed" (0 importance)
C
IMP:P 1 46R 0 0
C
C   Materials and cross section tables specification
C
M1   12000.51C -.0216014 17000.51C -.0036326 22000.51C -.0339442
     24000.50C -.0074101 25055.51C -.0024754 26000.55C -.0925769
     1001.50C  -.0109823 6012.50C  -.0067811 8016.50C  -.5362210
     11023.51C -.0096411 13027.50C -.0061714 14000.51C -.2593048
     20000.51C -.0092576                              $CORE SAMPLE
M3   1001.50C  -.1437176 6012.50C  -.8562824          $POLYETHYLENE
M4   48000.51C 1.0                                    $CADMIUM
M5   1001.50C  -.1437176 6012.50C  -.8562824          $POLYETHYLENE
M6   82000.50C 1.0                                    $LEAD
M7   1001.50C  -.1119013 8016.50C  -.8880937          $WATER
M8   1001.50C  -.1437176 6012.50C  -.8562824          $POLYETHYLENE
M9   24000.50C -.18048  25055.51C -.01956  26000.55C -.62924
     28000.50C -.13998  42000.51C -.03074             $S.S 316
M10  13027.50C 1.0                                    $ALUMINUM
M11  29000.50C 1.0                                    $COPPER
M12  31000 1.0                                        $GALLIUM
C
C   S(a,b) treatment is specified for water and polyethylene
C   AT 300 K
C
MT3  POLY.01T
MT5  POLY.01T
MT7  LWTR.01T
MT8  POLY.01T
C
C   ONLY SELECTED LINE GAMMAS ARE ALLOWED, ALL OTHER GAMMAS AS A
C   RESULT OF COLLISIONS ARE TURNED OFF
C   Na:  0.472,.87,2.027, AND 2.517 MeV
C   Cl:  5.715,6.11,6.619, AND 7.413 MeV
C   THE FREQUENCY OF SAMPLING IS EQUAL FOR ALL LINE GAMMA RAYS;
C   HAS TO RE-ADJUST ACCRORDING TO THE BRANCHING RATIO
C
PIKMT 11023.51 4 102060 1.0 102054 1.0 102042 1.0 102037 1.0
      17000.51 4 102010 1.0 102007 1.0 102005 1.0 102003 1.0
C
C   Tally specifications
C   all tallies are per source neutron
C
FC4  Neutron flux averaged over sections of the core sample
F4:N 45
E4   2.0E-6 10.0
FS4  -42
FQ4  F S E
F14:N 46
E14   2.0E-6 10.0
FS14 -43 -44 -45 -46 -47 -48
FQ14 F S E
F24:N 47
E24  2.0E-6 10.0
FS24 -49
FQ24 F S E
FC34 Neutron flux averaged over the detector volume, cell 23
F34:N 23
SF34 24
E34  2.0E-6 10.0
FQ34 F D E
FC44 Neutron flux averaged over the detector tube Cd volume
F44:N 27
E44  2.0E-6 10.0
FQ44 F D E
C
```

```
C     A DXTRAN SPHERE IS SPECIFIED TO SURROUND THE DETECTOR
C
DXT:P  0. -3. 64.8 3.54 3.8
FC1   Photon current integrated over detector top surface (-DIRECTION)
F1:P  24
E1     .1 .2 .3 .4 .5 .6 .7 .8 .9 1. 1.1 1.2 1.3 1.4 1.5 1.6 1.7 1.8
       1.9 2. 2.1 2.2 2.3 2.4 2.5 2.6 2.7 2.8 2.9 3. 3.1 3.2 3.3 3.4
       3.5 3.6 3.7 3.8 3.9 4. 4.1 4.2 4.3 4.4 4.5 4.6 4.7 4.8 4.9 5.
       5.1 5.2 5.3 5.4 5.5 5.6 5.7 5.8 5.9 6.0 6.1 6.2 6.3 6.4 6.5
       6.6 6.7 6.8 6.9 7. 7.1 7.2 7.3 7.4 7.5 7.6
C1     0 1
FS1   -7
FQ1   F S C E
FC11  Photon current integrated over detector side wall
F11:P 7
E11    .1 .2 .3 .4 .5 .6 .7 .8 .9 1. 1.1 1.2 1.3 1.4 1.5 1.6 1.7 1.8
       1.9 2. 2.1 2.2 2.3 2.4 2.5 2.6 2.7 2.8 2.9 3. 3.1 3.2 3.3 3.4
       3.5 3.6 3.7 3.8 3.9 4. 4.1 4.2 4.3 4.4 4.5 4.6 4.7 4.8 4.9 5.
       5.1 5.2 5.3 5.4 5.5 5.6 5.7 5.8 5.9 6.0 6.1 6.2 6.3 6.4 6.5
       6.6 6.7 6.8 6.9 7. 7.1 7.2 7.3 7.4 7.5 7.6
FS11  -50 -23 -24
FQ11  F S E
FC21  Photon current integrated over detector bottom (+DIRECTION)
F21:P 23
E21    .1 .2 .3 .4 .5 .6 .7 .8 .9 1. 1.1 1.2 1.3 1.4 1.5 1.6 1.7 1.8
       1.9 2. 2.1 2.2 2.3 2.4 2.5 2.6 2.7 2.8 2.9 3. 3.1 3.2 3.3 3.4
       3.5 3.6 3.7 3.8 3.9 4. 4.1 4.2 4.3 4.4 4.5 4.6 4.7 4.8 4.9 5.
       5.1 5.2 5.3 5.4 5.5 5.6 5.7 5.8 5.9 6.0 6.1 6.2 6.3 6.4 6.5
       6.6 6.7 6.8 6.9 7. 7.1 7.2 7.3 7.4 7.5 7.6
C21    0 1
FS21  -7
FQ21  F S C E
C
C     The VOID card is for geometry check
C
C     VOID
C
C     Conditional termination
C
CUT:P J 0.1
NPS   1000              $excusion is terminated when histories are exhausted
PRINT                    $print full output
```